Dielectric Metasurfaces with Overlapped Modes: An Ultrathin Platform for Infrared Optics

By

Austin Howes

Dissertation
Submitted to the Faculty of the
Graduate School of Vanderbilt University
in partial fulfillment of the requirements
for the degree of

DOCTOR OF PHILOSOPHY
in
Physics

May 8, 2020
Nashville, Tennessee

Approved:

Jason Valentine, Ph.D.

Richard Haglund, Ph.D.

Sharon Weiss, Ph.D.

Yaqiong Xu, Ph.D.

Sokrates Pantelides, Ph.D.

ACKNOWLEDGEMENTS

My journey towards a Ph.D. degree has been made possible by the support of many people. First, I would like to thank my advisor, Jason Valentine, for his guidance, compassion, and patience throughout the years. He taught me that in order to do quality science, you must not only answer the question of “How can we achieve this?”, but “Why should we achieve this?” as well. This mentality has shaped my time as a graduate student, and I will carry that attitude with my scientific endeavors in the future. I appreciate his openness to my questions and concerns, whether talking about research projects on campus or preparing for job interviews at his home. I am very thankful that spending time with him over the past few years has taught me to think more critically, creatively, and helped me persevere during difficult times. There is no one else I would have rather carve out new knowledge with, and my time as his student has made me not only a better scientist, but also a better person.

Additionally, I would like to thank all of my lab mates from the past and present in the Valentine group. This set of people provided much-needed camaraderie during the ups and downs of completing my Ph.D. In particular, I want to give my thanks to Wenyi Wang for taking me under her wing when I was new to the group, and both Zack Coppens and Zhihua Zhu for their mentorship and friendship in and out of the clean room. Finally, thank you to You, Fabian, Scott, Elena, Hanyu, and everyone else in the lab for the helpful discussions, encouragement, and countless hours working hard together to succeed. I wish you all well in your own paths to completing your Ph.Ds.

I would also like to thank the staff at the Vanderbilt Institute of Nanoscale Science and Engineering (VINSE) for their immense help training and assisting me in the clean room and imaging suite. Special thanks to Kurt Heinrich for his support with the etching equipment, Tony Hmelo for his help with the SEM, and Bill and Alice for their guidance with the evaporators and furnaces. They all have made learning the details of nanofabrication much easier, and I am grateful for their work ethic in keeping the space clean and running perfectly. None of my devices would be possible without their knowledge.

I should also thank Josh Caldwell for his guidance, expertise, and equipment over the past few years. Even though he arrived during my final years as a graduate student, he still had plenty of time to make a tremendous impact on my progress and achievements. I am grateful for all the insight he has given to help me both in my research and in my career pursuits. I'm confident his lab's successes will continue to grow, and I wish everyone the best.

I also want to express my gratitude to my committee members Sokrates Pantiledes, Sharon Weiss, Yaqiong Xu, and Richard Haglund for their time, support, and suggestions regarding my work. Every scientist can benefit from a variety of perspectives, and I appreciate all of their input in shaping my projects over the years.

I would not be where I am today without my family, and they are indirectly responsible for everything I have been able to accomplish. This dissertation, and all of the work therein, is possible due to their support and love. Thank you for everything you've sacrificed to help get me to this point; I'll continue to do my best to make you proud.

Finally, I need to thank my best friend and wife, Victoria, for her unyielding support and love. These last six years have been infinitely more enjoyable and manageable with her by my side. Thank you for all you've helped me achieve and all the times we've pushed through stressful days together. I can finally say all those weekends working at coffee shops have paid off, and I'm looking forward to navigating the future with you.

TABLE OF CONTENTS

Page

LIST OF TABLES

Table **Page**

LIST OF FIGURES

LIST OF ABBREVIATIONS

3C-SiC	3C Silicon Carbide
AFM	Atomic Force Microscopy
AR	Aspect Ratio
ENZ	Epsilon-Near-Zero
FTIR	Fourier Transform Infrared (Spectrometer)
HF	Hydrofluoric Acid
ITO	Indium Tin Oxide
IPA	Isopropyl Alcohol
IST	Intersubband Transition
LPCVD	Low Pressure Chemical Vapor Deposition
MCT	Mercury Cadmium Telluride
MIBK	Methyl Isobutyl Ketone
MQW	Multi-Quantum Well
NA	Numerical Aperture
(N)IR	(Near) Infrared
PMMA	Poly(Methyl Methacrylate)
QCL	Quantum Cascade Laser
QCSE	Quantum Confined Stark Effect
QF	Quality Factor
SEM	Scanning Electron Microscope
SPhP	Surface Phonon Polariton

SPR	Surface Plasmon Resonance
TCO	Transparent Conducting Oxide
TO	Transverse Optic
VINSE	Vanderbilt Institute of Nanoscale Science and Engineering

LIST OF PUBLICATIONS

Portions of this dissertation have been drawn from the following publications and manuscripts:

A. Howes, J.R. Nolen, J. D. Caldwell, and J. Valentine, "Near-Unity and Narrowband Thermal Emissivity in Balanced Dielectric Metasurfaces", **Advanced Optical Materials**, 1901470 (2019).

A. Howes, W. Wang, I. Kravchenko, and J. Valentine, "Dynamic Transmission Control Based on All-Dielectric Huygens Metasurfaces", **Optica**, Vol. 5, Issue 7, pp.787-792 (2018).

A. Howes and Z. Zhu, D. Curie, V. Wheeler, R. Haglund, and J. Valentine, "High-Efficiency Optical Limiter Based on Phase-Change Material-Integrated Huygens Metasurfaces", Manuscript in review.

A. Howes, R. Sarma, I. Brener, and J. Valentine, "Multi-Quantum Well-Based Phase Modulating Metasurfaces", Manuscript in preparation.

CHAPTER 1

Introduction

1.1. History of Metamaterial Optics

1.1.1. Importance of Permittivity and the Concept of Effective Medium

Throughout the history of science, light and electromagnetism have played an essential role in shaping humans' understanding of the natural world and technology to improve our existence within it. The origin of such progress stems from our theoretical understanding of how light interacts with matter, allowing for the design of materials that can distort and harness such interactions for a desired application. Combined with the Lorentz force law, the fundamental physics governing this behavior is described by Maxwell's equations, shown below in differential form and SI units.

$$\nabla \cdot \vec{\mathbf{D}} = \rho \qquad \nabla \cdot \vec{\mathbf{B}} = 0$$

$$\nabla \times \vec{\mathbf{E}} = -\frac{\partial \vec{\mathbf{B}}}{\partial t} \qquad \nabla \times \vec{\mathbf{H}} = \vec{\mathbf{j}} + \frac{\partial \vec{\mathbf{D}}}{\partial t} \tag{1}$$

E denotes the electric field, **H** is the magnetic field, **D** is the displacement current, **B** is the magnetic flux, ρ is the charge density, and **j** is the current density. This set of equations provides a model for the relationship between fields, charges, and currents formed in materials and forms the basis of electromagnetism and optics. Using Maxwell's equations and the associated constitutive relations $\vec{\boldsymbol{D}} = \varepsilon_0 \varepsilon_r \vec{\boldsymbol{E}}$, $\vec{\boldsymbol{B}} = \mu_0 \mu_r \vec{\boldsymbol{H}}$, the famous wave equation can be derived (assuming no free charges), shown below for the electric field.

$$\nabla^2\vec{\mathbf{E}} = \mu_0\mu_r\varepsilon_0\varepsilon_r\frac{\partial^2\mathbf{E}}{\partial t^2} \tag{2}$$

Here, ε_r and μ_r are the relative electric permittivity and magnetic permeability. They measure the strength of interaction between the electric and magnetic field with the medium, respectively. Additionally, the constants ε_0 = 8.85e-12 F/m and μ_0 = 1.26e-6 H/m are the vacuum permittivity and permeability. Equation 2 illustrates that the propagation of the field through a material is a wave dictated by the relative permittivity and permeability.

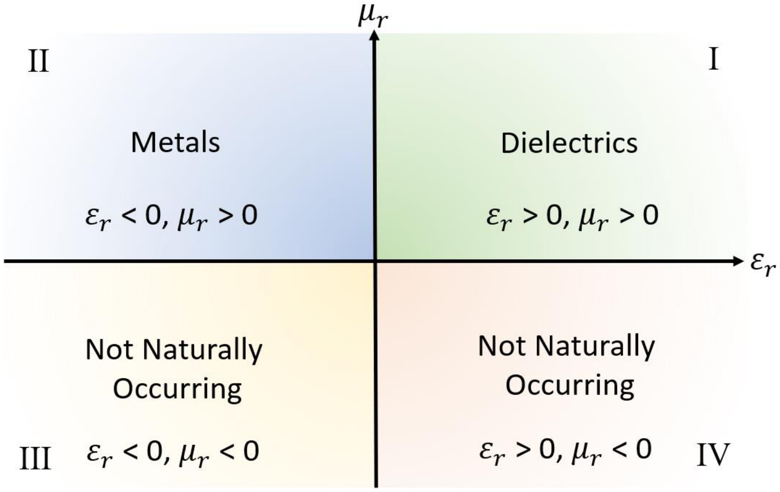

Figure 1.1: Parameter map for the electric permittivity and magnetic permeability.

When light interacts with matter, there are three main processes that occur: reflection, transmission, and absorption. How much energy is directed into each of these three processes is determined by the material’s permittivity and permeability at the wavelength of the incident light. Figure 1.1 illustrates the parameter space of ε_r and μ_r, which can be split into four regions. Naturally occurring materials fall into regions I and II where the permeability is positive; a positive permittivity is a characteristic of a dielectric while a negative permittivity represents a metallic response. However, regions III and IV are much less populated and generally cannot be achieved with naturally occurring materials.

In a natural material, the position, size, arrangement, etc. of the constituent atoms govern the permittivity, permeability, and therefore the overall electromagnetic response. However, the parameter space can be expanded by instead creating materials with nanostructured resonant elements that are smaller than the wavelength of light. In doing so, these nanostructures provide an artificial response that is seen as an effective medium with optical properties determined by the structure and composition of the resonators. This is known as a metamaterial, and the resonators that support their unique electromagnetic response are commonly referred to as “meta-atoms”.

The role of meta-atoms in engineering the permittivity and permeability is described by Maxwell Garnett in cases where metallic elements represent a small filling fraction of the metamaterial (Markel, 2016) and effective medium theory for larger filling fractions. Note that these approaches only consider the proportion of materials and do not account for resonances generated by the structure of any subwavelength elements. Careful design of meta-atoms allows metamaterials to fill the gaps in the parameter space uninhabited by naturally occurring materials. With more complete control over the permittivity and permeability, it is possible to design new optics and electromagnetic devices that can direct energy is ways that are normally impossible in traditional media.

1.1.2. First Demonstrations and Applications

The first discussion of engineering materials with previously unseen ε_r and $\mu_{r,}$ and its consequences on the optical characteristics was by Veselago (Veselago, 1968). However, the first metamaterial to demonstrate simultaneously negative permittivity and permeability was realized in 2000 (Smith, Padilla, Vier, Nemat-Nasser, & Schultz, 2000). This was accomplished in the microwave spectral range by using metallic wires to force the permittivity below zero and split-ring resonators that generate an artificial magnetic dipole current to engineer the permeability. This structure, known as a “negative index metamaterial”, allows for unique optical phenomena such as negative refraction at interfaces. As the metamaterial field has grown in the past twenty years, the wavelength range in which metamaterials are possible to create has expanded alongside improvements in nanoscale fabrication techniques. While meta-atoms only need to be on the scale of millimeters in the microwave range, such structures need to be micrometers or hundreds of nanometers in size for metamaterials in the infrared or visible range, respectively.

Regardless of wavelength, the flexibility in permittivity and permeability allowed by metamaterials has been proven extremely useful for miniaturizing optics. For example, flat lenses have been demonstrated using metasurfaces (2D analogues of metamaterials) by harnessing the reflected phase of individual meta-atoms. Since each meta-atom has a resonant frequency that is dependent on its size, it is possible to focus light into a focal spot by creating a phase gradient across the metasurface (Aieta et al., 2012). Similarly, it is possible to design anisotropic metasurfaces that function as waveplates (Yu et al., 2012) and holograms by encoding an image into a metasurface using its phase information (J. Lin, Genevet, Kats, Antoniou, & Capasso, 2013). Metasurfaces have also been used for optical cloaking (Ni, Wong, Mrejen, Wang, & Zhang, 2015), antennas (Faenzi et al., 2019; Y. Yang et al., 2014), filters (Asadchy et al., 2015; C.-S. Park et al., 2019), and other applications in which naturally occurring materials with the required properties are either scarce, prohibitively expensive, or otherwise unavailable. This customizability makes metamaterials and metasurfaces a powerful tool not only for realizing ultrathin versions of existing devices, but also for creating new devices with unique properties.

1.2. Material Choices in Meta-Optics

1.2.1. Plasmonics, Benefits and Limitations

Historically, metallic structures are the most common resonant elements in metamaterials. At high frequencies, such structures possess localized surface plasmon resonances (LSPRs). A surface plasmon is a mode associated with the oscillation of free electrons at a metal's surface induced by the electric field from incident light. In a metallic film, additional structuring such as coupling prisms or gratings are necessary to provide the in-plane momentum needed to make a surface plasmon available for excitation via free-space (Fox, 2012). However, metallic meta-atoms are designed to scatter light at the boundaries, providing the necessary momentum vector to excite SPRs. The resonant frequency of the plasmonic structure will depend on its morphology and dimensions; generally, the larger the nanostructure, the lower the energy of the SPR. When excited, surface plasmon polaritons (SPPs) propagate along the polarization axis and the resonant wavelength of the SPP is related to the size of the resonator by $L = m\lambda/2$, where L is the length of the nanostructure in the direction of the polarization, λ is the wavelength of the SPP, and m is an integer (the fundamental mode exists at m=1).

Plasmonic sub-wavelength resonators are commonly used in metamaterials due to their excellent field enhancement properties near the surface of the metal. This can be useful for integrating the resonant fields of the nanostructure with other components such as electro-optic materials (Tunable meta-optics will be discussed in Section 1.3). Strong field concentration is possible using dielectric feed-gaps between plasmonic resonators (L. Huang et al., 2013). Since the normal component of the electric field must be conserved across the boundary between the metal and dielectric, the field is enhanced in the dielectric by $|\varepsilon_m/\varepsilon_d|$, where ε_m and ε_d are the associated permittivities. Additionally, electric field hotspots via bowtie structures have been employed by squeezing free electrons to a point , generating field enhancements on the order of 10^3 (Schuck, Fromm, Sundaramurthy, Kino, & Moerner, 2005). However, plasmonic architectures often suffer from unwanted absorption losses, and the large imaginary permittivity of metals results in low quality factors of their resonant modes (Fleming, Lin, El-Kady, Biswas, & Ho, 2002; S. Y. Lin, Moreno, & Fleming, 2003; Mason, Smith, & Wasserman, 2011; Sai & Yugami, 2004), which often limits their use in sensing and applications that require high spectral resolution. It also often requires plasmonic metamaterials to operate in reflection mode, which can be more inconvenient than transmission mode for integration into technology.

1.2.2. Dielectrics, Benefits and Limitations

In recent years, dielectrics have been investigated as substitutes for metallic resonators in metamaterials. The main benefit for designing resonators comprised of dielectrics such as silicon or germanium is their low loss and relatively low dispersion. This enables more efficient meta-optics compared to their plasmonic counterparts, where parasitic losses limit throughput and quality of resonant modes. Many different optics have been realized using dielectric metasurfaces

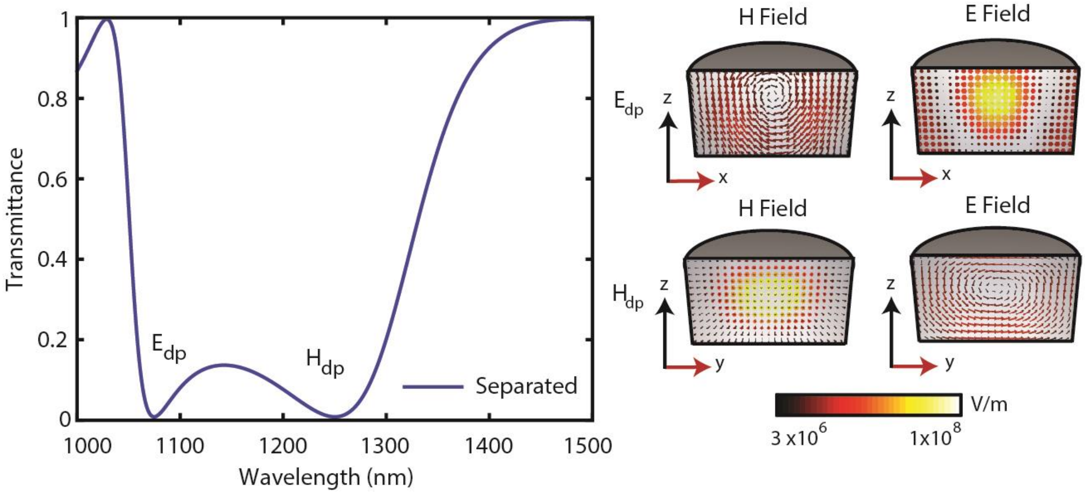

Figure 1.2: Description of fundamental Mie dipole resonances. Left: Transmittance as a function of wavelength for an array of silicon nanopillars with diameter = 500nm, height = 230nm, and period = 800nm. Right: Field profiles at the wavelength of the electric and magnetic dipole Mie resonances.

such as high-efficiency lenses that correct for chromatic dispersion to increase the operation bandwidth (A. Arbabi, Horie, Ball, Bagheri, & Faraon, 2015; E. Arbabi, Arbabi, Kamali, Horie, & Faraon, 2016), polarization-sensitive filters (B. Yang et al., 2018), waveplates (Pfeiffer & Grbic, 2013a), and frequency-selective beam steering (B. H. Chen et al., 2017).

Much of the contrast between plasmonic and dielectric metamaterials lies within their resonant field profiles. In place of SPRs, high-index dielectric nanostructures have modes known as Mie resonances (Jahani & Jacob, 2016). These modes, named after Gustav Mie, were first proposed in the early 20th century (Mie, 1908) and used alongside effective medium theory in the 1940's to demonstrate how both the effective permeability and permittivity can be achieved in an all-dielectric material system (Lewin, 1947). Mie resonances, at the lowest order modes, possess fields that appear as electric or magnetic dipoles. An example of such modes (that are used regularly throughout this dissertation) is pictured in Figure 1.2 for silicon nanopillars. More complex modes such as the electric and magnetic quadrupole, octupole, and so on will appear at higher energies. The electric dipole resonance (E_{dp}) possesses fields that oscillate between the boundaries of the nanoparticle along the polarization axis, which generates a circulating magnetic field due to Ampère's Law (Maxwell's equations). Similarly, the magnetic dipole resonance (H_{dp}) is excited perpendicular to the polarization axis and generates a complementary circulating electric field. Notably, the fields are more confined within the resonator compared to plasmonic structures. Additionally, the mode is distributed volumetrically throughout the particle instead of being localized to the surface. While this results in poorer field confinement compared to metallic nanostructures, it also creates opportunities to combine multiple modes within the same mode volume to engineer new combinations that interact with light in unique ways.

1.3. From Passive to Active Metamaterial Performance

1.3.1. Increasing Application Space due to Tunability

While the metamaterial community has been able to produce many exciting ultrathin optical devices, most designs are passive, meaning that their optical properties are fixed once they are made. The application space of meta-optics whose properties can change as a function of some external stimulus is much larger than that of passive devices, and as a result there has been a surge of research in the past ten years to engineer active meta-optics with the capability of actively modulating the amplitude and/or phase of light. As interest in dynamic metasurfaces has grown, many competing techniques have evolved that have worked to integrate sensitive materials with resonant elements in metasurfaces to create active devices that have greater modulation depths, faster switching speeds, and lower power consumption than previous attempts. By expanding the scope of metamaterials to include active performance, the potential viability of meta-optics as realistic replacements for existing bulky technologies continues to grow.

1.3.2. Modulation Methods

Many techniques to modulate the optical properties of metamaterials have been developed in the past decade or so. One of the most common methods is through the application of an electrical field through a sensitive element in a capacitive structure, such as a quantum well (Wu et al., 2019), 2D material (Miao et al., 2015), or doped semiconductor with enough free carriers to generate a charge accumulation layer (H. T. Chen et al., 2009). Transparent conductive oxides (TCOs) such as Indium Tin Oxide (ITO) are commonly used for this purpose due to their highly tunable carrier concentration. Similarly, one can use a current to directly inject charge carriers into a region of the metamaterial, changing its permittivity and resonant energy (Shcherbakov et al., 2017). It is possible to achieve the same effect for short timescales by optically pumping carriers into the conduction band to change a material's permittivity until they thermalize and drop back into the valence band (Shcherbakov et al., 2017). More generally, optical pumping is commonly used in ultrafast experiments for nonlinear processes to achieve modulation in wavelength ranges that are normally difficult to access, such as the ultraviolet (Semmlinger et al., 2018).

Another large portion of tunable metasurfaces rely on phase-change materials such as Germanium-Antimony-Tellurium (GST) or Vanadium Dioxide (VO_2). These materials undergo a structural and electronic phase transition upon reaching a critical temperature (approximately 67°C for VO2, 170°C for GST) that produces large changes in the refractive index. By concentrating light into the phase-change material, it is possible to produce large changes in the optical spectrum depending on the material phase (L. Liu, Kang, Mayer, & Werner, 2016; Z. Zhu, Evans, Haglund, & Valentine, 2017).

There have been many investigations of changing the dielectric environment of meta-atoms to alter their resonant behavior. One of the most well-studied combinations is using liquid crystals to alter the permittivity surrounding a resonant particle (Sautter et al., 2015). By applying a field, liquid crystals can re-orient along the polarization axis and affect the effective permittivity. Similarly, meta-atoms have been embedded in elastomers and strained via stretching to change the periodicity of the metamaterial and alter the response by changing the degree of coupling between neighboring meta-atoms (Karvounis et al., 2019). Additionally, MEMS-type structures have been extensively studied to alter the positioning of resonant structures to alter their behavior (W. M. Zhu et al., 2011).

1.3.3. Current State-of-the-Art in Active Meta-Optics

While many different actuation mechanisms have been investigated, they each have benefits and drawbacks. A summary of recent progress in dynamic metasurfaces, separated by modulation mechanism, is provided in Table 1.1 (Q. He, Sun, & Zhou, 2019). Strain-based engineering has resulted in resonant frequency tuning ranges of 27% in the visible range (Tseng et al., 2017), but utilizing stretchable substrates such as PDMS to change the metasurface lattice constant is always limited by the yield of the stretchable film, which is less than 10% for reversible control (Gutruf et al., 2016). Liquid crystal-based active metamaterials have demonstrated large modulation depths (>70%) in frequency ranges from the GHz to visible, but the response time is slow (Savo, Shrekenhamer, & Padilla, 2014). Carrier injection techniques can achieve modulation of approximately 50% at frequency ranges ranging from the THz to visible, but the speed of the response is limited by the carrier lifetime and generally require large power (bias voltages) to achieve maximum performance (H. T. Chen et al., 2009). Phase change materials have been demonstrated to possess large modulation depth and can switch quickly, but material choices are

Tuning Approach	**Materials**	**External Knots**	**Operational Energy**	**Modulation Depth**	**Modulation Speed**
Carrier Doping	Semiconductors	Electrical	THz to Visible	55%	2MHz
		Optical	THz to Visible	90%	NA
	Graphene	Electrical	THZ to NIR	243°	NA
	TCO	Electrical	NIR to Visible	30%	10MHz
Phase Transitions	Liquid Crystals	Electrical	GHz to Visible	70%	NA
		Thermal	GHz to Visible	12°	NA
		Optical	GHz to Visible	18%	NA
	VO_2	Electrical	THz to Visible	80%	1KHz
		Thermal	THz to Visible	20%	NA
		Optical	THz to Visible	38%	NA
	GST	Electrical	THz to Visible	100%	NA
		Thermal	THz to Visible	NA	NA
		Optical	THz to Visible	400%	10MHz
Mechanics	MEMS	Electromechanical	GHz to Visible	31%	1KHz
		Electromechanical	GHz to Visible	8%	1MHz
	Elasticity	Mechanical	GHz to Visible	27%	NA
	Microfluidics	Microfluidics	GHz to Visible	NA	62Hz

Table 1.1: Comparison of most common approaches for dynamic metasurfaces, including the use of semiconductors, 2D materials, TCOs, liquid crystals, phase-change materials, MEMS, elasticity, and microfluidics.

scarce for reasonable operating temperatures and the undesirable loss in the metallic states of many metal-insulator phase-change materials limits their applicability. There is much progress being made in this area, but a complete solution that achieves large modulation depth and speed, low input power, and high efficiencies remains an elusive goal.

When considering metasurface-based phase modulation, the most successful techniques have been gate-tunable devices that rely on carrier density to spectrally shift resonant modes (Kafaie Shirmanesh, Sokhoyan, Pala, & Atwater, 2018; Sherrott et al., 2017). However, the reflected intensity remains both low and variable during this process. To make phase modulation more applicable, such modulation depths must be preserved while maintaining large (and constant) amplitude.

1.4. Motivation and Organization of the Dissertation

Since their first experimental realization at the turn of the millennium, metamaterial optics has grown into a popular subfield of nanophotonics where a toolbox of functionality has been realized through clever design of resonant meta-atoms. As demand for technology with more power in smaller form factors continues to rise, meta-optics provide a unique solution for ultra-compact and customizable performance where naturally occurring materials cannot. Furthermore, the application space of metamaterials expands tremendously when considering ultrathin devices whose behavior can change via user input. However, the amount of control over optical properties is limited depending on the choice of material and modulation method, and thus far there is still much work to be done in order to successfully realize complete control over both the amplitude and phase in a variety of spectral bands. We must go beyond what has been demonstrated if we are to successfully miniaturize and evolve past the current state of optical technology.

In this thesis, I will present my efforts to explore and surpass the limits of metasurface optics by combining electromagnetic modes of dielectric particles and tunable media in unique ways. By harnessing and enhancing light-matter interaction in new material systems, my goal is to realize avenues towards novel and tunable devices for infrared applications in an ultra-compact footprint.

In Chapters 2 and 3, we demonstrate how a uniquely lossy, dispersive, and high-permittivity medium affects dielectric modes in meta-atoms. We then show that overlapping orthogonal modes in such an environment can result in narrow-band and near-unity emissivity in the long-wave infrared. This is accomplished by creating Huygens surfaces out of 3C-SiC near the TO phonon energy. Additionally, the metasurface is highly insensitive to the incident angle and is transmissive off-resonance. Using FTIR spectroscopy and thermal emission measurement, we achieve 78% absorptance with a quality factor of 170 at an operating wavelength of 13μm from an array of resonators 2μm tall. Due to its simple architecture and high quality, this design is a strong candidate for future narrow-band IR sources.

In Chapter 4, we outline a method to realize a dynamic metasurface that operates in transmission at telecom wavelengths. By harnessing the combination of epsilon-near-zero (ENZ) modes in transparent conducting oxides and fields from Huygens modes in dielectric resonators, we can modulate the absorption with an on-state that is near-unity in transmission. We create such a device and observe a maximum experimental transmittance of 70% and modulation depth of 31%. By doing so, this architecture offers a unique solution for compact spatial light modulators and/or tunable filters in the near-IR.

In Chapter 5, we design an ultrathin optical limiter by integrating VO_2, a phase-change material known for its near-room-temperature threshold (340K), with an all-dielectric metasurface.

This structure also supports a Huygens mode with characteristically high transmittance in the on-state. The limiting behavior of the device triggers when the incident intensity grows strong enough to trigger the metal-insulator transition of VO_2. These devices are experimentally realized, achieving 7.7dB transmission contrast with an off-state transmission of -4.1dB at an operating wavelength of 1.24μm. Due to the large cutoff efficiency and transmissive architecture, we believe this optical limiter design can contribute to highly secure real-time detection and sensing applications without the threat of overheating or damaging equipment.

Chapter 6 details my efforts to design and create a reflective metasurface that modulates phase by integrating dielectric resonances with intersubband transitions (IST) in multi-quantum well (MQW) structures. Using the quantum confined Stark effect, the IST energy can be tuned towards or away from the magnetic dipole Mie mode energy, governing the strong coupling response. We provide a resonator architecture that ensures a constant reflection amplitude (0.6) with a phase tunability of nearly 180 degrees. Further, this geometry in sensitive to the incident polarization, allowing for tunable waveplate functionality by altering the phase delay between orthogonal incident polarization states. By further investigating this approach, we believe this metasurface design can serve as a strong candidate for fast and highly adjustable ultrathin phase modulators.

Finally, Chapter 7 summarizes the results presented in this dissertation and provides potential avenues towards future research. Additionally, this section discusses the main challenges that currently limit the use of such technologies outside of research settings and provides some recent developments that could alleviate those issues in the future.

CHAPTER 2

Consequences of Large Permittivity and Dispersion on Mie Resonances

2.1. Introduction

As we have seen in Chapter 1, electromagnetic metasurfaces often use the resonances of subwavelength structures to manipulate the optical properties of materials (Genevet, Capasso, Aieta, Khorasaninejad, & Devlin, 2017; Holloway et al., 2012; Yu & Capasso, 2014). Dielectric metasurfaces based on Mie resonances have become a popular choice in recent years due to their low-loss and rich mode structure compared to plasmonic particles (Bezares et al., 2013; Genevet et al., 2017; Spinelli, Verschuuren, & Polman, 2012). At optical frequencies, previous dielectric metasurfaces have employed materials such as silicon that have a relatively low permittivity ($\varepsilon \cong 12$) with minimal dispersion, thus limiting the implementation of nanoscale resonators to the visible and near-infrared spectral range. While Mie modes in highly dispersive media have been observed in the long-wave infrared (Long et al., 2013; Schuller, Zia, Taubner, & Brongersma, 2007), there has been no work examining more complex behavior and design principles, such as determining the role of modal overlap. This chapter will outline the main consequences of using high-permittivity (due to the spectral vicinity of other resonant modes) media and large dispersion on the character, spectral location, and quality factors of Mie dipole modes. Understanding how these modes behave when employing constituent materials with such extreme properties could open new doors for controlling light via resonant nanostructures, as we will explore in later chapters.

2.2. Effects of Large Permittivity

As we have seen in Section 1.2.2, the lowest-order Mie modes in dielectric resonators exhibit electric and magnetic dipole-like fields with the spectral location of the resonances being dictated by the size and aspect ratio of the resonator (A. Evlyukhin, S. Novikov, U. Zyweitz, R. Eriksen, C. Reinhardt, S. Bozhevolnyi, 2012; Bezares et al., 2013). While these features have been well-studied in low-index and nondispersive dielectrics such as silicon (See Sections 1.2.2 and 3.2), the same cannot be said for more exotic materials that possess much larger ($\varepsilon_r > 100$) permittivity combined with dispersion and loss. These parameters exist near strong material resonances such as phonon modes in polar dielectrics. By studying the evolution of Mie resonances in such an environment, we aim to understand and control the various degrees of freedom that govern their resonant characteristics in the far field. This not only interesting from a fundamental physics point of view, it will also prove useful when discussing spectrally overlapping modes for engineering new types of ultrathin optical devices (as seen in Section 3.3).

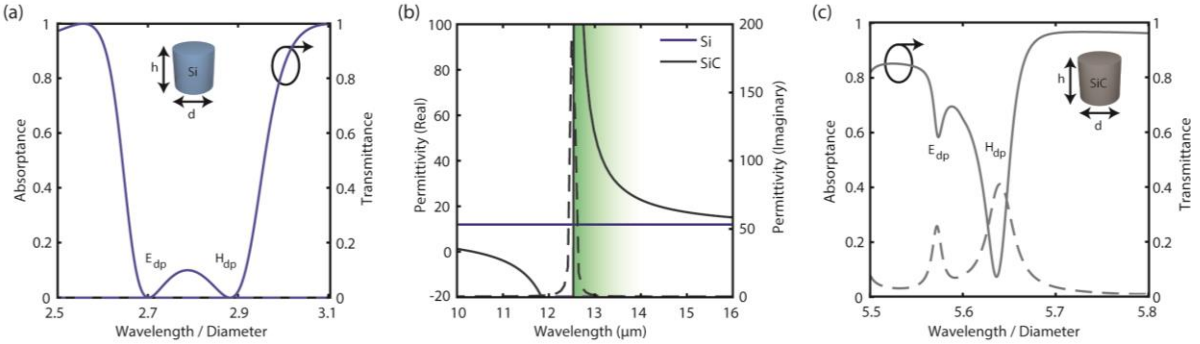

Figure 2.1: Simulated performance of Si and 3C-SiC metasurfaces. (a) Absorptance for an array of Si nanopillars with diameter d = 2.32 μm, height h = 1.28 μm, and a period p = 4.66 μm. The two modes E_{dp} and H_{dp} represent the electric and magnetic dipole Mie resonances, respectively. (b) Real (solid) and imaginary (dashed) permittivity of 3C-SiC as a function of wavelength. The design in (c) operates on the low-frequency side of 3C-SiC's surface-phonon polariton (SPhP) resonance, shaded in green. (c) Absorptance (dashed) and transmittance (solid) for an array of 3C-SiC nanopillars with the same dimensions as in (a). In both (c) and (a), the x-axis is normalized with respect to the resonator diameter.

To begin, consider the transmittance and absorptance spectrum of an array of lossless silicon nanopillars displayed in Figure 2.1(a). The two dips in the transmittance correspond to the electric dipole (E_{dp}) and magnetic dipole (H_{dp}) Mie resonances. To understand how these modes are modified in regions of high permittivity and dispersion we utilize 3C-SiC, a polar dielectric crystal, as a model material. The permittivity of SiC is plotted in Figure 2.1(b) and is given by:

$$\varepsilon(\omega) = \varepsilon_\infty + (\varepsilon_{st} - \varepsilon_\infty)\frac{\omega_{TO}^2}{\omega_{TO}^2 - \omega^2 - i\gamma\omega} \quad (3)$$

Here, $\varepsilon_\infty = 6.03$ is the high-frequency permittivity, $\varepsilon_{st} = 9.25$ is the static permittivity, $\gamma = 0.255$ THz is the damping frequency, and $\omega_{TO} = 23.75$ THz is the wavelength of the 3C-SiC transverse optic (TO) phonon, a vibrational resonance stemming from the bonding behavior and difference in atomic weights of silicon and carbon. The presence of the TO phonon at 12.62μm results in a metallic response ($\varepsilon_r < 0$) on the high-frequency side of the phonon mode that extends up to the longitudinal optic phonon where the permittivity crosses through zero (Caldwell et al., 2015b). This spectral range is referred to as the Restsrahlen band and it is within this range that SPhPs can be supported. On the low frequency side of the TO phonon there exists a spectral region where the material is a very lossy and highly dispersive dielectric, with real permittivity values in excess of a few hundred (Powell, Christiansen, Gregory, Wetteroth, & Wilson, 1999). If we keep the dimensions of the cylinder in Figure 2.1(a) constant, but change the material to 3C-SiC, we obtain the spectra in Figure 2.1(c). From a glance, we see that the Mie modes have shifted in wavelength from the NIR to the long-wave infrared, grown closer together spectrally, and incorporated absorption losses when transitioning from silicon to 3C-SiC.

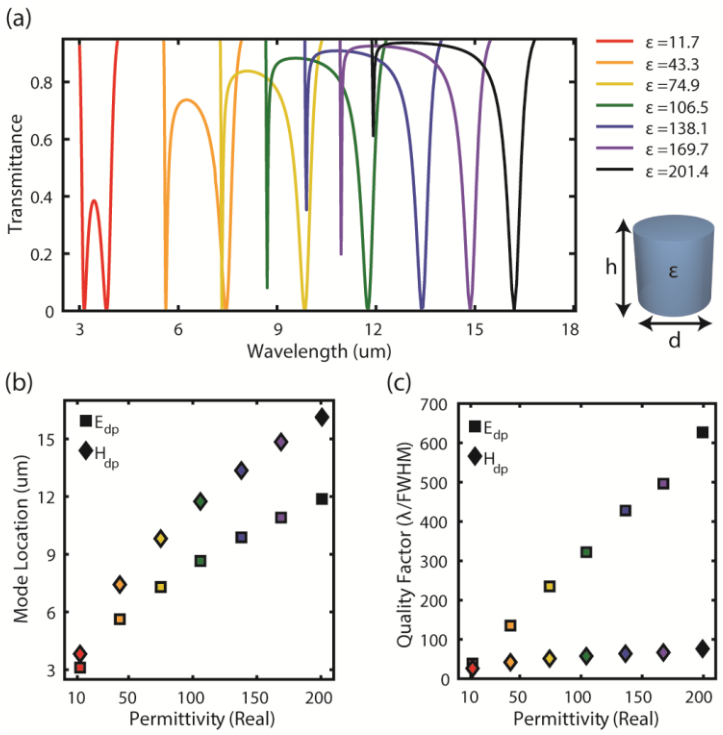

Figure 2.2: Study of simulated dipole Mie resonance position and quality factor as a function of permittivity. (a) Transmittance of an array of nanopillars with dimensions h = 0.9μm, d = 1.1μm, and period p = 2.2μm for various permittivities. Only the electric and magnetic dipole modes have been plotted for clarity. (b) Spectral position of the electric and magnetic dipole resonances for the permittivities in (a). (d) Full-width half-maxima of the electric and magnetic dipole modes in (a).

One can better understand the mechanisms responsible for adjusting the Mie modes by considering them independently. To illustrate this, we first examine the effects of the real component of the permittivity alone on Mie resonances. Figure 2.2(a) shows the transmittance of the electric and magnetic dipole modes for cylindrical nanopillar arrays of various permittivities. Since the permittivity controls the effective wavelength inside the material ($n = \frac{c}{v} = \sqrt{\varepsilon_r}$), we expect to see these modes increase in wavelength when in the permittivity is increased. Indeed, we observe that tuning over a large spectral window (~3-16μm) is possible by altering the permittivity of the cylinders by over an order of magnitude. Alternatively, this means that by increasing the permittivity, it is possible to generate Mie modes at the same wavelength with smaller particle sizes. This is reflected in the 3C-SiC metasurface spectra in Figure 2.1(c) since the modes have larger wavelength/diameter ratios than the silicon metasurface. Additionally, we observe that while both modes (electric and magnetic) increase in wavelength as the permittivity is increased, the magnetic mode is more affected, as shown in Figure 2.2(b). The linewidths and quality factors are

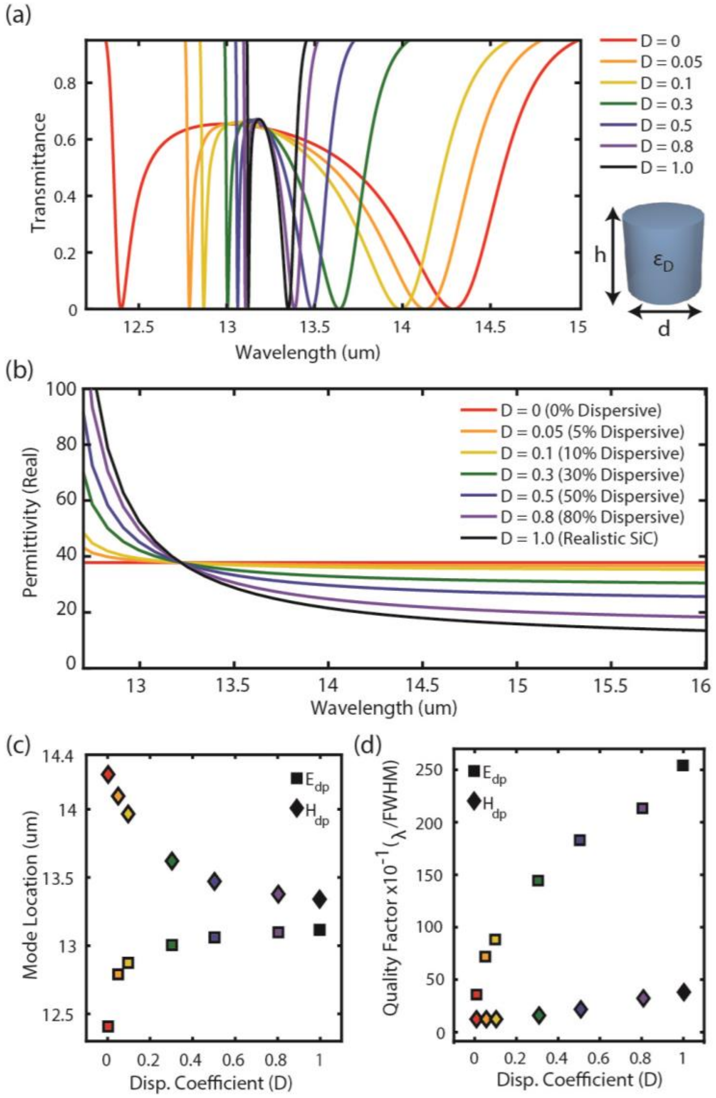

Figure 2.3: Study of simulated dipole Mie resonance position and quality factor as a function of dispersion. (a) Transmittance of an array of nanopillars with dimensions h = 2.75μm, d = 1.52μm, and period p = 5.54μm with various permittivity functions (defined by the parameter D). (b) Permittivity functions for various D. A larger value of D corresponds to increased dispersion near the dipole resonance frequency of the metasurface. (c) Spectral position of the electric and magnetic dipole resonances in (a) for the permittivity functions in (b). (d) Quality factor of the electric and magnetic dipole resonances in (a) for the permittivity functions in (b).

altered as well and are pictured in Figure 2.2(c). The magnetic dipole mode possesses circulating electric fields around the boundary of the resonator (See Section 1.2.2), allowing more energy to couple to free space. By comparison, the electric dipole has its strongest fields in the middle of the resonator and possesses lower field leakage. Therefore, the magnetic dipole modes possess a larger linewidth (and lower QF) than their electric counterparts.

2.3. Effects of Large Dispersion

Since large permittivity is achieved via resonances in materials (such as the TO phonon in 3C-SiC), dispersion is a byproduct and must be considered. We can understand the effect of dispersion on Mie modes by varying its presence in the constituent cylinders of the metasurface described in Figure 2.2. If we begin with a dispersion-less model material and incorporate dispersion by increasing the permittivity at lower wavelengths and decreasing the permittivity at higher wavelengths, modes that exist in this region will be spectrally compressed closer together. This effect is described in Figure 2.3(a). The underlying model is a dummy permittivity function that is a weighted average between a completely nondispersive medium and a realistic model for 3C-SiC (Equation 3). This is expressed as $\varepsilon_D(\omega) = D\varepsilon_{SiC}(\omega) + (1 - D)x$, where $\varepsilon_{SiC}(\omega)$ is the dispersive permittivity function of 3C-SiC, x = 38.8 is a static value to represent the permittivity of a nondispersive material, and D is the dispersive-ness proportionality constant. This can be seen in Figure 2.3(b) for several values of D. We chose the value of x to be 38.8 since this is the average value of $\varepsilon_{SiC}(\omega)$ at the wavelengths between the electric and magnetic dipole resonance (13.25μm). Therefore, by varying the value of D and examining the evolution of the resonances near this frequency, the role of dispersion is isolated. The spectral location of the electric and magnetic dipole modes as a function of D is tracked in Figure 2.3(c). As the medium becomes more dispersive, the two resonances grow closer together in energy. This is expected since adding dispersion to the model will increase the permittivity at wavelengths below 13.25µm, decreasing the wavelength inside the material, and red shift any resonances in this regime. Similarly, adding dispersion to the permittivity decreases it at wavelengths above 13.25µm, increasing the wavelength inside the material, and blue-shifting resonances in this region. Notably, this compression will remain regardless of our choice of x; we have simply chosen its value here to most conveniently demonstrate the effect. Additionally, the quality factor of the resonances is affected by including dispersion. Figure 2.3(d) illustrates that as D is increased, the spectrum is compressed around the wavelength corresponding to a permittivity of x (13.25µm), which decreases the linewidths of the resonances and increases their quality factors. From this study, we can conclude that engineering Mie resonances in a highly dispersive medium or in a material with large permittivity can be beneficial for obtaining high-quality factor resonances. Figures 2.1(a) and 2.1(c) support this claim, as the electric and magnetic Mie modes in the 3C-SiC metasurface have much smaller linewidths than the analogous modes in the silicon metasurface.

CHAPTER 3

Near-Unity and Narrow-band Metasurface Thermal Emitters via Extreme Material Parameters

3.1. Introduction

Extreme material properties, such as those in the spectral vicinity of strong absorptive resonances (e.g., TO phonons, SPRs) can yield new design freedoms; yet, they are naturally accompanied by increased absorption loss (Kramers, 1927; Kronig, 1926). However, one application for such metasurfaces where this absorption loss can be harnessed is in tailoring thermal emission or absorption (Inoue, De Zoysa, Asano, & Noda, 2015). Thermal emission in the mid-infrared (mid-IR) is used in several applications, such as nondispersive infrared sensing (Hodgkinson & Tatam, 2013), IR spectroscopy, beacons, and thermophotovoltaic power generation (Lenert et al., 2014). Many of these applications would benefit from a narrow spectral response; therefore, there is a strong motivation to engineer narrow-band thermal emission sources with high efficiencies.

Recent designs for narrowband thermal emission generally contain diffractive elements, such as gratings and photonic crystals. These have been implemented with a variety of materials, such as gold (Biener, Dahan, Niv, Kleiner, & Hasman, 2008), zinc selenide and germanium (H. Zhu et al., 2018), polar dielectrics such as silicon carbide and gallium phosphide (J.-J. Greddet, R. Carminati, K. Joulain, J.-P. Mulet, S. Mainguy, 2002; Lee, Fu, & Zhang, 2005; Schuller, Taubner, & Brongersma, 2009; T. Wang et al., 2017), gallium arsenide-based quantum wells (Asano, Mochizuki, Yamaguchi, Chaminda, & Noda, 2009; De Zoysa et al., 2012; Inoue, De Zoysa, Asano,

& Noda, 2013, 2015, 2016; Inoue, Zoysa, Asano, & Noda, 2014), and graphene-integrated cavity structures (H. Li, Wang, & Zhai, 2016; K. Li et al., 2017). While some of these techniques are capable of generating long-wave infrared emission with quality factors above 100, they also suffer from dispersion as a function of the viewing angle (Biener et al., 2008; J.-J. Greddet, R. Carminati, K. Joulain, J.-P. Mulet, S. Mainguy, 2002; H. Li et al., 2016; Xianliang Liu et al., 2011; Mason et al., 2011; H. Zhu et al., 2018), which increases the effective linewidth as the emission is typically integrated over a range of viewing angles. Subwavelength elements can remedy this issue and plasmonic metamaterials have been used for this purpose, but the large ohmic loss in metals leads to quality factors on the order of 10 resulting in thermal emission with excessively broad bandwidths (Fleming et al., 2002; S. Y. Lin et al., 2003; Mason et al., 2011; Sai & Yugami, 2004).

In order to achieve both angular-insensitive and narrowband emission, materials with a large index of refraction are required to create resonant structures that are more deeply subwavelength than low-index materials. Successfully reducing sensitivity to the viewing angle while maintaining or improving the quality factor with large efficiency and a simple resonator structure would be beneficial for a wide variety of application in this wavelength range, including infrared sources and beacons, free-space optical communications, and sensors.

In this chapter, an approach for achieving narrow-band, angle-insensitive, and near-unity absorptivity and emissivity using a single layer of deeply subwavelength dielectric resonators is outlined. This is accomplished by utilizing spectrally overlapped electric and magnetic dipole resonances featuring equal oscillator strength, which satisfies Kerker’s first condition (Geffrin et al., 2012; Kerker, Wang, & Giles, 1983; Videen & Bickel, 1992) resulting in cancellation of backscattering (Decker et al., 2015; Monticone, Estakhri, & Alù, 2013; Pfeiffer et al., 2014; Pfeiffer & Grbic, 2013b). While this condition would result in near-unity transmittance in the absence of loss, we demonstrate that if absorption loss is present, and the losses in the dipole modes are balanced, then the result in near-unity absorption. Further, implementing this architecture in highly dispersive and high permittivity media results in narrowband absorption and thermal emission that is insensitive to the angle of incidence up to 50° off normal. The metasurfaces are also highly transmissive off-resonance. This special type of device, which we call "balanced metasurfaces", are realized experimentally using deeply subwavelength ($\lambda_{\text{free-space}}/6.6$) 3C-SiC nanopillar arrays, from which we observe 78% absorptance with a quality factor of 170. Due to its simple architecture, high quality, and insensitivity to angle of incidence, this design could be a strong candidate for future narrow-band IR sources.

3.2. Kerker's Condition and Huygens Modes

In the late 17th century, Dutch physicist Christiaan Huygens developed the idea that every point on a wavefront is also a secondary source of outgoing waves (Huygens, 1690). This concept is critical for the foundations of diffraction and reflection in optics. Over two centuries later, English mathematician Augustus Love formalized this theory to explain that in order to have forward-propagating waves, the Huygens principle required each secondary source of radiation to be modeled as an antenna with the far-field radiation pattern of overlapped electric and magnetic dipoles, labeled as Huygens sources (Love, 1901). In more recent times, such sources have been fabricated in metallic metasurfaces to create artificial reflection-less sheets, known as Huygens surfaces (Monticone et al., 2013; Pfeiffer & Grbic, 2013b). This is accomplished by creating an artificial magnetic response that is equal in strength to the electric response of resonant meta-atoms

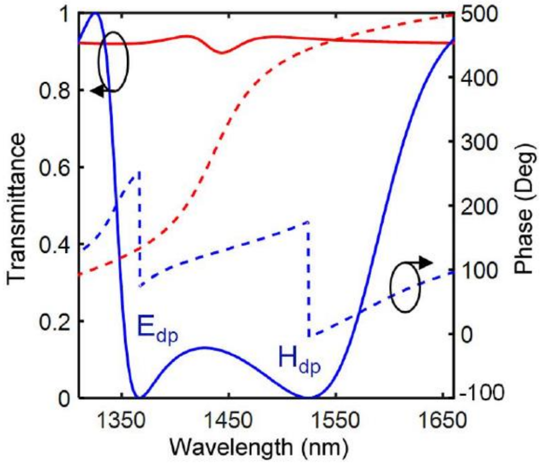

Figure 3.1: Amplitude and phase response of the Huygens mode in dielectric metamaterials. Simulated transmittance and phase of resonators ($\varepsilon_r = 13.7$) using finite element frequency domain simulations with spectrally separated electric and magnetic dipole resonances are shown in blue. Spectra of resonators with overlapped modes (Huygens mode) are shown in red.

and spatially combining them in a metasurface architecture. When achieved ($\varepsilon=\mu$), the resulting radiation pattern exhibits zero backscattering, a feature commonly known as Kerker's first condition (Kerker et al., 1983)**.**

One advantage of working with dielectric metamaterials is the spectral location of both the magnetic and electric dipole Mie modes can be adjusted by altering the aspect ratio of the resonator (A. Evlyukhin, S. Novikov, U. Zyweitz, R. Eriksen, C. Reinhardt, S. Bozhevolnyi, 2012; Bezares et al., 2013). With the correct geometry, the electric and magnetic dipole modes can exist at the same frequency. When this occurs for two orthogonal dipole modes of equal strength, Kerker's condition is again satisfied and results in zero reflection (Decker et al., 2015; Monticone et al., 2013; Pfeiffer et al., 2014; Pfeiffer & Grbic, 2013b). Alternatively, this feature can be interpreted an interference effect: the reflected field from the electric dipole mode is equal in amplitude and opposite in phase to that of the magnetic dipole mode. When the two are spectrally overlapped, their interaction results in complete destructive interference in reflection. Therefore, if the material used to support these Mie dipole modes is a low-loss dielectric, the absorption remains small and the transmission becomes unity. Dielectric Huygens metasurfaces have been explored in the past for high efficiency wavefront manipulation due to the large (2π) phase gradient that is accumulated upon passing through the Huygens mode in frequency space. This is a direct consequence of placing two resonant modes, each of which normally accumulate a phase change of π at the same energy, as seen in Figure 3.1. Huygens modes provide a convenient path to unity transmittance at the nanoscale while providing a unique resonant environment for interaction with materials nearby the dielectric resonators. This allows for the construction of meta-optics with large transmittance outside the region of interest and in the on-state of tunable metamaterials. These concepts will be explored in more detail in Chapters 4 and 5.

3.3. Overlapping Resonances in a Lossy Medium

As we have seen in Section 3.2, overlapping two orthogonal Mie modes of equal strength in a traditional low-index and lossless dielectric results in unity transmittance (zero backscattering), known as the first Kerker condition (Kerker et al., 1983). In the metasurface community, this is often referred to as a Huygens mode (Decker et al., 2015; Monticone et al., 2013; Pfeiffer et al., 2014; Pfeiffer & Grbic, 2013b). However, if we attempt to construct a Huygens mode in 3C-SiC, a lossy dielectric, a different result emerges. To accomplish this, the aspect ratio (AR = h/d) of the 3C-SiC resonators from Figure 2.1(c) must be varied to overlap the electric and magnetic dipole Mie modes. To explore the design space for inducing such an overlap, we plot the absorption as a function of the aspect ratio in Figure 3.2(a). At large values (AR > 0.5), the electric and magnetic dipole Mie modes are spectrally separated. The blue dashed line at AR = 0.53 corresponds with the blue transmittance and absorptance curves in Figure 3.2(b). In this case, each resonance exhibits an absorptance less than 50%. Reducing the AR of the nanopillars results in convergence of the resonances and eventual spectral overlap near an AR of 0.4, as shown in Figure 3.2(a). The red dashed line corresponds with the red transmittance and absorptance curves in Figure 3.2(b), demonstrating near-unity absorptance at AR=0.41.

This special case, overlapping orthogonal Mie modes in a lossy dielectric, provides a new opportunity for metamaterial absorbers and emitters. Thanks to the TO phonon of 3C-SiC, the dielectric environment is well-suited for strong absorption or emission in the long-wave IR. The large dispersion at 13μm means the resonant absorption is much narrower than expected at these

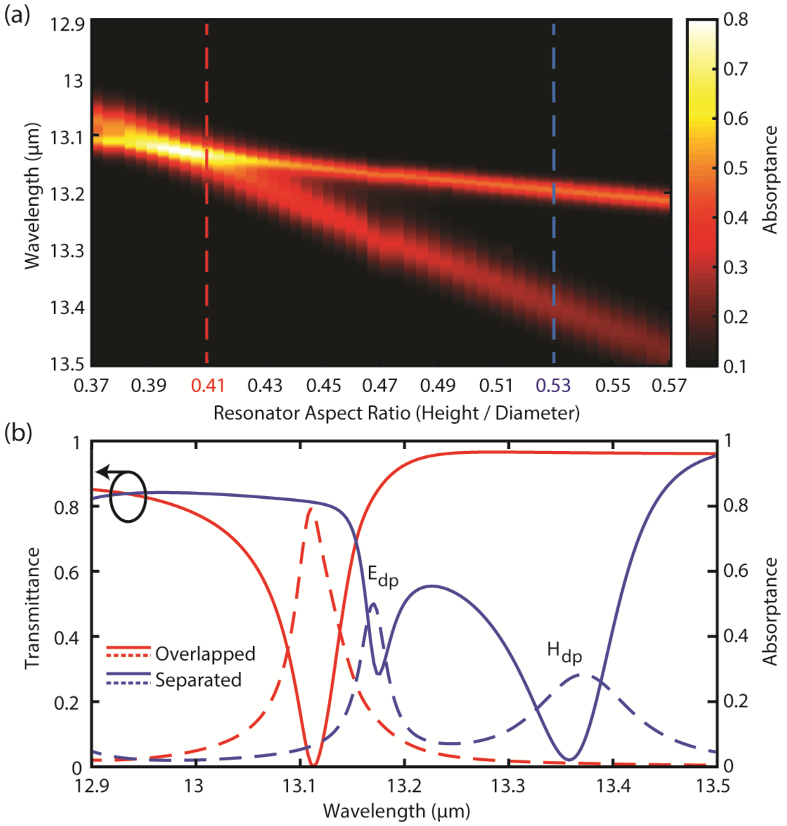

Figure 3.2: Optical response of spectrally separated and overlapped Mie dipole modes in 3C-SiC metasurfaces. (a) Absorptance of an array of cylindrical 3C-SiC nanopillars as a function of wavelength and aspect ratio. The dimensions are diameter d = 2.9μm and period p = 5.835μm, and the height is varied from h = 1.1 to 1.6μm. (b) Transmittance and absorptance of 3C-SiC nanopillar arrays for resonator geometries highlighted in (a). The blue curve represents cylinders with electric and magnetic modes spectrally separated and dimensions d = 2.9μm, h = 1.5μm, and period p = 5.835μm. The red curve represents cylinders with overlapped modes and dimensions d = 2.9μm, h = 1.2μm, and period p = 5.835μm.

wavelengths, and the imaginary permittivity enables a large absorption amplitude. The exact role of losses and the desired amount for perfect absorption will be discussed in Section 3.7. Another advantage of using this architecture for thermal emission is the transmittance remains high outside the absorption band, which is in contrast with past demonstrations of metamaterial perfect absorbers that use reflective backplanes (Bhattarai et al., 2017).

3.4. Fabrication Procedure

To create the 3C-SiC metasurfaces, we began with 4" wafers of 2μm thick heteroepitaxially grown 3C-SiC on Si. After dicing the wafer into 1x1cm^2 pieces, samples were spin coated with A4 PMMA photoresist at 4500rpm and baked using a hot plate at 180°C for 2 min. Afterward, electron beam lithography (EBL) was performed and the sample was developed using A4 PMMA as the photosensitive film and 1:3 MIBK:IPA as the developing agent. A 90nm Cr layer was

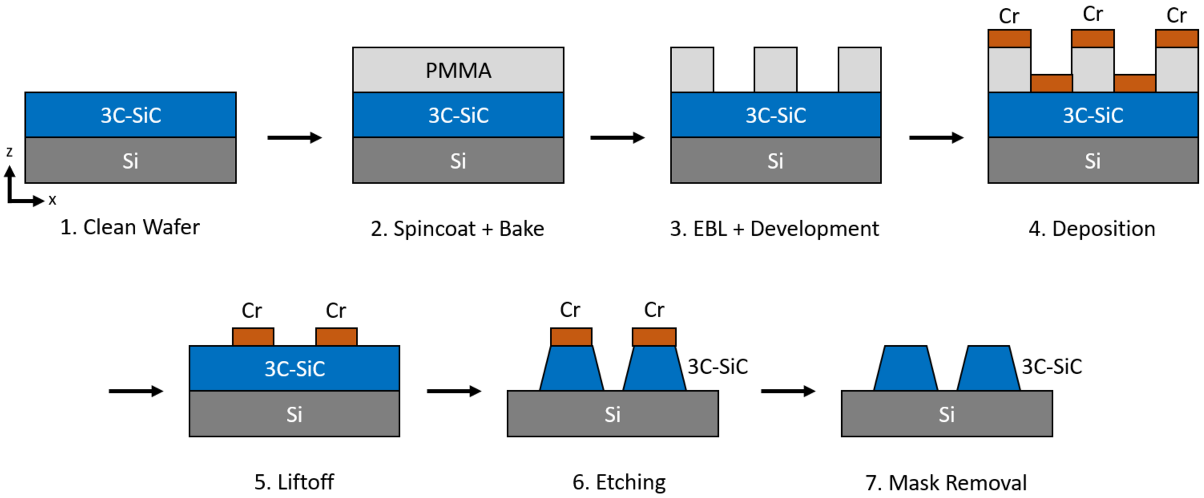

Figure 3.3: Fabrication procedure for 3C-SiC metasurface architecture. Starting with a clean wafer, we coat the sample in photoresist and use electron beam lithography and development to create a mask layer in PMMA. Then, Cr deposition followed by liftoff creates an inverse hard mask that is used as a high-selectivity layer with 3C-SiC when subjected to the reactive ion etching step. After removing the mask post-RIE, the metasurface is complete.

deposited using thermal evaporation to function as an etch mask, after which the remaining PMMA was lifted off by submerging the sample in Remover PG (Microchem) heated to 85°C.

Then, the 3C-SiC resonators were created via reactive ion etching (RIE) using a mixed-gas recipe on an SiO_2 handling wafer, stopping at the substrate. The gases involved with etching the 3C-SiC introduced a sidewall angle into the unit cell design, resulting in a frustrum architecture. Finally, the sample was submerged in Cr etchant solution to dissolve the remaining etch mask. A summary of this process is pictured in Figure 3.3, and more detailed descriptions of the EBL and RIE procedures are outlined in the appendix. All the fabrication steps described here were performed in the clean room at VINSE, and a SEM image of the completed device is pictured in Figure 3.4.

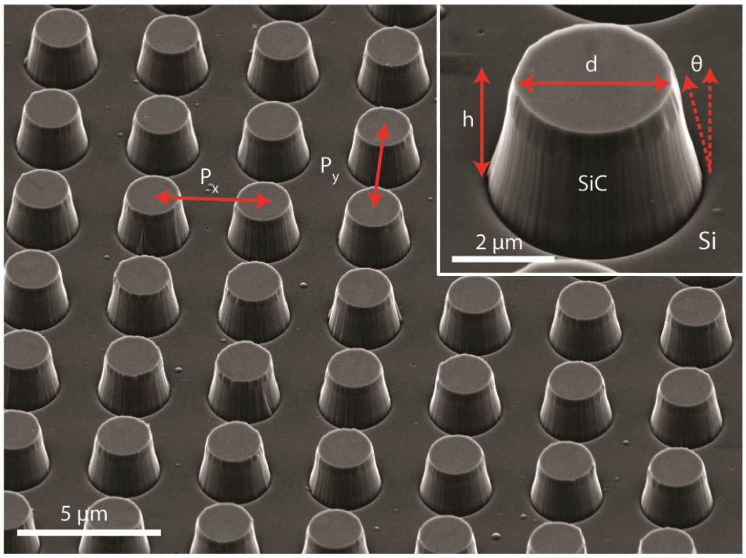

Figure 3.4: SEM image of the finished 3C-SiC metasurface device. The dimensions are $p_x = p_y = 5.25\mu m$, $h = 2\mu m$, $d = 2.3\mu m$, and the sidewall angle is $\theta=15°$.

3.5. Experimental Setup

Two experiments were conducted using the devices discussed in the previous section. First, optical measurements of the absorption and reflection spectrum in the long-wave infrared were done to verify the narrow absorptance peak created by overlapping the electric and magnetic dipole resonances. These experiments will be discussed in Section 3.6. Second, thermal emissivity measurements were conducted to verify the absorber's performance as a narrowband thermal emitter. These experiments and their results will be discussed in Section 3.8.

For measuring the absorption spectra, an MCT detector of a Bruker VERTEX 70v FTIR spectrometer was used in combination with a Hyperion 2000 microscope. The samples were aligned using a glass 5x (0.17 NA) objective in the microscope, and a Ge refractive 5x (0.17 NA) was used for the measurements since glass is not suitable for the long-wave infrared. All spectra were normalized to spectra of the substrate.

For the thermal emission measurements, a heated stage was added to the FTIR microscope (Linkam FTIR600) that raised the temperature of the sample to 250°C. The emissivity was measured using a Cassegrain reflective 15x objective with a weighted average view angle of 17° incidence. The samples were calibrated using a carbon nanotube black-body reference sample, the details of which are outlined in the appendix.

3.6. Absorption, Reflection, and Scattering Results

To validate this approach for achieving narrowband absorbers, we performed optical measurements of the absorption and reflection spectra using the resonator geometry outlined in Section 3.3 and Figure 3.4. The metasurface exhibits a peak absorptance of 78%, a QF ($\lambda/\Delta\lambda$) of 170, and a reflectance of 1% on resonance, as shown in Figure 3.5. While the peak absorption is

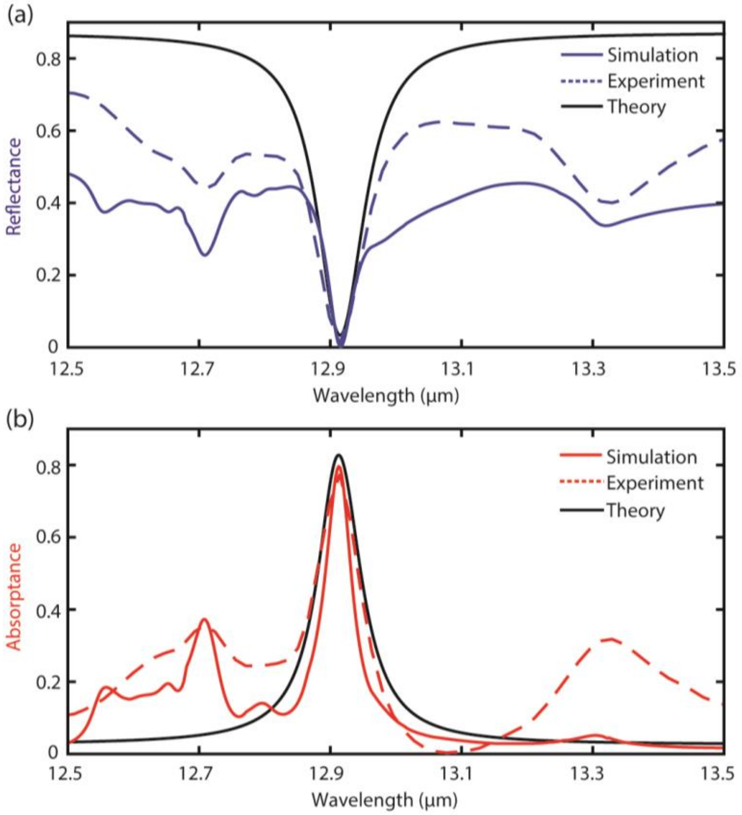

Figure 3.5: Performance of the fabricated 3C-SiC metasurfaces. (a,b) Reflectance and absorptance spectra of the theoretical, simulated, and fabricated device with dimensions $p_x = p_y = 5.25\mu m$, $h = 2\mu m$, $d = 2.3\mu m$, and sidewall angle is $\theta=15°$.

less than unity, the features of the measured spectra agree with full-wave simulations performed using CST Microwave Studio (dashed lines). This high-quality resonance is achieved with a simple and deeply subwavelength geometry (resonator diameter = $\lambda_{\text{free-space}}/6.6$). Notably, the other features seen in the spectra are higher-order Mie modes present in the particle. Due to the dispersion of 3C-SiC, higher order Mie modes will appear much closer in frequency to the electric and magnetic dipole (owing to the property outlined in Figure 2.3). Additionally, we observe a stronger background reflection signal than expected in the simulation – this can be due to several factors related to modeling or experimental error. For example, the Si substrate used may have a slightly different doping level than assumed (intrinsic), slightly changing its index and optical properties. Additionally, the reactive ion etching procedure (Step 6 in Figure 3.3) is performed for a set time based on the estimated etching rate of 3C-SiC. While the desired resonator height is 2μm, and the 3C-SiC film thickness is also approximately 2μm (verified with AFM and SEM), imperfections in the etch may result in a thin 3C-SiC layer between the resonators. This is not expected to significantly impact the results but will nevertheless reduce the transmission.

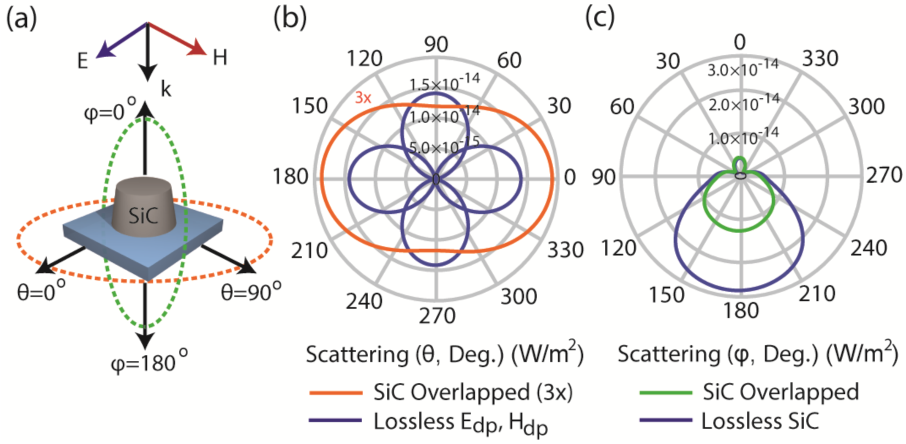

Figure 3.6: Far field scattering profiles of 3C-SiC particles with overlapped dipole modes. (a) Schematic of the unit cell geometry and map of the scattering axes. (b) In-plane scattering profile. The magnetic dipole (which radiates primarily at θ = 0,180°) dominates the response. (c) Out of plane scattering profile. Most of the energy (that is not absorbed) is transmitted at φ = 180°.

In theory, overlapping two lossy resonances should result in a maximum absorption of 100%; here, we only observe 78% and 81% absorption in the experimental and simulated spectrum, respectively. To better understand the factors dictating peak absorption in our system, we examine the simulated scattering cross section of the resonator. For reference, in Figure 3.6 we plot the electric and magnetic dipole scattering profiles in the xy-plane (φ = 0) for a lossless resonator with perfectly overlapped resonances. In the 3C-SiC resonators, the combined response in the xy-plane possesses far less scattering due to the presence of absorption loss. More interestingly, we observe that the minimal scattered light has the character of the magnetic mode. In the xz-plane (θ = 0), we notice that the light is scattered almost exclusively in transmittance for the 3C-SiC resonators (Figure 3.6(c)). Again, the losses mitigate the scattering amplitude when compared to the same resonator in the absence of loss, but the directionality of the scattered light remains the same.

3.7. Analytical Model for Overlapped Lossy Dipoles

The scattering results can be put into context by employing an analytical model approximating the resonators as orthogonal electric and magnetic dipoles. The resonant behavior can be understood by comparing the strengths of the effective magnetic and electric polarizabilities of the array ($\alpha_{mm}^{eff}, \alpha_{ee}^{eff}$), and the absorption when the two are overlapped is expressed as (Alaee, Albooyeh, & Rockstuhl, 2017):

$$\mathrm{A} = 1 - |\mathrm{r}|^2 - |\mathrm{t}|^2 = 1 - \left|\frac{\mathrm{ik}}{2\Lambda^2}\alpha_{\mathrm{ee}}^{\mathrm{eff}} - \frac{\mathrm{ik}}{2\Lambda^2}\alpha_{\mathrm{mm}}^{\mathrm{eff}}\right|^2 - \left|1 + \frac{\mathrm{ik}}{2\Lambda^2}\alpha_{\mathrm{ee}}^{\mathrm{eff}} + \frac{\mathrm{ik}}{2\Lambda^2}\alpha_{\mathrm{mm}}^{\mathrm{eff}}\right|^2 \qquad (4)$$

In Equation 4, r is the reflection coefficient, t is the transmission coefficient, Λ is the period of the array, $\mathrm{k} = \omega/\mathrm{c}$ is the wavenumber at angular frequency ω, and $\alpha_{\mathrm{mm}}^{\mathrm{eff}}$ and $\alpha_{\mathrm{ee}}^{\mathrm{eff}}$ are the effective magnetic and electric polarizabilities of the array, respectively. This form of the reflection and transmission coefficients comes from the electromagnetic constitutive relations ($p = \varepsilon_0 \alpha_{ee} E^{loc}$, $m = \alpha_{mm} H^{loc}$) between the induced dipole moments (*p*,*m*) and local fields of the resonators (*E*, *H*). By using Maxwell's generalized boundary conditions, it is possible to write the reflected and transmitted fields in terms of the electric and magnetic dipole moments. The form of the reflection and transmission coefficients seen in Equation 4 are obtained by dividing the reflected and transmitted fields by the incident fields, respectively ($r = E^r/E^i$, $t = E^t/E^i$). A complete derivation of this equation and accompanying constants such as the interaction term β are provided (Alaee et al., 2017). The condition of balanced dipoles with equal strength which results in zero reflection and 100% absorption is summarized in Equation 5:

$$\alpha_{\mathrm{ee}}^{\mathrm{eff}} = \alpha_{\mathrm{mm}}^{\mathrm{eff}} = \frac{1}{\beta_{\mathrm{mm}} - \frac{\mathrm{ik}}{\Lambda^2}} \tag{5}$$

Here, β_{mm} is a constant related to the interaction field and is the same for both the electric and magnetic resonances. The effective polarizabilities are normalized and described by a Lorentzian line-shape, as seen in Equation 6 for the magnetic case (Alaee et al., 2017; Sipe & Kranendonk, 1974):

$$\alpha_{\mathrm{mm}}^{\mathrm{eff}} = \frac{\alpha_{mm}}{1 - \alpha_{mm}\beta_{mm}} \;, \alpha_{mm} = \frac{\alpha_{0mm}}{\omega_{0mm}^2 - \omega^2 - i\omega\gamma_m} \tag{6}$$

The effective electric polarizability takes the same form. Here, ω_{0mm} is the resonance frequency, $\gamma_m = \gamma_{mm} + \gamma_{sc,mm}$ is the total loss component and includes γ_{mm}, the absorption or nonradiative losses and $\gamma_{sc,mm}$, the scattering or radiative losses. Finally, α_{0mm} is the oscillator strength of the resonance. In order to achieve the balanced dipole condition in Equation 5, the real and imaginary components of $\alpha_{\mathrm{ee}}^{\mathrm{eff}}$ and $\alpha_{\mathrm{mm}}^{\mathrm{eff}}$ must be equal. Equating the real components of the effective polarizabilities requires the oscillator strengths and resonant frequencies of the two dipole modes to be equal, resulting in zero reflectance. Matching the imaginary components also requires balancing the absorption and scattering losses in each resonance and will result in zero transmission if achieved. Thus, unity absorption comes from achieving balancing of both the real and imaginary components of the effective polarizabilities, a condition known in many other contexts as critical coupling. If either the absorption losses dominate or are small compared to scattering loss, the system becomes overdamped or underdamped, respectively. This comparison is illustrated in Figure 3.7.

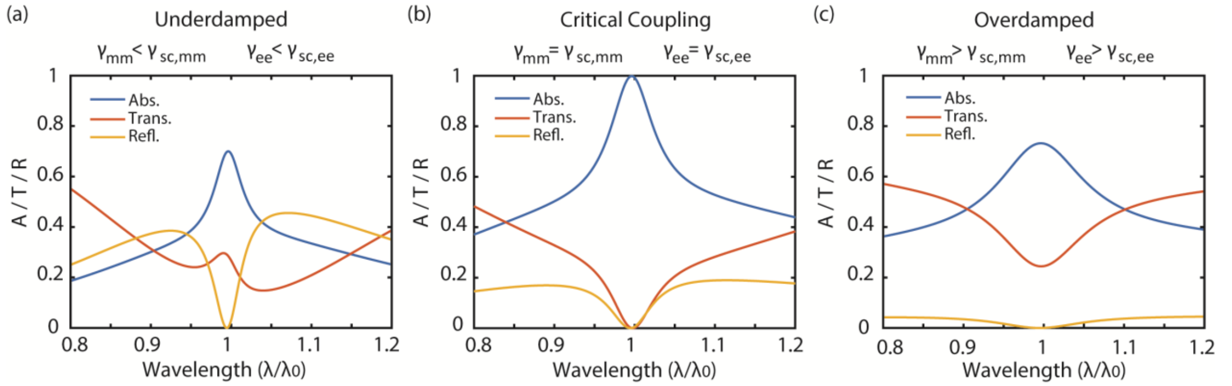

Figure 3.7: Overview of loss parameters governing critical coupling in particles with electric and magnetic dipoles with loss. For all plots, the absorptance, reflectance, and transmittance are plotted as a function of wavelength normalized to the resonance wavelength, λ_0. The absorption losses are represented by γ_{mm} and γ_{ee} for the magnetic and electric dipoles, respectively. The scattering losses are represented by $\gamma_{\mathrm{sc,mm}}$ and $\gamma_{\mathrm{sc,ee}}$. The cases of (a) underdamping, (b) critical coupling, and (c) overdamping due to the relationship between scattering and absorption losses in the resonator array.

One can also employ a reflective backplane and destructive interference of the reflection from the interfaces to achieve unity absorption (Hedayati et al., 2011; W. Li & Valentine, 2014; Xiaoming Liu, Zhao, Lan, & Zhou, 2013) or impedance matching combined with a non-resonant absorbing material of sufficient thickness(Baranov, Edgar, Hoffman, Bassim, & Caldwell, 2015; Rodríguez-Ulibarri, Beruete, & Serebryannikov, 2017). There has been related experimental work focused on spectrally overlapping lossy dipole modes by using coils to create a magnetic response (Asadchy et al., 2015) in the GHz regime. However, translating this method to the infrared is non-trivial due to significant complexity in fabrication at smaller length scales.

In our case, based on the scattering results (Figure 3.6) and the analytical model, the real part of the polarizability is close to being balanced as the reflection is close to zero. On the other hand, the imaginary components of the electric and magnetic polarizabilities are not perfectly balanced. The magnetic dipole possesses circulating electric fields around the boundary of the resonator, resulting in smaller field overlap with the lossy material and larger scattering. By comparison, the electric dipole has its strongest fields in the middle of the resonator, thus possessing larger absorption loss. Ultimately, this results in scattering into the forward direction with a magnetic dipole-like character, justifying the response in Figure 3.6(b). The black curve in Figure 3.5 corresponds to the analytical model under this scenario, namely, matched real components of the polarizability and an imaginary magnetic component that is smaller than the electric component. We estimate that the resonant frequencies are only slightly detuned ($\omega_{0ee} = 0.97\omega_{0mm}$) and the scattering losses of the two dipoles are scaled appropriately ($\gamma_{sc,mm} = 1.31\gamma_{sc,ee}$). This comparison provides good agreement between the analytical model, full-wave simulated results, and our experimental data regarding the resonance linewidth and peak absorption. Notably, since the analytical model only considers the two overlapped dipole modes, the absorption off-resonance is zero, whereas in our measured spectra and full-wave simulated results for 3C-SiC metasurfaces additional absorbing modes appear at various wavelengths. Thus, with further optimization of the resonator geometry perfect matching and unity absorption should be achievable.

3.8. Thermal Emissivity Measurements

One of the most obvious applications of strongly absorbing resonators is a long-wave infrared source based on thermal emission (Inoue, De Zoysa, Asano, & Noda, 2013b; Inoue et al., 2015b, 2014; Lee et al., 2005; Oskooi, Noda, Inoue, De Zoysa, & Asano, 2012; T. Wang et al., 2017). Due to Kirchhoff’s law of thermal radiation, the uniquely strong resonant absorption of this metasurface design also functions as a strong narrow-band thermal emitter. By integrating a

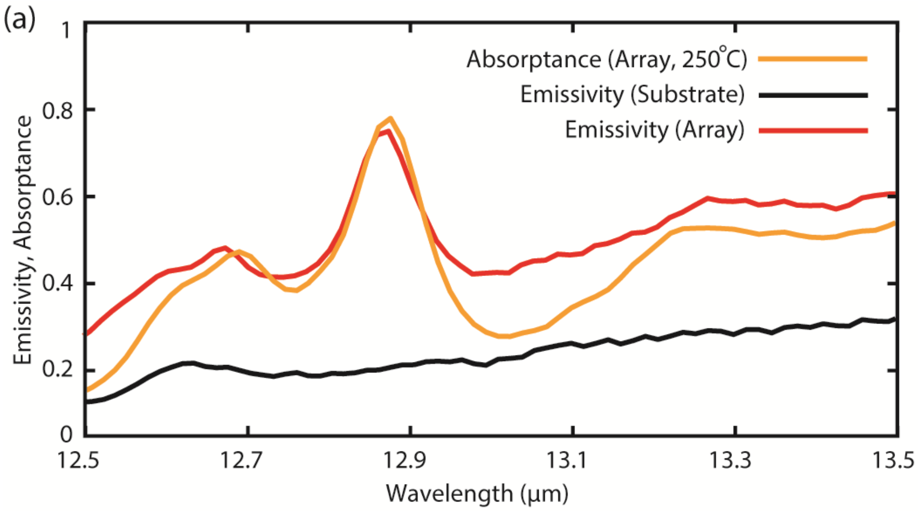

Figure 3.8: Measured emissivity and absorptance of the 3C-SiC metasurface as a function of wavelength at 250°C. The substrate emissivity is plotted since it contributes to the overall spectrum.

heated stage into our FTIR microscope, we demonstrate this by heating our sample to 250 °C and measuring the emissivity via FTIR spectroscopy. The line shape of the emissivity (Figure 3.8) matches the measured absorptance of the device. We attribute the difference between the emission spectra and simulated absorptance in Figure 3.5(b) to the emission of the Si substrate (Sato, Dai, & Wang, 1967). This is verified by measuring the absorptance of the device and the substrate at the same temperature as the emissivity measurement (Figure 3.8). Silicon displays broadband emission in the long-wave infrared due to the presence of lattice vibrations and free carriers when heated above 500K (Sato et al., 1967), which raises the absorptance and emission off-resonance in our device at high temperatures.

3.9. Design Benefits: Angle of Incidence Insensitivity and Scalability

Past Huygens' metasurfaces based on silicon are strongly dependent on the incident angle (Epstein & Eleftheriades, 2016). The angular dependence is due to unequal spectral shifts in the resonances as the angle increases as well as resonator coupling. The use of extreme permittivity materials, such as SiC in the long-wave infrared, results in significantly smaller resonators than the free space wavelength and reduced inter-pillar coupling since the index contrast between the resonator and surrounding environment is larger. At our experimental working wavelength of 12.92 μm, the real component of the permittivity of 3C-SiC is 63.1 (Figure 2.1). This enables us to use resonators with diameters that are deeply subwavelength ($\lambda_{\text{free-space}}/6.6$). These features significantly decrease the sensitivity to the angle of incidence as shown in the angle dependent absorption plots in Figure 3.9(a). The balanced 3C-SiC metasurface maintains strong absorptance (>70%) and negligible spectral shifts for incident angles from 0 to 50 degrees. Maintaining a strong and narrow absorptance peak over a large range of incident angles is critical for spectroscopic and absorption-based applications as it preserves the resonance linewidth when integrating the signal over large collection angles.

Traditionally, metasurface-based absorbers at these wavelengths have relied on reflective architectures to achieve perfect absorption (Aydin, Ferry, Briggs, & Atwater, 2011; Landy, Sajuyigbe, Mock, Smith, & Padilla, 2008; Xianliang Liu, Starr, Starr, & Padilla, 2010). The use of balanced resonators demonstrates that it is possible to achieve nearly the same result in a transmissive scheme with a single pass through the resonator layer. Since the high permittivity and dispersion increase the quality factor of the resonances, the near-unity absorption peak shown here is among the narrowest observed in metasurface-based optics at these wavelengths to date (Inoue et al., 2013b, 2014; J.-J. Greddet, R. Carminati, K. Joulain, J.-P. Mulet, S. Mainguy, 2002; Xianliang Liu et al., 2011; Oskooi et al., 2012). Additionally, since the relative spectral location of the dipole modes are tunable by changing the resonator aspect ratio, the combined dipole mode can be shifted to different frequencies so long as the aspect ratio of the resonator required to support it is maintained (A. Evlyukhin, S. Novikov, U. Zyweitz, R. Eriksen, C. Reinhardt, S.

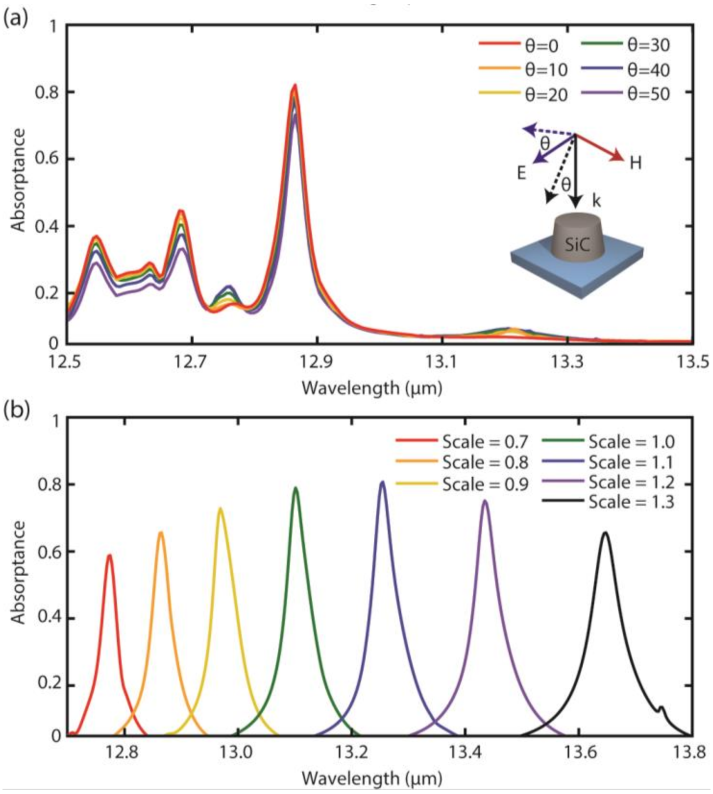

Figure 3.9: Robustness and tunability of the 3C-SiC metasurface absorber design. (a) Simulated absorptance of a metasurface with dimensions $p_x = p_y = 5.25\mu m$, $h = 2\mu m$, $d = 2.3\mu m$, and sidewall angle $\theta=15°$. The response is the same for TE and TM-polarized light. (b) Absorptance of nanopillar arrays with dimensions $p_x = p_y = 5.8\mu m$, $h = 1.2\mu m$, $d = 2.9\mu m$, and all dimensions scaled by the scaling factor. Only the overlapped Mie dipole modes are plotted for clarity.

Bozhevolnyi, 2012). This means it is possible to create absorption peaks with similar linewidths by uniformly scaling the metasurface unit cell design (period, height, and diameter), as shown in Figure 3.9(b). However, there are limits on the range of frequencies in which this applies. High absorption amplitude relies on balancing of the radiative and non-radiative loss channels present in the modes. The radiative loss component decreases as one approaches the TO phonon due to an increase in permittivity. However, the non-radiative loss component increases as the TO phonon is approached. In our case, the two are most similar when the scale factor is within 1.0-1.1 and falls out of balance when the scaling is adjusted away from these values. However, we demonstrate a tuning range of 1μm where the absorption amplitude is >50%, all while maintaining a quality factor in excess of 110.

3.10 Conclusions and Future Directions

The balanced metasurfaces outlined here have several benefits over traditional metasurface-based and photonic crystal-based thermal emitters. The large permittivity near the TO phonon of 3C-SiC enables metasurfaces with deep subwavelength periods, providing more consistent performance with varying angle of incidence in a nanoscale unit cell that is not possible with Mie resonances in non-resonant materials at such long free-space wavelengths. This compares favorably with work involving SiC emitters utilizing surface phonon polariton modes within the Restsrahlen band (Devarapu & Foteinopoulou, 2017; Dunkelberger et al., 2018; Long et al., 2013). Our design utilizes a simple architecture that allows for operation at normal incidence and maintains high emissivity and narrow linewidths throughout a wide range of viewing angles. The large permittivity and dispersion near the edge of the TO phonon also significantly narrows the linewidths of the Mie type resonances, allowing for quality factors in excess of 100. In addition, our emitter has high transmissivity around the emission peak which could be beneficial for long-wave infrared sources as the metasurface will not reflect the background thermal radiation. We believe that this combination of features makes this design a strong candidate for future narrow-band thermal sources for applications ranging from spectral signature control to infrared spectroscopy. Furthermore, while we demonstrate these aspects utilizing 3C-SiC resonator designs, this concept can be generalized to the broad suite of polar crystals, thus extending the spectral range where such emitters could be realized from approximately 6 μm out into the long-wave IR (Caldwell et al., 2015a), limited only by the accessibility of sufficient thermal energy.

CHAPTER 4

All-Dielectric Metasurface Transmission Modulators Based on Coupling Epsilon-Near-Zero Modes to Huygens Modes

4.1. Introduction

Thus far, we have explored the extreme ends of material properties to create new varieties of optical nanostructured devices. In addition to being much thinner than traditional optics, metasurfaces can be more sensitive to changes in the dielectric environment due to resonances. This sensitivity can be further amplified by concentrating fields into small volumes near (or within) the resonant meta-atoms. This allows for dynamic tunability using a range of techniques including electrical (Y. W. Huang et al., 2016; Yao et al., 2014), optical (Shcherbakov et al., 2017, 2015; Y. Yang et al., 2015), mechanical (Gutruf et al., 2016; Ou, Plum, Zhang, & Zheludev, 2013), and phase-change -based control (Abdollahramezani, Taghinejad, Nejad, Eftekhar, & Adibi, 2018), as seen in section 1.3. Creating metasurfaces with tunable properties is of great interest because it increases the application space of ultrathin optics; for example, generating tunable filters or beam steering optics with a fraction of the size of traditional components would immensely improve the SWAP (size, weight, and power) footprint in areas where miniaturization is a valuable metric for performance, such as aerospace technologies.

One method to provide this tunability is to integrate plasmonic metasurfaces with active materials. Plasmonic resonances provide large local field enhancement, which can be engineered to coincide with an actively tunable material. This allows tuning of the resonator while only changing a small region of the surrounding environment. However, the inclusion of metallic resonators generates unwanted absorption loss, and most demonstrations to date have focused on reflection-based architectures (Y. W. Huang et al., 2016; Ou et al., 2013; J. Park, Kang, Liu, & Brongersma, 2015; Yao et al., 2014). Dielectric resonators are an interesting substitute for plasmonic metasurfaces due to their low loss and large mode volumes with the fields being distributed throughout the resonator, as seen in section 1.2. Several approaches for tuning dielectric resonators have been investigated, including harnessing nonlinearity (Shcherbakov et al., 2015; Y. Yang et al., 2015), mechanical strain (Gutruf et al., 2016; Karvounis, Ou, Wu, Macdonald, & Zheludev, 2015), and liquid crystals (Komar et al., 2017; Sautter et al., 2015). However, the lack of field confinement means that a large volume of material must be modulated, which often results in increased power consumption and can also limit switching speed.

In this chapter, we present a dynamic dielectric metasurface that operates in transmission at telecom wavelengths. In order to overcome the large mode volume in dielectric resonators, we take advantage of an epsilon-near-zero (ENZ) mode in an electrically tunable indium tin oxide (ITO) layer. ITO is chosen for its convenient plasma wavelength, which can be tuned electrically so that the ENZ point is in the spectral region of interest. Operating at the ENZ point provides for large local field enhancement within the ITO, leading to dynamic absorption (and transmission) control. Here, we utilize a Huygens mode in the dielectric resonators to minimize impedance mismatch and maximize transmittance, allowing a maximum experimental transmittance of 70% and modulation depth of 31%. By doing so, this architecture offers a unique solution for compact spatial light modulators and/or tunable filters in the NIR.

4.2. Properties of Optoelectronic Thin Films (Epsilon-Near-Zero Mode)

Huygens surfaces provide a convenient route for achieving perfect transmittance using dielectric metasurfaces. For dynamic control, this response can be modified by changing the index of the resonator to disrupt the Huygens mode. Figure 4.1 demonstrates the effect of modifying the real and imaginary components of the permittivity of a cylindrical dielectric particle. If we modify the real permittivity from 13.7 to 11.7, individual dipole resonances again appear in the transmittance spectrum since the effective wavelength inside the resonator has changed. Therefore, the Huygens criterion is not satisfied, resulting in an altered spectrum and phase response. If we instead modify the imaginary permittivity from 0 to 0.7, the phase profile is unaffected since the wavelength of the magnetic and electric dipole modes is unchanged, but the transmittance is suppressed at the Huygens mode wavelength due to absorption.

In real devices, actively changing the index of an entire metasurface structure to this degree is challenging. While phase change materials can possess permittivity changes of this magnitude,

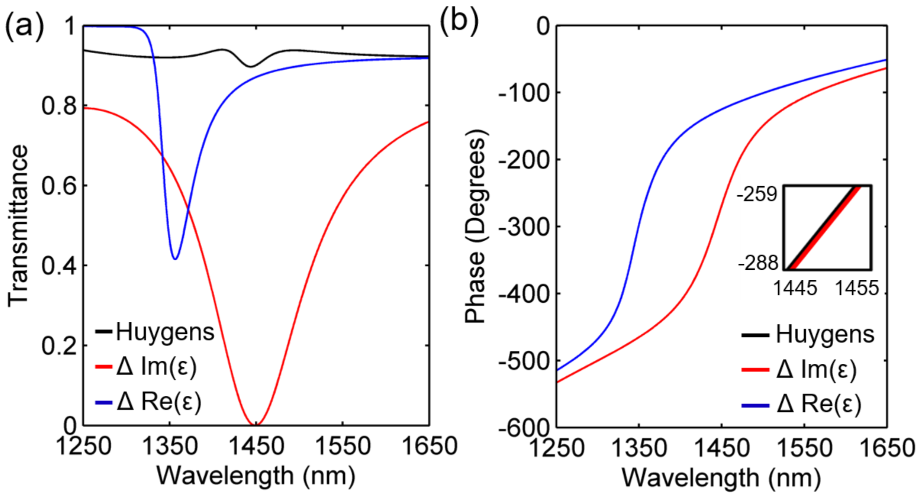

Figure 4.1: Simulated performance of Si-based metasurfaces with cylindrical resonators. (a) Transmittance plot of cylindrical resonators upon changing the real and imaginary components of the permittivity. The black curve is for Si with a real permittivity of 13.7 and imaginary permittivity of 0. The blue curve has an altered real permittivity of 11.7, and the red curve has an altered imaginary permittivity of 0.7. The dimensions of the particle are diameter d = 525nm, height h = 230nm, and period p = 800nm. (b) Corresponding phase plots for those appearing in (a). Inset: Zoomed plot of the phase data to resolve the two plots.

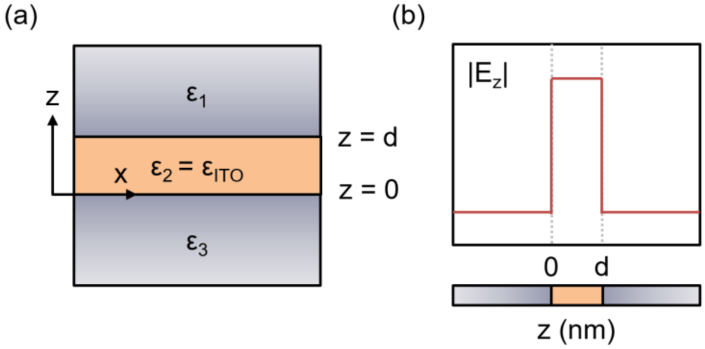

Figure 4.2: Visualization of the ENZ mode in a three-layer system. (a) Schematic of a multilayer system with an ITO film in between two dielectrics. (b) Electric field enhancement as a function of position at the frequency of the ENZ mode.

they often also exhibit large absorption losses. To make a device with high on-state transmittance and efficiency, we investigate if we can produce similar effects by changing only a small fraction of the resonator (using a thin film).

In order to achieve significant modulation with such a small volume, we take advantage of the ENZ mode in a film directly on top of the Huygens resonator (Silveirinha & Engheta, 2006). Various studies involving ENZ modes have provided unique methods for spontaneous emission enhancement (Lu et al., 2017), optical switching (De Ceglia, Campione, Vincenti, Capolino, & Scalora, 2013), and cloaking (Alù, Silveirinha, Salandrino, & Engheta, 2007). The ENZ mode manifests in a sufficiently thin (below the skin depth) plasmonic film. ITO is suitable for supporting an ENZ mode as a transparent conductive oxide (TCO) and can be represented using the Drude permittivity model:

$$\varepsilon_{\mathrm{ITO}}(\omega) = 1 - \frac{\omega_{\mathrm{p}}^2}{\omega^2 + i\gamma\omega} \tag{7}$$

Here, γ is the damping term and ω_p is the plasma frequency of the material. By modeling our system as a 3-layer material stack in Figure 3.2(a) with ε_1 = Air, ε_2 = ITO, and ε_3 =

Silicon, we can simplify Maxwell's equations to represent the mode as the following (Campione, Brener, & Marquier, 2015):

$$1+\frac{\varepsilon_1 k_{z3}}{\varepsilon_3 k_{z1}}=itan(k_{z2}d)\left(\frac{\varepsilon_2 k_{z3}}{\varepsilon_3 k_{z2}}+\frac{\varepsilon_1 k_{z2}}{\varepsilon_2 k_{z1}}\right) \tag{8}$$

Here, $k_{zi}^2=\varepsilon_i\frac{\omega^2}{c^2}-k_0$ is the wave vector in each medium perpendicular to the material interface. Importantly, two SPPs are supported in this system. One exists at the interface between ε_1 and ε_2, and the other exists at the interface between ε_2 and ε_3. If d is less than the skin depth of ε_2 (ITO), the two SPPs will begin to interact and hybridize in the thin film limit. When this occurs, the coupled modes will split into symmetric (high-energy) and antisymmetric (low-energy) SPP modes. The symmetric mode exhibits an extremely flat dispersion near the plasma frequency and the fields of the two SPPs at neighboring interfaces destructively interfere outside ε_2, leading to the field confinement seen in Figure 4.2(b). This set of features is what defines the ENZ mode (Campione et al., 2015; T. Folland et al., 2019; Runnerstrom, Kelley, Sachet, Shelton, & Maria, 2017).

One of the largest consequences of the ENZ mode is not only the field confinement within the ENZ material layer; the magnitude of such field is greatly enhanced as well. This can be understood by examining the electromagnetic constitutive relationship at material boundary of ITO and silicon for the model in Figure 4.2(a):

$$\varepsilon_{\mathrm{z,ITO}}\mathbf{E}_{\mathrm{z,ITO}}=\varepsilon_{\mathrm{z,Si}}\mathbf{E}_{\mathrm{z,Si}} \tag{9}$$

If the permittivity of ITO is nearly zero (ENZ mode, near ω_p), then the magnitude of the electric field inside ITO must grow to compensate. Therefore, if it is possible to tune the plasma frequency of ITO, it becomes possible to spectrally shift the ENZ mode, and therefore control the amount of field present in the ITO layer at a given energy.

4.3. Integration of Huygens Modes with ENZ Films: Metasurface Design

So far, we have outlined how Huygens modes provide high transmittance at a target wavelength and how ENZ modes in thin films possess large local field enhancement near a material's plasma frequency. Combining the two concepts presents an opportunity to create an ultrathin modulator with high on-state transmission and large modulation depths by controlling the local carrier concentration within the ENZ film. A potential geometry that integrates ITO as an active component with a silicon resonator supporting a Huygens mode is illustrated in Figure 4.3(a). In addition, the permittivity of ITO for two plasma frequencies is plotted in Figure 4.3(b). Since the plasma frequency depends on the number of charge carriers in the material ($\omega_p^2 = Ne^2/\varepsilon_0 m^*$), altering the local electric concentration will shift the energy at which the real permittivity crosses 0.

Importantly, the Huygens mode has strong E_z near the top of the cylindrical resonator due to the circulating electric field present in the magnetic dipole Mie mode. Using a Huygens mode instead of simply using the strong E_z in the magnetic dipole mode is necessary since we aim to create a device that operates in transmission with minimal losses in the on-state. The only way to achieve high transmittance while maintaining E_z from the magnetic dipole mode is to combine it with an orthogonal electric dipole mode. If the Huygens wavelength (λ_H) is spectrally overlapped with the ENZ mode of the ITO layer, then the z-oriented electric field in the ITO will be dramatically enhanced due to the continuity of the normal displacement field (Equation 7), as shown in Figure 4.3(c). These plots are based on an accumulation layer thickness of 3nm (Feigenbaum, Diest, & Atwater, 2010; Kwon, 2016; S. Zhu, Lo, & Kwong, 2014) and are generated from full-wave simulations using CST Microwave Studio. Field enhancement in the

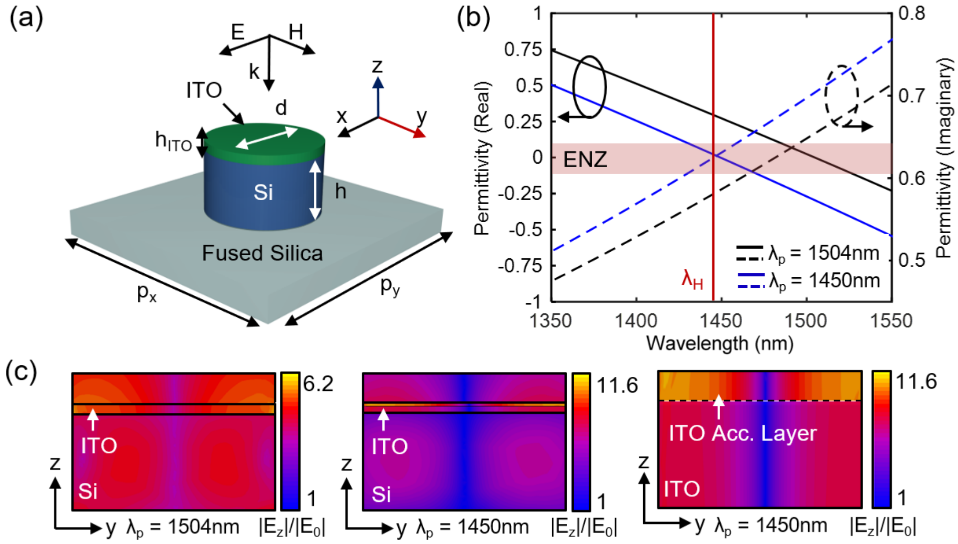

Figure 4.3: Metasurface combination of Huygens and ENZ modes. (a) Unit cell schematic for a silicon Huygens metasurface with an ITO film on top and a fused silica substrate with period p = 800 nm, h = 230 nm, h_{ITO} = 10 nm, and d = 480 nm. (b) Real and imaginary ITO permittivity as a function of wavelength. The red line intersecting with the x axis indicates the Huygens wavelength for the silicon resonator. The red bar intersecting with the y axis indicates the ENZ mode range for the ITO. (c) E_z field profiles for the resonator depicted in (a). The left and center figures contain ITO with plasma frequency spectrally separated and overlapped with the Huygens wavelength, respectively. The right figure is a zoomed-in field profile of the ITO when its plasma frequency is overlapped with the Huygens wavelength. The estimated carrier concentration in the accumulation layer and remainder of ITO are 8.6e20 e^-/cm^3 and 3.56e20 e^-/cm^3, respectively.

ITO is observed when the ENZ point of ITO coincides with the Huygens wavelength of the resonators, as shown in Figure 4.3(c). Similarly, if the ENZ mode of the ITO is tuned away from λ_H, the field enhancement disappears.

The amount of electric field present inside the ITO layer dictates the absorption loss according to $A \propto \int \varepsilon_i |E|^2 dV$. Since ε_i is finite at ITO's plasma frequency, tuning ITO's ENZ point to the Huygens mode wavelength of the underlying dielectric cylinder will couple the z-oriented electric fields from the Huygens mode to the ENZ mode in the film. The fields will be enhanced due to Equation 7, and the system will experience absorption loss, destroying the signature of the Huygens mode. If the ENZ point of ITO is tuned away from the Huygens wavelength, the Huygens

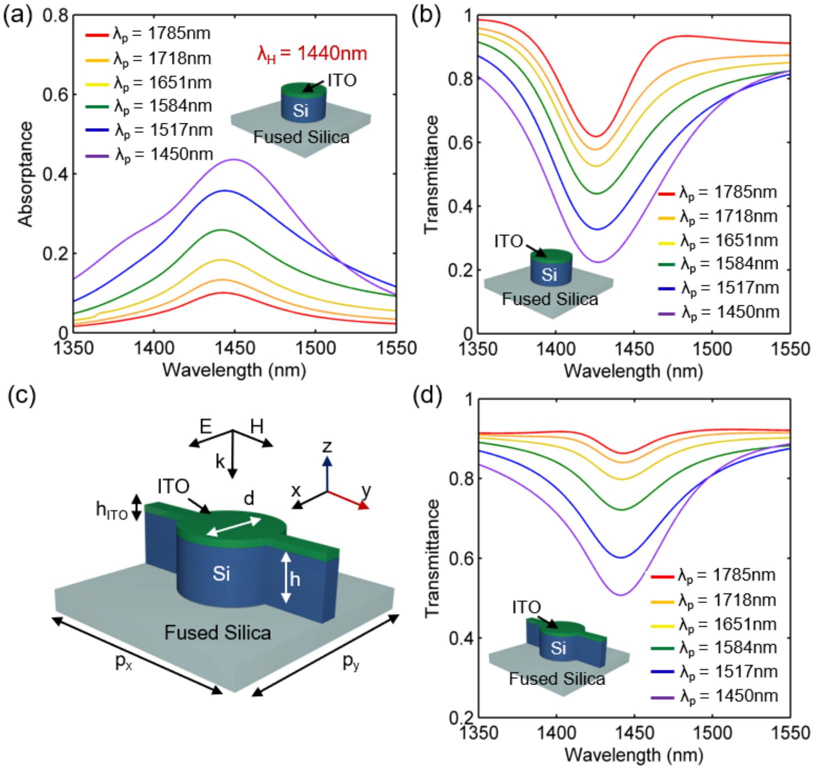

Figure 4.4: Metasurface final design and simulated modulation capabilities. (a) Simulated absorption for the metasurface in Figure 3.3(a) for several plasma wavelengths, increasing as the plasma wavelength approaches the Huygens wavelength. (b) Simulated transmittance for the same metasurface. (c) Unit cell schematic including dielectric bars for electrically connecting the ITO across resonators. The bar width is 80 nm. (d) Simulated transmittance spectra for the metasurface including bars.

mode is restored at λ_H. This relationship is illustrated in Figure 4.4(a), Similarly, the absorption is accompanied by a reduction in transmittance, and the model in Figure 4.4(b) predicts a modulation depth of 41% at λ_H=1450nm.

In order to modify the local carrier concentration of the ITO across multiple cylindrical resonators in an array, the ITO film must be continuous across the resonators. To accomplish this, we introduce this bars in our unit cell structure, as seen in Figure 4.4(c). Though the off-state transmittance is higher for the architecture with connected resonators, as seen in Figure 4.4(d), the modulation depth remains at 40% due to higher transmittance in the on-state. The higher value can be attributed to slightly better spectral overlap between the resonances.

4.4. Fabrication Procedure

To experimentally realize these devices, we constructed a silicon metasurface array integrated with a thin active ITO modulation layer with Au contacts and a solid electrolyte top gate. First, silicon on quartz wafers were fabricated at Oak Ridge National Laboratory via LPCVD. A liquid boron dopant was applied by spin coating at 4000rpm to ensure the ITO film was electrically connected throughout the array, and then baked on a hot plate at 200°C for 20 min. We annealed the same in a tube furnace at 1010°C for 45 min, then exposed it to O_2 gas at 850°C for 10 min to oxidize the top Si layer. Details regarding the oxidation rate are included in the appendix. Afterwards, the device was washed in a 10% HF;DI-H_2O solution to remove the oxide, leaving the silicon at the desired thickness (resonator height). We removed the backside Si by spin coating a protective photoresist layer on the front side and performing RIE. After removing the photoresist, the front-side Si thickness was measured using spectroscopic ellipsometry. If the height was above the resonator target height, we continued oxidizing the same to convert some of the Si to SiO_2, which was then again removed with HF.

Afterwards, we performed EBL and development (using A4 PMMA as the photosensitive film and 1:3 MIBK:IPA as the developing agent) to define the Si pattern. We deposited a 35nm Cr layer to function as an etch mask and lifted off the PMMA with Remover PG (Microchem). The silicon resonators were defined using RIE to etch through the remaining silicon, and the device was cleaned with an O_2 plasma treatment. The details of the RIE processes are also detailed in the appendix.

Next, we proceeded with a second round of lithography to define the ITO layer. We spin coated photoresist on the device (6000rpm) and baked in for 2 min at 95°C. After exposing the

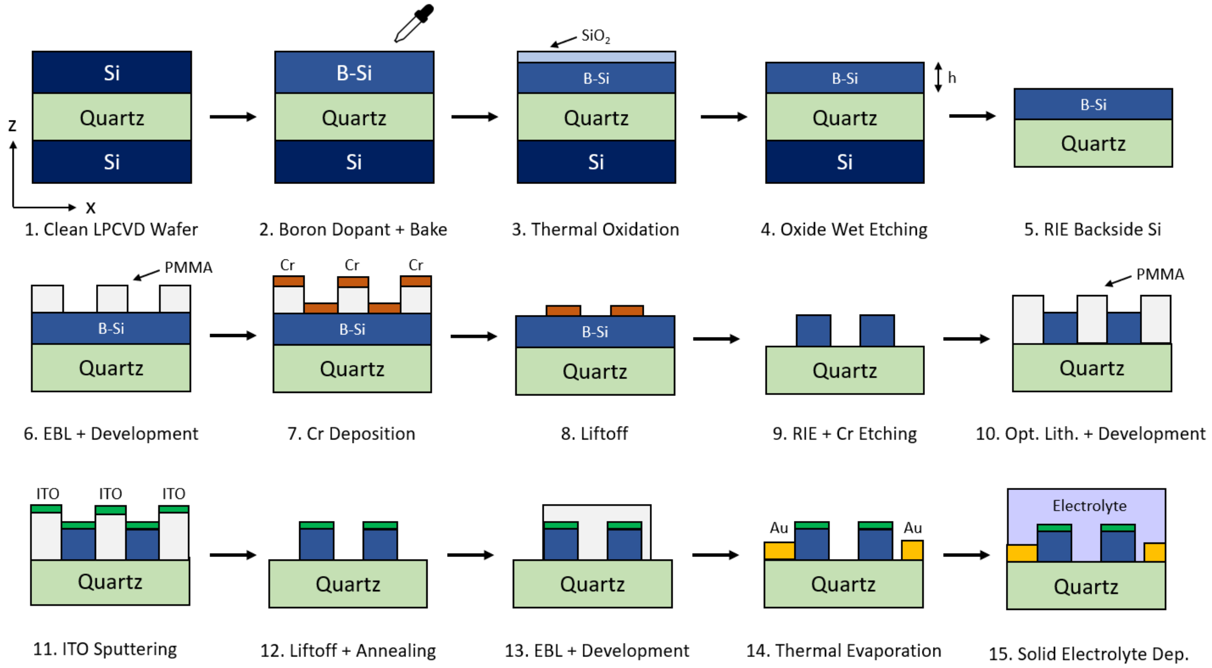

Figure 4.5: Metasurface transmission modulator fabrication procedure. After pre-processing, the devices are formed via thermal oxidation and three rounds of lithography. The role of oxidation is to ensure the thickness of the boron doped silicon layer is exactly the needed value for the Huygens mode. The first lithography process is responsible for defining the Si resonators, the second is used to create the ITO layer on top of the Si, and the third is needed to define the Au electrical contacts. Finally, the solid electrolyte solution is applied to connect the two electrodes. For more details on the finished device geometry, refer to Figure 3.6(c).

ITO layer design in the photoresist using optical lithography, developing it in MK-319 (Dow Inc.), and cleaning the sample again with O_2 plasma, we deposited a 10nm ITO layer using radio frequency (RF) sputtering. The sample was annealed in an oxygen environment to modify the ITO plasma frequency, which was verified using spectroscopic ellipsometry. Once the photoresist was removed via lift-off in acetone, we repeated this process to define the Au electrode layer, using thermal evaporation as the deposition mechanism.

Finally, a solid electrolyte solution was prepared to serve as the electrostatic gate. We used a bi-(trifluoromethylsylfonyl) amine lithium salt dissolved in poly (ethylene oxide) in order to index match the electrolyte and SiO_2 substrate to minimize reflection from the interface (Prasai et

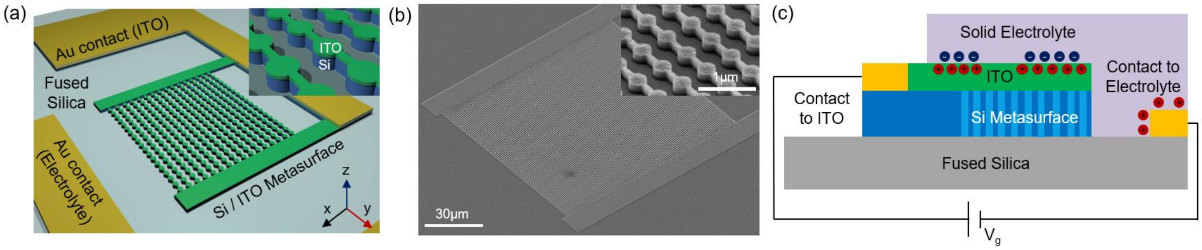

Figure 4.6: Metasurface modulator schematic. (a) 3D illustration of the fabricated device. The bias voltage is applied between the electrolyte contract and the ITO contact. (Inset) Zoomed image of the resonator structure within the array. (b) SEM image of the fabricated metasurface. (c) Schematic demonstration of the working principle of the device. The electric bilayer formed at the solid electrolyte / ITO interface is responsible for the local increase in ITO carrier density, changing its permittivity.

al., 2015). The details for preparing the solid electrolyte are provided in the appendix. After soldering wires onto the device electrodes, we applied the electrolyte to the device by spin coating at 800rpm and baking the same at 90°C for 5 min. A summary of this process is illustrated in Figure 4.5.

Figure 4.6 illustrates the final architecture of the device and the working principle for modulating the plasma frequency of ITO. One electrode is attached to the ITO, and the other is connected to the electrolyte. By applying a bias voltage between the solid electrolyte and the ITO, a charge bilayer forms at the interface between the two materials. This causes the local carrier density to increase in the charge accumulation region of the ITO, which modulates the local permittivity and therefore the spectral position of the ENZ mode. As we have discussed in section 4.3, moving the ENZ mode closer or further away (spectrally) from the Huygens wavelength results in the desired transmission tunability.

4.5. Measurement Setup

To measure the devices in this chapter, we constructed the custom IR optical characterization setup pictured in Figure 4.7. There are two main branches of the setup that are

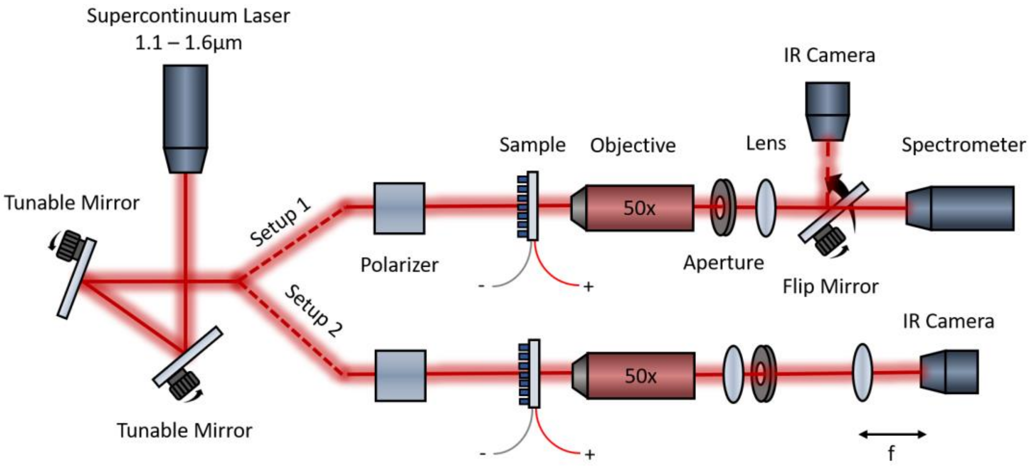

Figure 4.7: Optical measurement setup. The metasurfaces were measured using two architectures labeled Setup 1 and Setup 2. Setup 1 is for spectroscopy, and Setup 2 is for Fourier Imaging.

used for different experiments. The beam path labeled Setup 1 is designed for IR spectroscopy to measure the transmittance spectrum of the metasurfaces as a function of bias voltage. This branch consists of a polarizer, the sample positioned at normal incidence, an objective to magnify the image of the metasurface, an aperture to restrict the transmitted light to the specific array we are measuring, and a lens that directs the light either to an IR camera (for focusing and visualization of the array) or to the spectrometer cable. The spectroscopy experiments using this beam path will be discussed in Section 4.6. The beam path labeled Setup 2 is designed for Fourier Imaging to measure the transmitted angles in devices. This path is the same Setup 1 until after the objective; here, there is a lens to recapture the light from the objective and an aperture to restrict the light to the array being measured. After this, the IR camera can image the array. To get a Fourier image, we can insert a final lens before the IR camera at a distance f away from the camera, where f is the focal length of that lens. This will return the Fourier transform of the light passing through the lens. This way, we can easily switch between a real image and its Fourier image counterpart. This beam path will be discussed in Section 4.7 when considering additional functionalities and more complicated device architectures for control of the transmittance angle.

4.6. Transmission Results as a Function of Bias Voltage

Experimental transmittance data is plotted in Figure 4.8(a) for a device with a Huygens wavelength of 1470nm. The transmittance is modulated between 0.71 and 0.42 as we change the bias voltage between +10V and -10V. Note that a bias voltage of 0V does not result in maximum transmittance, as the Huygens mode is near the plasma wavelength of the unbiased ITO. Applying a negative bias moves the ITO plasma wavelength closer to the Huygens wavelength, decreasing transmittance, whereas applying a positive bias voltage moves the ITO plasma wavelength farther from the Huygens wavelength, increasing transmittance. The simulated transmittance spectra of the device are shown in Figure 4.8(b). The Huygens mode should exist at 1455nm with a transmittance modulation of 0.85 to 0.47. The difference in Huygens frequency between simulated and experimental data can be attributed to the fact that fabrication techniques limit our accuracy in defining the height of the silicon resonators. Additionally, the discrepancy in linewidth of the resonant mode can be attributed to slight inaccuracies in the modeling of ITO's permittivity, particularly the imaginary component.

Figure 4.8(c) is a series of images in an IR camera of our sample illuminated with 1470nm light fed through a monochrometer. As we change the bias voltage, the array appears darker, indicative of the lower transmittance. Figure 4.8(d) shows that the change in transmittance is gradual for intermediate voltages. To ensure modulation is not due to a change in the electrolyte, a control sample with no ITO was fabricated and demonstrated no change in transmittance. This is also verified by the fact that the bus bar lines remain transmissive in Figure 4.8(c) when biasing the sample. The average switching speed was found to be 88s and is dictated by the carrier mobility of the solid electrolyte. Since the carrier density of ITO is modulated via a field effect, the time

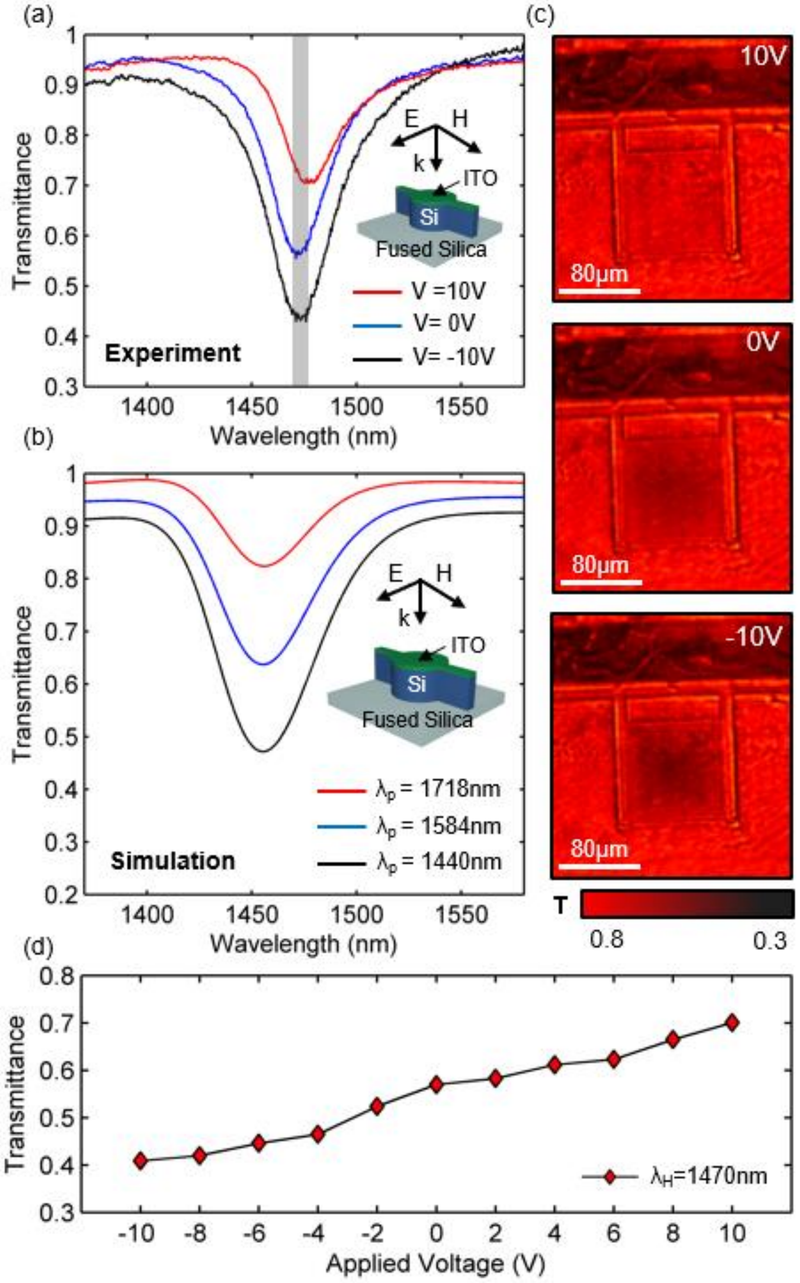

Figure 4.8: Transmittance experiment results. (a) Experimental transmittance spectrum of the fabricated device as three distinct applied bias voltages. The gray vertical bar indicates the wavelength at which the IR camera images in (c) were taken. (b) Simulated transmittance spectrum of the fabricated device at three distinct ITO plasma wavelengths. (c) IR camera images of the device at three bias voltages using monochromatic light at the working wavelength of the device. (d) Peak transmittance amplitude as a function of bias voltage, showing several intermediate voltage steps.

response of this device can be greatly improved using a more traditional metal/oxide gate.

4.7. Advanced Functionalities: Diffraction-Based Beam Steering (Proof of Concept)

By selectively patterning ITO over particular regions of the Si array, we can make select areas absorptive while the rest of the array remains highly transmissive. This freedom enables not only tunable filtering as seen in Figure 4.8, but also reversible diffraction-based beam steering. To demonstrate this effect, we designed and fabricated a device in which alternating strips of the ITO are electrically connected. The device schematic is outlined in Figure 4.9(a,b). Upon positive bias, the electrically connected regions become more transmissive, resulting in a single output beam.

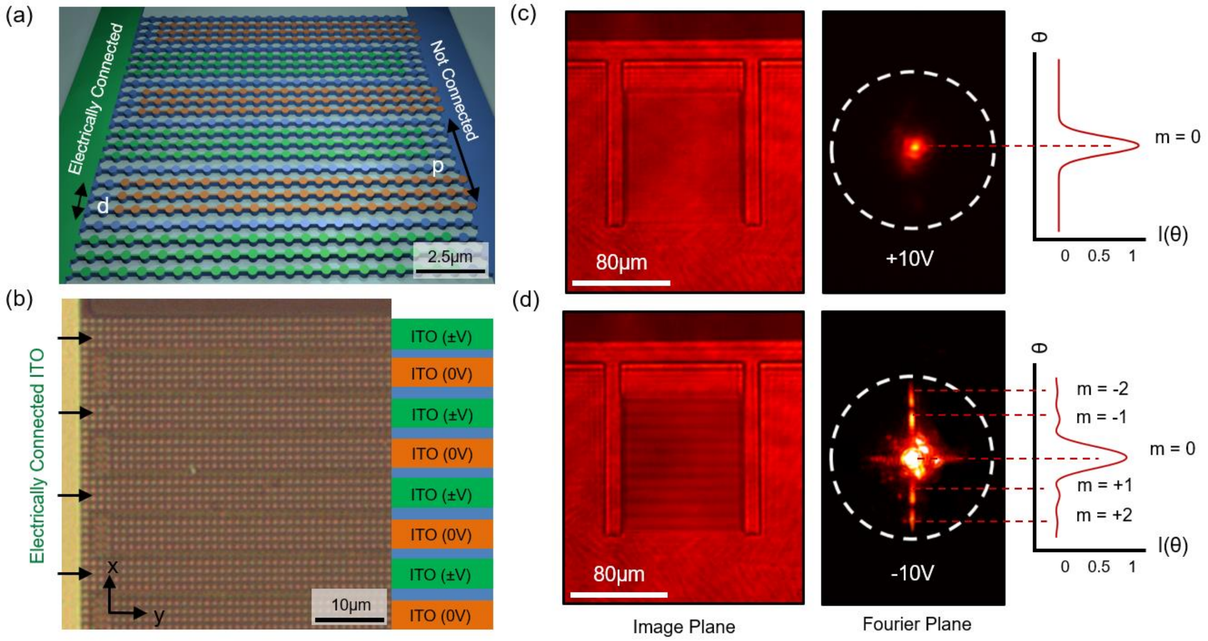

Figure 4.9: Metasurface beam steering proof-of-concept. (a) Schematic of the ITO grating structure over the array with dimensions d = 3.2μm and p = 8μm. Horizontal strips of ITO cover the silicon (blue) array, which alternate between those connected to an electrode (green) and those not electrically connected (orange). (b) Optical image of the completed device with patterned ITO in bars across the resonator array. (Right) Colored schematic illustrating which portions are electrically modulated. The colors match with those illustrated in (a). (c) (Left) IR camera image at 1470nm light of the device at a positive boas voltage. (Right) Fourier plane image of light transmitted through the metasurface. The white dashed circle represents the maximum angular field of view due to the numerical aperture of the objective used in the measurement (26°). (d) (Left) IR camera image at 1470nm light of the device at a negative bias voltage. (Right) Fourier plane image showing the diffraction pattern of the device. The plots on the right are simulated intensity plots of the diffraction pattern, labeled with the expected modes (m = ±1, 10.6°) (m = ±2, 21.4°).

Imaging the sample in the Fourier plane, as shown in Figure 4.9(c), confirms that one output beam is observed for this bias condition. The dotted circle represents the numerical aperture of the objective. The electrically connected strips will become absorbing upon negative bias, resulting in a diffraction pattern with beam maxima dictated by $psin(\theta) = m\lambda$, where p = 8μm, λ = 1470nm, and m is the diffracted order. Figure 4.9(d) demonstrates the experimental performance of the device under negative bias. We indeed observe the zero-, first-, and second-order diffracted modes in the Fourier plane. The simulated intensity plots on the right indicate the expected angular position of the diffracted modes for a grating with period p = 8μm, which coincide with the experimental images. This device serves as a proof of concept for reversibly modulating these ultrathin structures and could easily be expanded to more complicated designs.

4.8. Conclusions and Future Directions

In summary, we have presented a method to locally modify Mie resonances of dielectric resonators by using the ENZ point of thin conductive oxides. By choosing to utilize dielectric resonators, we avoid the absorption losses inherent to metallic devices and operate in transmission instead of reflection. In particular, our choice of materials eliminates parasitic losses in the device and forces all of the absorption within the ITO layer, enabling high absorption efficiencies. For these reasons, this approach offers a unique solution for compact spatial light modulators and dynamic optics in the near-infrared region.

Despite this progress, there is additional work that can be done to improve the device's performance. To realize a switching speed that is compatible with IR applications, the architecture can be improved by replacing the electrolyte with a more traditional metal and dielectric gate.

Additionally, by varying the ITO thickness, it may be possible to improve the absorption contrast between the on and off states.

CHAPTER 5

High-Efficiency Optical Limiters Based on Phase-Change Material-Integrated Huygens Metasurfaces

5.1. Introduction

The demand for power-limiting optics has accompanied the development of high-power lasers in order to mitigate damage to eyes as well as sensitive photodetectors, sensors, and cameras. For these applications, optical limiters are needed which transmit low intensity light (on-state) while blocking high intensity light (off-state). In the past twenty years, many approaches for optical limiting have been investigated. The most common designs have used two-photon absorption or absorption in nonlinear media as the limiting element (Ehrlich et al., 1997; G. S. He et al., 1995; Kannan et al., 2004; Karimzadeh, Aleali, & Mansour, 2011; Westlund et al., 2008). However, many of the examined materials such as carbon black (Jin, M. H., Durstock, M., Dai, 2006), cadmium sulphates (Dhanuskodi, Girisun, Smijesh, & Philip, 2010), graphene oxides (Liaros, Koudoumas, & Couris, 2014), and silica with metal nanoparticles (Du, Chen, Kao, Wu, & Hong, 2015) have been primarily studied as dilute suspensions in liquid and suffer from turndown ratios below 10. Alternatively, some limiter designs with damage thresholds near their limiting threshold provide larger turndown ratios at the expense of single-use protection. While polymeric films (Ali, 2019) and dye-based approaches (H.-K. Liu, 2003) possess high electro-optic coefficients and lower costs, they also actuate slowly and exhibit a tradeoff between the on-state transmission and turndown ratio.

The most important set of features for a limiter is a high on-state transmission, large turndown ratio, high damage threshold, and a fast response time. In order to passively switch from the on-state to the off-state, the limiter should incorporate an intensity, field, or temperature-dependent material to maximize the turndown ratio. Here, we demonstrate a transmissive and all-dielectric optical limiter with an excellent turndown ratio based on Vanadium Dioxide (VO_2) as the active material. Vanadium dioxide possesses a large contrast in optical constants upon undergoing a semiconductor to metal phase transition. This transition occurs within 60fs when triggered optically, making the device suitable for limiting both continuous wave as well as ultrafast pulsed lasers (Braun et al., 2018). Additionally, the phase transition threshold is tunable by applying stress or doping; therefore, the limiting intensity can be adjusted throughout the near-infrared depending on the application.

The use of nanoscale structuring in optics creates new possibilities and architectures for limiters. For example, Bragg mirrors with a semiconductor defect layer have been investigated for limiters (Vella et al., 2016) but this approach requires a reflection band around the limiting wavelength and is restricted to narrow-band operation. One method to circumvent this issue is to instead use highly efficient metasurfaces to enhance the properties of existing nonlinear media. Metasurfaces can increase the light-matter interaction in nearby nonlinear or tunable media by using resonant fields to alter their optical properties. However, optical limiter designs using metasurfaces are scarce and to date have only used reflection-based architectures. All-dielectric metasurfaces are more suitable for transmissive optics due to the low optical losses compared to plasmonic counterparts, offering higher efficiencies in the on-state.

In this chapter, we present an optical limiter by integrating VO_2 with an all-dielectric metasurface. The resonators are designed to support electric and magnetic dipole Mie-type resonances at the same energy, resulting in a Huygens mode with high transmittance in the on-state. An epsilon-near-zero (ENZ) mode of the VO_2 is introduced to damp the transmission. The limiting behavior of the device triggers when the incident intensity grows strong enough to change the phase of VO_2 from semiconductor to metallic, further increasing the absorption and decreasing transmission. The simulated transmission contrast between the on-state and off-state is 25.2dB with an on-state transmission of -4.8dB. We experimentally realize this design in the near-infrared and further explore the working wavelength range of the limiter by scaling the geometry of the resonator structure. Additionally, we investigate the expected performance in both steady-state and pulsed laser environments via thermal analysis. Our transmission-based approach towards optical limiting provides a superior combination of efficient on-state performance and large turndown ratio compared to its predecessors. Additionally, the unique combination of a fast response time, high damage threshold, large transmittance off-resonance, and conveniently scalable performance from 1-2um makes our design not only a strong candidate for current limiting demands, but also a suitable platform for future near-infrared optics.

5.2. Fundamental Properties of Vanadium Dioxide

Vanadium dioxide (VO_2) is a phase change material, a substance which can transform between different crystal structures in response to external stimuli such as laser fields, stress, or extreme temperatures. Due to the change in crystal structure, phase change materials such as VO_2 experience large changes in their electronic band structures and therefore optical and/or electrical properties. In particular, VO_2 has been the subject of much optics research due to its large contrast in optical properties in the near-IR, relatively low transition temperature (340 kelvin (K)), and fast transition speeds (Lazarovits, Kim, Haule, & Kotliar, 2010; Zhang et al., 2015). At low temperatures (<340K), VO_2 possesses a monoclinic crystal structure and acts as a standard

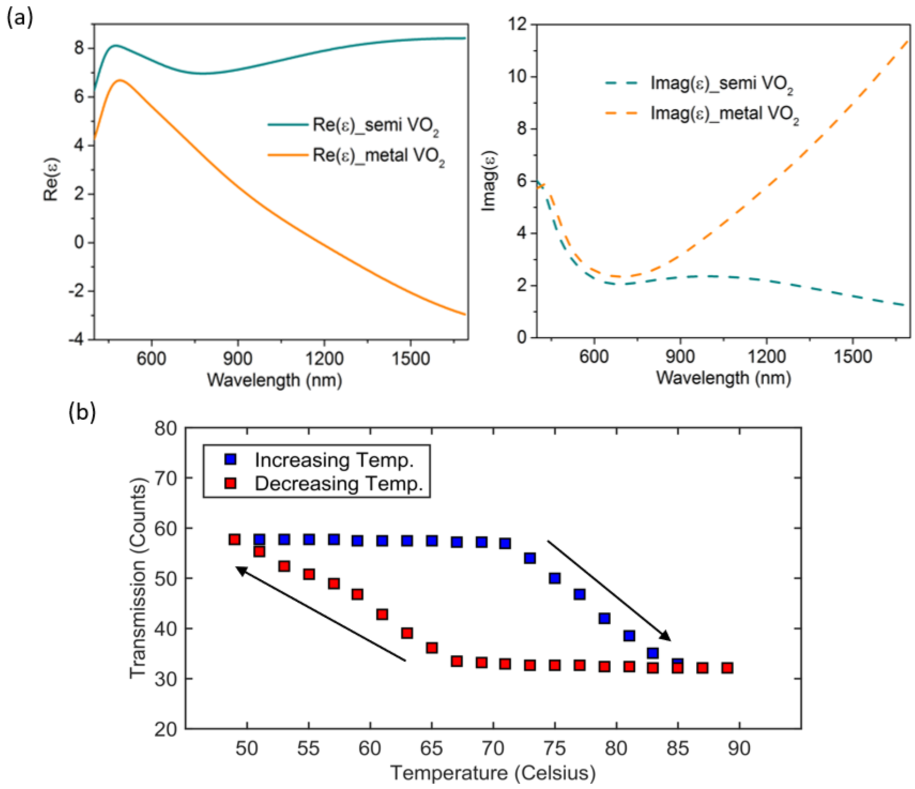

Figure 5.1: Fundamental characteristics of VO_2 and their consequences on optical properties. (a) Real (left) and imaginary (right) permittivities as a function of wavelength for VO_2 in both the semiconducting (low-temperature) and metallic (high-temperature state). (b) Transmission as a function of temperature for a 30nm VO_2 film on silicon at 1300nm.

dielectric with high resistivity. However, at high temperatures (>340K), the crystal structure transforms to rutile and the material becomes largely metallic with decreased resistivity. This is illustrated in Figure 5.1(a) where the real component of the permittivity at 1200nm and above is high ($\varepsilon_r > 7$) in the semiconductor state but below zero in the metallic state. Similarly, the imaginary component of the permittivity is massively increased in the metallic state. While triggering the phase transition is possible via strain, large electric field, and optically, the most common and accessible method is via thermal heating. The results of heating on the transmission of a VO_2 film are shown in Figure 5.1(b), confirming the larger losses in the metallic state. This dramatic contrast opens the door for many nanophotonic elements using VO_2 such as communications devices (Miller, Haglund, & Weiss, 2018; Miller, Hallman, Haglund, & Weiss, 2017; H. Wang, Yi, & Li, 2005), gas sensors (Liang, Li, Liu, & Hu, 2016; Strelcov, Lilach, & Kolmakov, 2009), and field-effect transistors (Kim et al., 2004; Stefanovich, Pergament, & Stefanovich, 2000).

The phase transition of VO_2 is both electronic and structural (Haverkort et al., 2005). When it comes to the phase transition time, different speeds are reported based on the modulation method. Nanosecond response times have been demonstrated in a silicon-based VO_2 modulator design using thermal heating (Markov et al., 2015), and ultrafast studies of optically inducing the phase transition are theorized to occur as quickly as 60fs. The discrepancy here is due to the discussion of whether the Peierls or Mott-Hubbard models (structural transition or electronic transition mechanism, respectively) are dominant at different timescales. Previous studies have shown that the structural phase transition occurs within picoseconds while the electronic transition requires only tens of femtoseconds (Wegkamp et al., 2014), providing opportunities to study phase transitions of VO_2 that are purely electronic (staying in the monoclinic lattice structure) and therefore faster using femtosecond laser pulses.

5.3. Enhancing Absorption by Combining Vanadium Dioxide and Huygens Modes

To create an all-dielectric metasurface-based optical limiter, a thin layer of Vanadium Dioxide (VO_2) is added to the Huygens mode resonator geometry, as seen in Figure 5.2(b). At room temperature, VO_2 is a lossy semiconductor with large real permittivity at λ_H, pictured in Figure 5.2(a). Due to the losses at this wavelength, the transmittance of the VO_2-integrated Huygens metasurface is no longer unity but remains reasonably large for the on-state of an optical limiter. When VO_2 is heated above ~67° C it undergoes a phase change from semiconducting to metallic, changing the permittivity as seen in Figure 5.2(a).

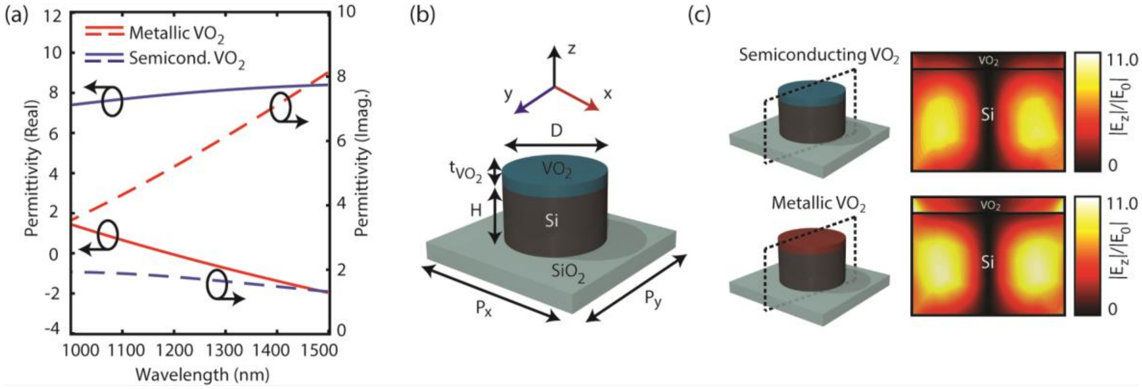

Figure 5.2: Fundamental design of Huygens mode / VO2 – integrated metasurface design. (a) Real and imaginary permittivity of VO_2 in the semiconducting and metallic state. (b) Unit cell design of the VO_2-integrated metasurface. (c) Z-oriented cross-sections displaying the electric field distribution for the VO_2-integrated resonator design in the metallic and semiconductor state.

The main advantage of this temperature-dependent phase change in our limiter design is twofold. First, the metallic phase of VO_2 has a much higher imaginary permittivity than its semiconducting state. This fulfills the basic requirement of an absorptive optical limiter – the device will be self-adjusted from the on-state to the off-state when VO_2 is heated up from incident radiation above the phase transition threshold via absorption. Second, the transmittance will be further suppressed in the off-state since the real permittivity of metallic VO_2 is engineered to cross zero at the wavelength of the electric and magnetic dipole Mie modes of the underlying silicon resonator. The consequence of this epsilon-near-zero (ENZ) mode in the VO_2 is seen by considering the electromagnetic boundary condition for the normal displacement field (Silveirinha & Engheta, 2006). Similarly, as with the metasurface geometry in Chapter 4, when the permittivity of VO_2 approaches zero the electric field inside is enhanced to compensate and satisfy the boundary condition. This is illustrated in Figure 5.2(c), where cross-sections of the VO_2-integrated metasurface unit cell design are pictured for semiconducting and metallic VO_2. In the case of

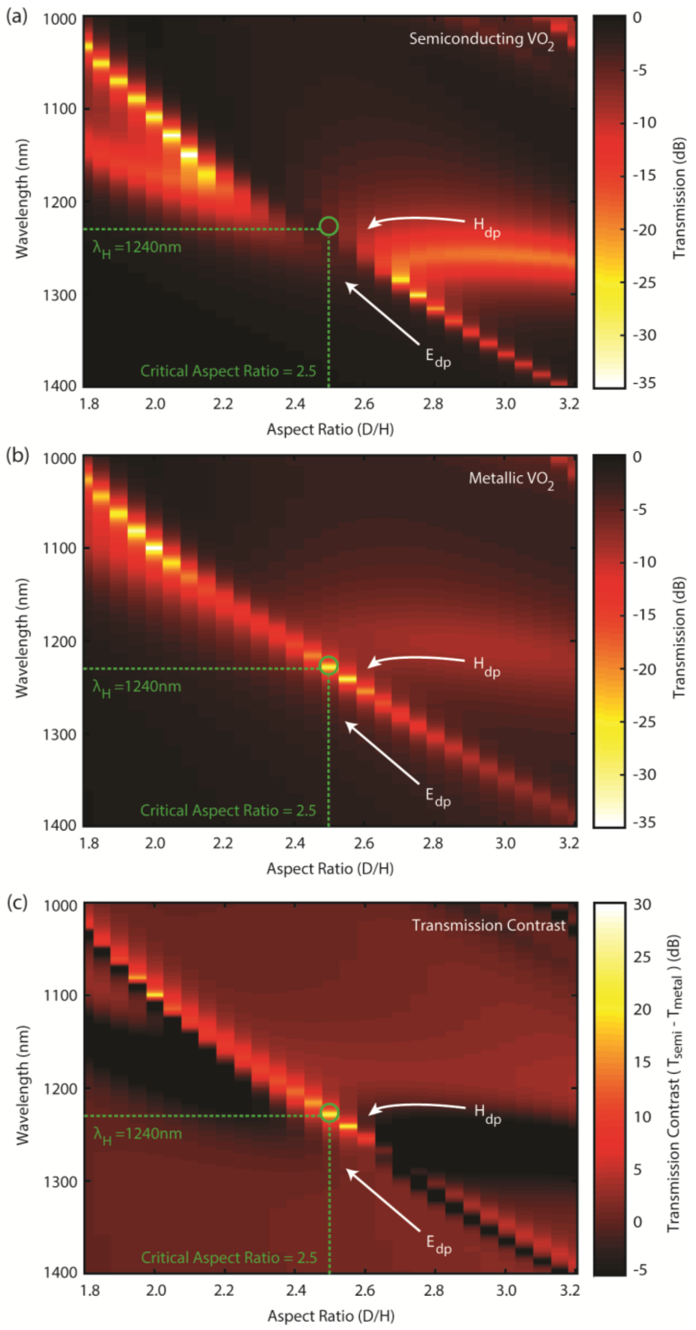

Figure 5.3: Engineering overlapped Mie resonances and optimizing optical contrast between the on-state and off-state. (a,b) Transmittance as a function of wavelength and aspect ratio (diameter / height) for VO_2-integrated Huygens metasurfaces when in the (a) on-state and (b) off-state. (c) Transmission contrast as a function of wavelength and aspect ratio. The optimized metasurface geometry ($t_{Si} = 190$nm, AR = 2.5, $P_x = P_y = 660$nm, $t_{VO2} = 35$nm) exhibits maximum optical contrast and minimum off-state transmittance.

metallic VO_2, the electric field inside the VO_2 layer in enhanced up to a factor of 11 compared to the field inside the silicon resonator. This field enhancement will naturally result in increased absorption, given by $A = \int \varepsilon_i |E|^2 dV$. Therefore, the presence of the ENZ mode in VO_2 will increase the cutoff efficiency in the off-state.

In order to achieve a high on-state transmission and therefore a large contrast between the on-state and off-state, the two Mie dipole-type resonances in the Si resonator must be perfectly spectrally overlapped. To achieve this, the aspect ratio corresponding to structures with the same electric and magnetic dipole mode energies has to be engineered at the wavelength of the ENZ mode of metallic VO_2 (1.23μm). This behavior is illustrated in Figure 5.3(a,b), where the transmittance of the optical limiting metasurfaces are simulated as a function of wavelength and aspect ratio using CST Microwave Studio. For large aspect ratios (AR > 2.6), the magnetic and electric dipole Mie resonances are spectrally separated. As the aspect ratio approaches AR=2.5, the two resonances merge and destructively interfere, resulting in high transmittance (-4.8dB) as highlighted in Figure 5.3(a). At the same aspect ratio for metallic VO_2 (Figure 4.3(b)), the ENZ mode and enhanced absorption causes the transmittance to drop to -30.0dB at 1.24μm. The final resonator geometry was selected by optimizing the transmittance contrast between the on-state with semiconducting VO_2 and the off-state with metallic VO_2, while also ensuring that the off-state was as close to zero as possible. This design is displayed in Figure 5.3(c), where a contrast of 25.2dB is achieved.

5.4. Fabrication Procedure

To validate this approach for achieving a Huygens metasurface-based optical limiter, we fabricated and characterized devices with geometries outlined in Figure 5.3. We began with wafers of 190nm Si on SiO_2 with 35nm VO_2 films grown via atomic layer deposition (ALD). To define

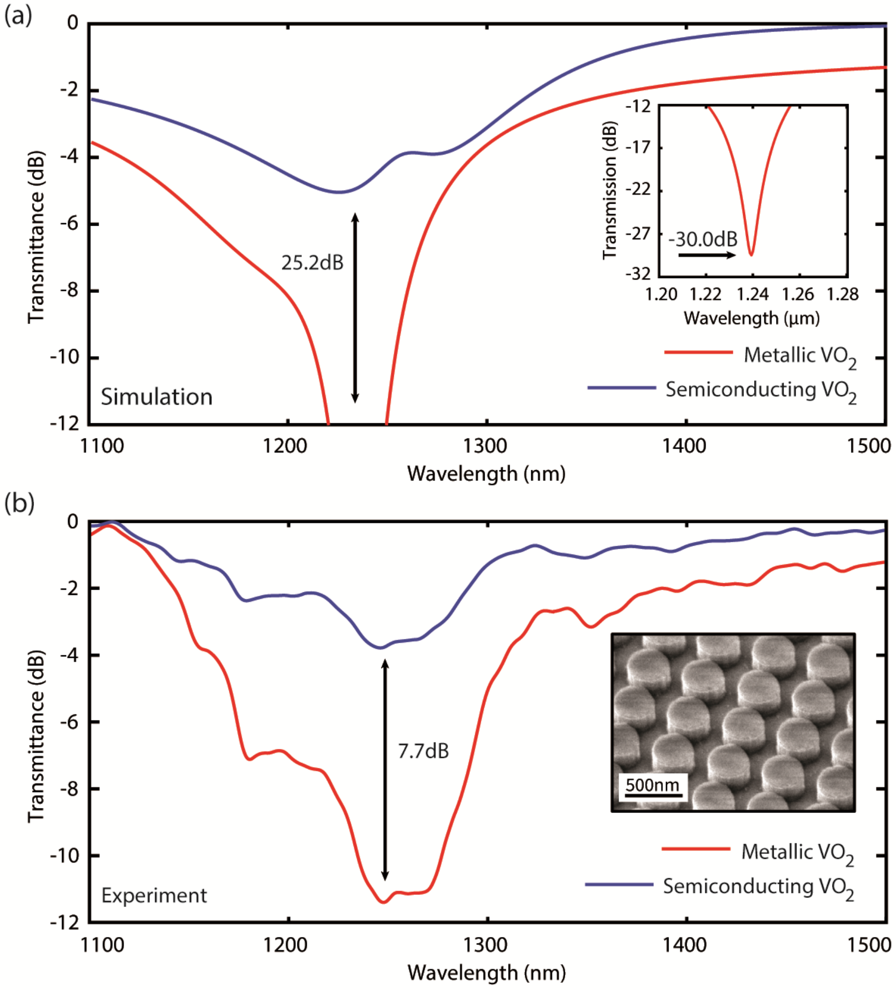

Figure 5.4: Experimental demonstration of VO_2-integrated metasurface-based optical limiter. (a,b) Simulated (a) and experimental (b) transmittance of the limiter with optimal resonator geometry in the on and off-states. (b, Inset) SEM image of the fabricated device.

the resonator structure, electron beam lithography was performed with PMMA as the photoresist and 1:3 MIBK: IPA as the developing agent. Afterwards, a 55nm Al_2O_3 etch mask was formed using electron beam deposition, and the same was placed in hot PG remover until the undeveloped PMMA had successfully lifted off the sample. The samples were then treated with a 1:8 30% H_2O_2:H_2O solution for 15 minutes at 85°C to selectively etch the VO_2 that was not underneath the hard mask. The samples were then formed using reactive ion etching (RIE) to define the silicon cylinders. Finally, a top coat of PMMA was applied and baked at 180°C for 3 minutes to protect the metasurface layer and serve as an index matching material to the SiO_2 substrate to prevented unwanted reflection during measurement. A SEM image of the completed devices can be found in the inset of Figure 5.4(b).

5.5. Measurement and Optical Limiter Characterization

The samples were measured in a custom spectroscopy setup similar to Setup 1 in Figure 3.7; the only major difference here is the addition of a heating module attached to the sample stage that allowed for resistive heating of the sample as a function of bias voltage. This heating element served as the trigger for forcing the VO_2 between semiconducting (25°) and metallic (85°) states. The simulated on-state and off-state transmittance is illustrated in Figure 5.4(a), and the experimental data is plotted in Figure 5.4(b) for a device with an operating wavelength of λ_H=1.24um. In the on-state, the transmittance matches with the simulated performance (-4.8dB at λ_H). In the off-state, the minimum transmittance achieved is –11.7dB, resulting in a 7.7dB contrast. While the off-state transmittance does not achieve the simulated value, the absolute transmission amplitude in the off-state remains under 5%.

The discrepancy between simulated and experimental results can stem from many factors. First, the metasurface design heavily relies on the perfect overlap between the electric and magnetic dipole Mie modes in the silicon resonator. The cylinder radius has a tolerance of 5nm; the z-oriented fields necessary to enhance the absorption in the VO_2 will not spectrally overlap with the ENZ region of the metallic-state VO_2 outside this range. Even small fabrication errors can result in this type of spectral misalignment. Second, the permittivity function of VO_2 is sensitive to stress and its switching behavior is highly dependent on its environment. At 35nm thick, the VO_2 is not a completely continuous film, and it is possible that only certain regions of VO_2 are properly switching. If so, the material near the outer radius of the resonators is most likely to behave properly since the z-oriented fields from the silicon resonator are strongest in this region (As depicted in Figure 5.2(c)). Therefore, the absorption is being enhanced due to the ENZ mode in VO_2 more in these areas than in the middle of the circular film above each resonator. If only part of the resonator is successfully switching, then the off-state transmission will suffer. Finally, since the VO_2 film is not continuous, its average thickness varies in-plane and will affect the quality of the ENZ mode and therefore the resonant absorption.

5.6. Design Scalability across the Near-Infrared

One advantage of this metasurface-based design is the ability to adjust the working wavelength by tuning the size of the resonators. The ENZ point of metallic VO_2 is approximately 1230nm with the carrier concentration used in our sample. One method to adjust the performance would be to chemically dope the VO_2 to shift its ENZ wavelength. While possible, this would require different growths of VO_2 films with varying doping levels for each target wavelength. An

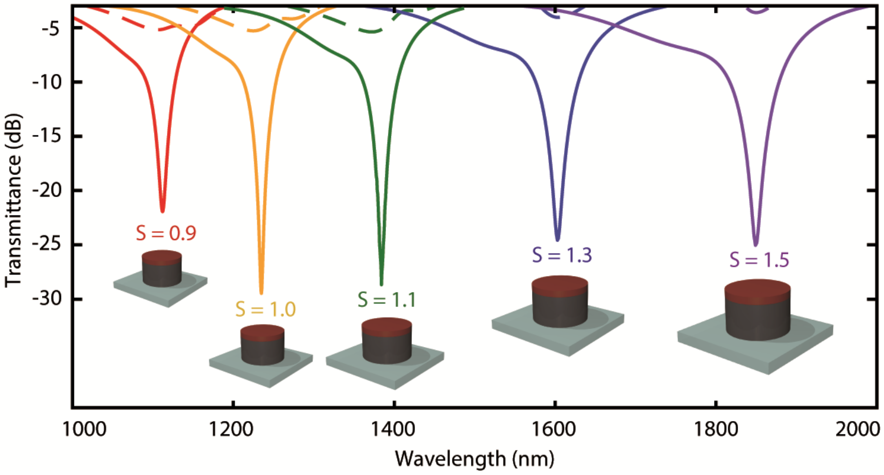

Figure 5.5: Demonstration of resonator scalability. Simulated transmission spectra in the on (dashed) and off-states (solid) for several optimized metasurface designs with scaled dimensions (S=0.9, 1.1, 1.3, and 1.5), where the diameter, period, and resonator height are all multiplied by S.

easier solution is to vary the geometry of the underlying silicon resonator. Despite the fact that the ENZ point is fixed, it is possible to achieve high transmittance contrast between the on and off states of the device at longer wavelengths where metallic VO_2 has larger absorption losses. To explore how this type of metasurface operates at other wavelengths, we simulate devices with unit cell dimensions uniformly scaled by a factor S, with the exception of the VO_2 thickness. For S=0.9, 1.1, 1.3, and 1.5, the resonant wavelengths of the Huygens modes are 1060nm, 1400nm, 1610nm, and 1870nm, as pictured in Figure 5.5. Over 18dB transmittance contrast is observed for all four metasurfaces with scaled working wavelengths, compared to 25.2dB contrast for a device with S=1. The decrease in contrast for the scaled designs illustrates the importance of the spectral difference between the ENZ point of VO_2 and the Huygens mode: the spectral overlap governs the magnitude of field concentration in the VO_2 film, controlling the cutoff efficiency.

5.7. Thermal Analyses: Steady-State and Temporal Limiting Behavior

While this design displays promising cutoff efficiency and contrast, it is also important to investigate the thermal dynamics of the metasurface to estimate the incident intensity threshold. To characterize the performance of the limiter design, a CST thermal solver is used to calculate the mean temperature of the VO_2 film using the material properties listed in Table 5.1. Assuming silicon and the SiO_2 substrate are both lossless, the injected power $Q = AI_{in}\alpha$ is entirely absorbed within the VO_2, where A is the cross-sectional area of the unit cell, I_{in} is the incident intensity, and α is the absorptance of the device. The absorptance at the semiconducting and metallic VO_2 states at λ=1240nm is α_{Semi}=0.6 and α_{Metal}=0.97. These parameters govern the temperature of the film as a function of input intensity, as illustrated in Figure 5.6(a,c). The VO_2 film in the model is treated as a heat source that dissipates energy to its environment with an ambient air convection of

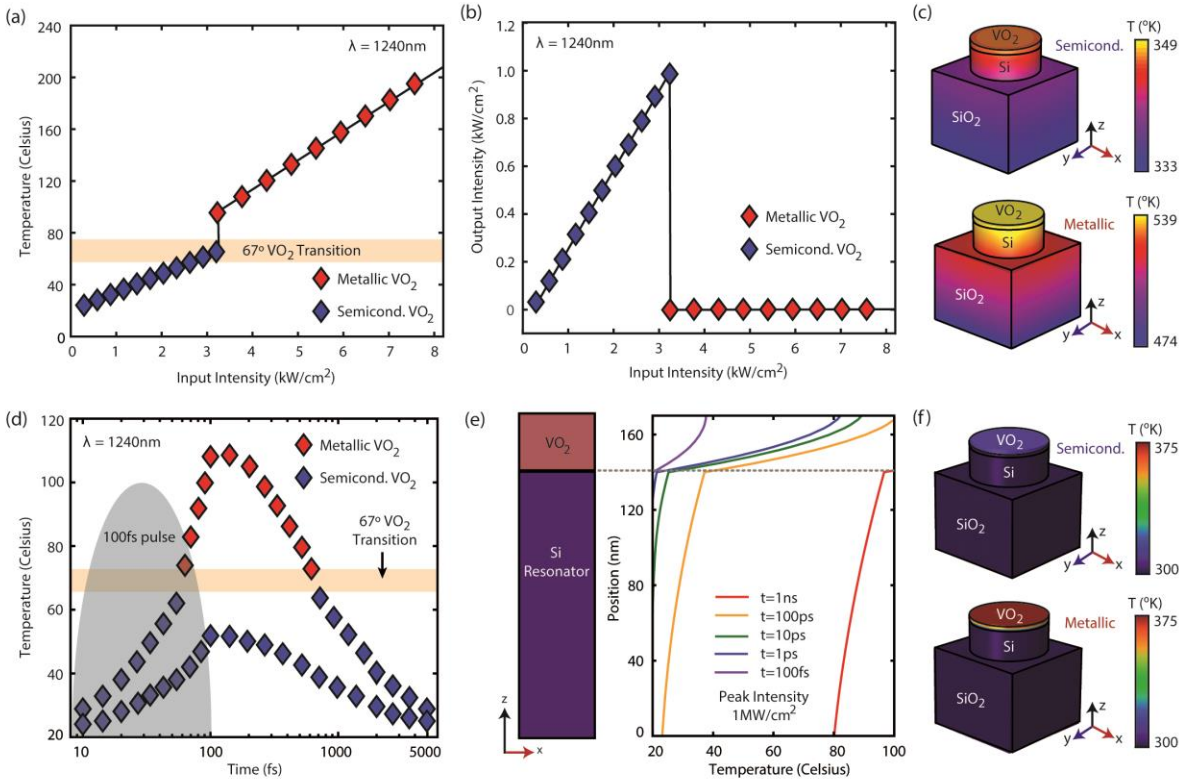

Figure 5.6: Thermal performance of VO_2 and its effect on optical limiting functionality. (a) Simulated mean temperature of the VO_2 film as a function of incident intensity in a steady-state environment. (b) Nonlinear relationship between the output intensity and input intensity, demonstrating optical limiting behavior. (c) Thermal distribution of the metasurface unit cell when operating in the on-state (Input Intensity = 3.1kW/cm^2) and off-state (Input Intensity = 9.0kW/cm^2). (d) Temporal thermal characteristics of the optical limiter for two 100fs pulses of peak intensities 2MW/cm^2 and 5MW/cm^2. The greater the incident intensity, the greater the recovery time due to heat dissipation. (e) Heat confinement as a function of pulse duration. The position on the y-axis corresponds to the z-axis of the resonator structure, as seen on the left. (f) Thermal distribution of the metasurface unit cell when operating in the on-state and off-state with a pulsed excitation.

Table 5.1: Thermal properties of materials in the Huygens metasurface-based optical limiter design.

Material	Density (g/cm^3)	Thermal Cond. $W/K \cdot m$	Heat Cap. ($kJ/K \cdot kg$)
Si	2.328	1.5	0.71
SiO_2	2.4	1.4	0.75
VO_2 (25℃)	4.57	3.5	0.656
VO_2 (85℃)	4.64	6	0.78

50W/m^{2}K. Adiabatic boundary conditions are used in the in-plane directions to mimic a periodic boundary. In the semiconductor phase, the mean temperature of VO_2 is heated to 67°C at an incident intensity of 3.2kW/cm^2 (Figure 5.6(a)). Once the phase transition is triggered, the temperature will rise at a greater rate alongside the incident intensity due to the increased absorption in the metallic state. We observe a simulated decrease of four orders of magnitude in output intensity I_{out} for intensities greater than 3.2kW/cm^2, as illustrated in Figure 5.6(b). For a 20µmx20µm device array, the required beam power is 12.8mW, which is consistent with the fluence needed for the ultrafast VO_2 phase transition triggered by a femtosecond laser (Braun et al., 2018). This method requires less power to trigger the phase transition of VO_2 than thermal heating since the dielectric environment surrounding the film experiences nearly zero absorption losses. Therefore, all the absorbed incident power is funneled into the VO_2 and more efficiently governs the material state than plasmonic metamaterials, in which metallic elements absorb a large amount of incident energy. Additionally, metallic nanostructures possess a higher conductivity than dielectrics used in our design, and exposure to air can affect the thermal properties due to convection.

Many applications of optical limiters, such as signal jamming protection systems in aircraft, require adequately fast response times with pulsed sources. One benefit of using VO_2 in metasurface-based optics is its ultrafast switching speed. Previous studies of VO_2 have demonstrated that the semiconductor to metallic phase transition occurs within 60fs, making this design suitable for an ultrafast laser environment (Braun et al., 2018). For example, a 100fs pulse can provide enough energy to trigger the VO_2 phase transition and cut off transmission, as seen in Figure 5.6(d). Since the energy is being absorbed in a much shorter time than in the steady-state solutions provided earlier, the intensity needed to observe this behavior is significantly higher than in Figure 5.6(a-c). For example, a pulse of peak intensity 2MW/cm^2 will only raise the temperature of VO_2 to 50°C and will not trigger the limiting behavior, while a pulse of 5MW/cm^2 will force

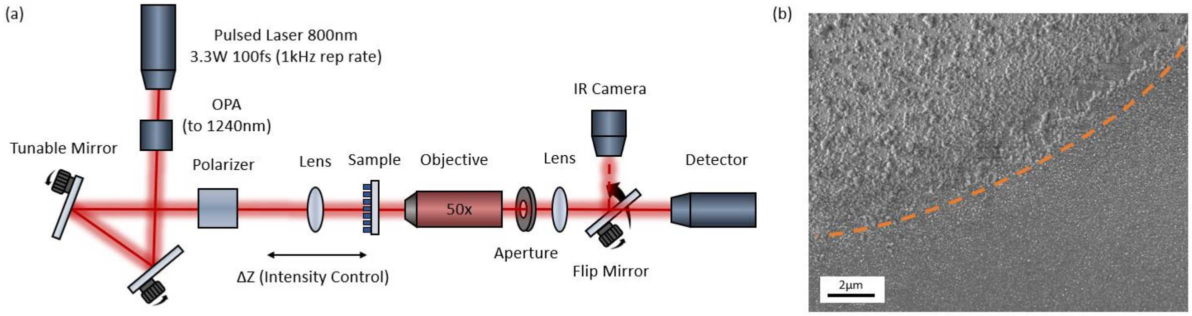

Figure 5.7: Observation of VO_2 film optical intensity damage threshold in a pulsed laser environment. (a) Optical setup used to observe the damage threshold of the VO_2 film. The power output after the laser passes through the OPA is 300mW, and the focal length of the lens used to modify the intensity on the sample is 150mm. (b) SEM image of a 35nm VO_2 film after illumination via the setup in (a) with an incident intensity of ~900MW/cm^2. For a pulse duration of 100fs, this intensity corresponds to an energy density of 90mJ/cm^2. The orange dashed line signals the edge of the beam spot and separates the damaged area (top) from the undamaged area (bottom).

the VO_2 above 100°C within 100fs. As expected, the relaxation time for the device depends on the maximum temperature reached during the duration of the pulse. In the case of a 5MW/cm^2 100fs pulse, the system cools to the semiconducting state within ~1ps, as seen in Figure 5.6(d). Therefore, the rate of ultrafast pulses such a system can effectively react to is limited by the thermal relaxation time and the intensity of the pulses.

Another factor to consider is the damage threshold, above which the VO_2 will be irreversibly affected and no longer undergo phase transitions. This value was reached experimentally by exposing a VO_2 film to a 100fs pulsed laser at an intensity of 900MW/cm^2 (Figure 5.7). This corresponds to an energy density of 90mJ/cm^2 and agrees with previous studies of the damage threshold of VO_2 films (X. R. Chen, Hu, Han, & Xu, 2008).

Thus far, our thermo-optic analyses of the metasurface design have been from opposite extreme timescales. While it is expected that transient and steady-state solutions differ, we can understand more about the limitations and nature of the resonator-VO_2 system by observing its evolution from a pulsed excitation to continuous exposure. For example, in the case of excitation via an ultrafast (100fs pulse), nearly all of the thermal energy is contained within the VO_2 layer, as seen in Figure 5.6(f). This is a consequence of the thermal conductivity of Si and short timescales compared to the steady-state solutions (Figure 5.6(c)). We can understand how the pulse duration affects the maximum temperature and thermal distribution within the metasurface structure by plotting the temperature as a function of position after exposure to pulses of various timescales. While increasing the pulse duration increases the average temperature of the device, particularly the VO_2 layer, it also allows more energy to bleed into the underlying Si resonator, as shown in Figure 5.6(e). As the length of exposure is increased beyond picosecond timescales, we begin to see the thermal behavior of the system converge to the steady-state profile in Figure 5.6(c). This provides a reassuring continuity between our two analyses of thermal dynamics at short and long timescales. Additionally, it provides a more complete picture of the limits of this metasurface limiter design in different application spaces in terms of the allowed intensities and damage thresholds of the device.

5.8. Conclusions and Future Directions

In summary, we have created a metasurface-based optical limiter with a unique combination of advantages over its predecessors. By harnessing the light-matter interaction between Huygens modes in dielectric resonators and VO_2, our design exhibits an efficient on-state transmission of -4.8dB while providing a contrast of 25.2dB on resonance. Additionally, this architecture is a flexible platform for previse multiwavelength limiting due to the high transmittance off-resonance and easily scalable resonant energy within the n-IR. Furthermore, our choice of VO_2 as the active component allows for protection in ultrafast environments due to the speed of the insulator-metal transition. With these benefits, our metasurface-based approach for an infrared optical limiter serves as a strong alternative for free-space elements or future ultrathin applications.

However, there is one major limitation with our limiter design: its absorptive nature. Optical limiters typically come in two forms – absorptive, in which the blocked light is lost to absorption, and reflective, in which the blocked light is reflected away. As incident light gets stronger and interacts with an absorbing limiter, eventually the light will generate enough heat to damage or destroy the device, whereas no such restriction applied to a system that reflects away incident energy. In the future, it would be interesting to consider a similar architecture that modulates into a negative permittivity region of a tunable material instead of modulating to the ENZ point of VO_2 in the metallic state to enhance absorption. Extra work is needed to produce such a material that guarantees light would be lost to reflection rather an absorption (in other words, a large modulation of the real permittivity compared to the imaginary permittivity), but if possible, would be a convenient route for compensating for this type of limiter's weaknesses. Additionally, since the system is highly transmissive off-resonance, this architecture presents an opportunity for customizable limiting profiles by stacking metasurface layers. For example, if one wanted to limit at specifically 1200nm, 1400nm, and 1600nm, but nowhere else, one could envision an architecture that consists of three limiter layers build with the geometries of S=1.0, S=1.1, and S=1.2 in Figure 5.5.

CHAPTER 6

Dynamic Phase Modulation via Multi-Quantum Well-Integrated Dielectric Metasurfaces

6.1. Introduction

In previous chapters, we have investigated how to take advantage of unique combinations of electromagnetic modes to both create novel and actively tunable amplitude profiles in the infrared. However, amplitude is not the only parameter of light that carries information and can be harnessed for optical technologies; the phase of light is a powerful tool for modern optics as well. Phase information is critical for many applications and is used in various microscopy techniques, quantum computing, holography, diffraction optics, signal processing, and polarization manipulation. Just as noted in previous chapters with devices that can provide custom amplitude profiles, altering the phase of light in a compact platform is also achievable by using metasurfaces. Many meta-optics that rely on resonances take advantage of the fact that a large change in phase (π) is accumulated as one passes through a resonance in the frequency domain. This property is a fundamental consequence of damped harmonic motion as described by Newton's laws and the Lorentz oscillator model. Since the resonant frequency of meta-atoms can be adjusted by their size or structure, the phase of the reflected or transmitted light can be modified in the same manner.

This concept has spurred the creation of many meta-optics that can steer or focus light. For example, by constructing resonator structures that have regularly scaled sizes as a function of position, it is possible to create a phase gradient across the metasurface which effectively deflects an incident light beam in a desired direction (Xu et al., 2018; Yu et al., 2011). By controlling the phase in a radial direction, it is possible to steer light using metasurfaces into a focal spot for flat lensing (Aieta et al., 2012). By constructing anisotropic structures that alter the phase for one polarization direction but not another, metasurface waveplates have been realized (Yu et al., 2012; Yu & Capasso, 2014) that are orders of magnitude smaller than conventional birefringent crystal waveplates. Additionally, several more advanced techniques such as metasurface holography (L. Huang et al., 2013; J. Lin et al., 2013) and optical cloaking (Ni et al., 2015) via customized spatial phase distributions using meta-optic architectures have been explored.

The application space of such ultrathin devices would be greatly enhanced if it were possible to actively tune their properties and realize real-time switching. Creating nanoscale versions of tunable beam steering elements, phase manipulators, holograms, or cloaks would be a tremendous asset in miniaturizing existing tunable devices. As such, there has been a large effort within the metamaterial community within the past decade to integrate active components within meta-optics for modifying phase at-will. Rather than suppressing resonant modes due to loss (as seen in Chapters 4 and 5), phase modulation techniques largely rely on spectrally shifting a resonant mode through the operation wavelength. Numerous approaches have been investigated for such modulation including carrier modulation in semiconductors (Chan et al., 2009), two-dimensional materials (H. Li et al., 2016), phase-change media (Samson et al., 2010), mechanical actuation (Ou et al., 2013), and liquid crystals (Komar et al., 2017). However, many of these techniques trade modulation depth for switching speed or required power to operate. For example, 2D-integrated active metasurfaces often suffer from low modulation depths due to the small interaction volume, and MEMS-type architectures are typically slow due to low mechanical Q-factors. Some recent work has achieved large phase modulation (>300°) by incorporating multiple interaction layers (Kafaie Shirmanesh et al., 2018), but encounter a common issue when shifting resonances in the frequency domain: low output efficiency and highly variable amplitude.

In this chapter, we explore how to overcome these issues by integrating dielectric resonances with intersubband transitions (IST) in multi-quantum well (MQW) structures. While there have been previous investigations of quantum well-based metasurfaces (Campione et al., 2014), our design increases the interaction between the particle resonance and the quantum wells by combining the two into one resonator. Additionally, quantum wells are advantageous since the use of ISTs for modulation is a purely electro-optic effect; therefore, the modulation speed of the system will be limited only by the time constant of the biasing circuit. We have also engineered a special resonator architecture that ensures a constant reflection amplitude (0.6) with a phase tunability of nearly 180 degrees. Further, this geometry in sensitive to the incident polarization, allowing for tunable waveplate functionality by altering the phase delay between orthogonal incident polarization states. By further investigating this approach, we believe this metasurface design can serve as a strong candidate for fast and highly adjustable ultrathin phase modulators.

6.2. Fundamental Properties of Quantum Wells

The size dependence of optical properties in very small crystals is a consequence of quantum confinement. The Heisenberg Uncertainty principle explains that is a particle is confined to a region of length Δx, we introduce a corresponding uncertainty in its momentum Δp_x. The kinetic energy gained from this momentum is significant if it is comparable or greater than the kinetic energy of the particle due to its thermal motion (Fox, 2012). In the 1D case, quantum size effects will emerge if:

$$\Delta x \leq \sqrt{\frac{h^2}{4\pi^2 m k_B T}} \tag{10}$$

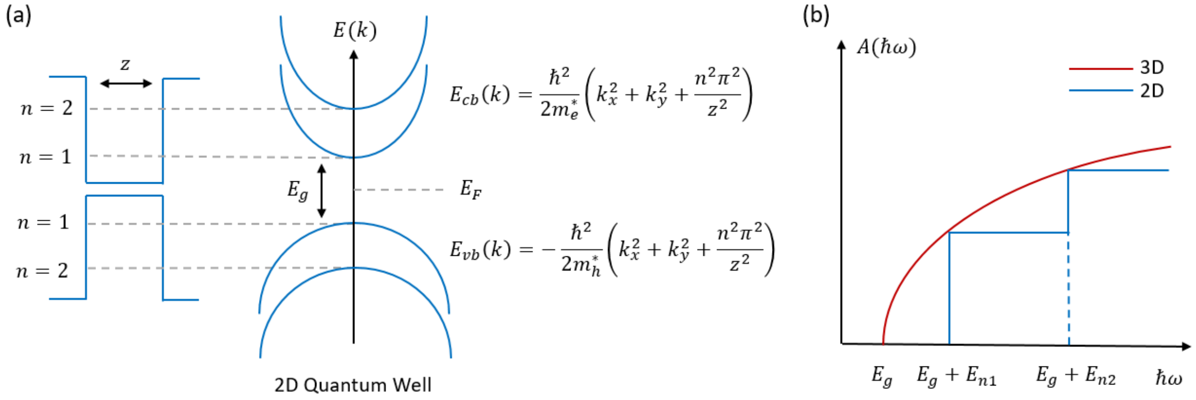

Figure 6.1: Quantum confinement in a quantum well. (a) Energy and E-k diagram for a quantum well structure. The "well" material has a smaller bandgap than the "wall" materials, creating a finite square well potential that quantizes the allowed energy levels. This corresponds to discrete bands in the E-k diagram. Energy labels are marked with index n. (b) Absorption for 2D (quantum confined) and 3D material systems. The quantization of the bands create the "step-like" density of states pattern as a function of energy.

Here, h is Planck's constant, m is the object mass, k_B is Boltzmann's constant, and T is the temperature. For an electron at room temperature in a typical semiconductor, $\Delta x \approx 5$nm. Quantum wells are artificial heterostructures containing layers of different materials thin enough to possess quantum confinement effects. They are often made with III-V materials such as GaAs, InGaAs, or AlGaAs due to their similar lattice constants and ease of growing thin layers on top of one another via molecular beam epitaxy (MBE). Since ultrathin layers confine electrons in one dimension, the energy levels formed in the conduction band of quantum wells are quantized in resemblance to the famous elementary quantum mechanics problem: the finite square well, as seen in Figure 6.1(a,b). This discretization results in a "step-like" absorption pattern (Figure 6.1(b)) whose energies are limited to the differences between the valence and conduction bands (interband transitions) or subbands within either the valence or conduction bands (intersubband transitions).

6.3. Intersubband Transitions and the Quantum Confined Stark Effect

As seen in Section 6.2, quantum wells possess intersubband transitions with energy levels similar to that of the finite square well problem. The application of a perpendicular electric field through quantum wells will ionize excitons (electron-hole pairs) by pushing electrons and holes in opposite directions (Fox, 2012). This is known as the quantum confined Stark effect, and is the primary mechanism used for emission in quantum cascade lasers (QCLs). Since quantum wells confine electrons and holes, the excitons are not ripped apart and interact with the field, affecting their energy. The amount that each energy level changes upon experiencing a perpendicular field is described by second-order time-independent perturbation theory. For a quantum well confined in the ẑ direction and a ẑ-oriented electric field of strength F, the subband energy shift due to the applied field can be described by the following (Chuang, 2009):

$$\Delta E = E - E_n^0 = \frac{n^2\pi^2 - 15}{24n^4\pi^4}\frac{4\pi^2 m e^2 F^2 L^4}{h^2} \tag{11}$$

Here, E_n^0 is the energy of the nth state of an infinite quantum well without an applied electric field, n is the IST state, and L is the length of the quantum well. Notably, the energy difference between

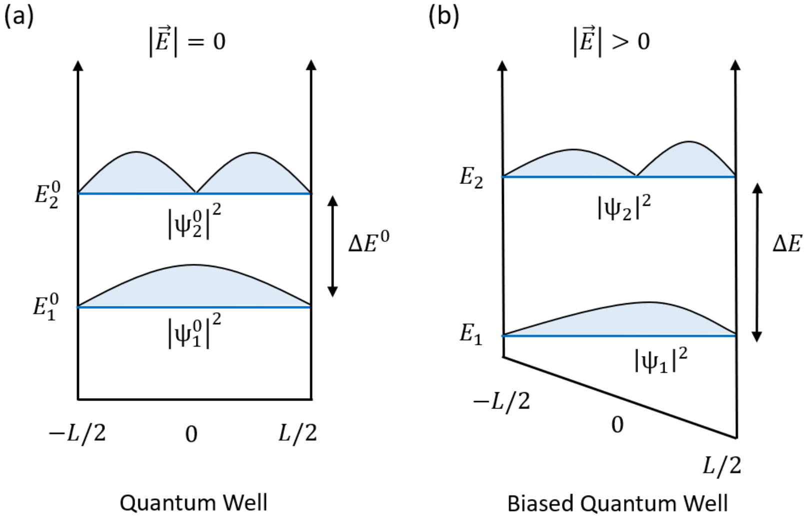

Figure 6.2: The quantum confined Stark effect. (a) Energy diagram of a quantum well with two conduction subbands and no applied electric field. (b) Similar diagram of a quantum well with an external perpendicular applied field. The relative position of the two subbands shift due to the QCSE, adjusting the IST energy ΔE.

the first two states in the conduction band (n=1,2) increases with applied electric field since ΔE_1 is negative whereas ΔE_2 is positive, resulting in a blue shifted absorption energy for the IST. This process is summarized in Figure 6.2.

Since the shift scales with electric field strength, it is possible to reversibly control the IST energy by scaling the applied field appropriately. This modulation will serve as the active element in our metasurface architecture, which will be described in Section 6.4. Since the QCSE is a purely electro-optic effect that involves no carrier injection, modulation speeds of the IST energy are limited only by the RC time constant of the biasing circuit used to apply the electric field.

More generally, quantum transitions have an associated matrix element (μ) that governs the directionality of the transition and the transition rate. The matrix element for ISTs is expressed as follows for a quantum well confined in the ẑ-direction (Chuang, 2009):

$$\mu_{ba} = \langle \Psi_b | e\boldsymbol{r} | \Psi_a \rangle = \delta_{k,k'} \langle \varphi_b | e\boldsymbol{z} | \varphi_a \rangle \hat{z} \tag{10}$$

Here, Ψ is the wave function associated with states a and b, $\delta_{k,k'}$ is the Dirac delta function for the wave vectors of the two wave functions Ψ_a and Ψ_b, and φ is the ẑ-component of Ψ. Importantly, the matrix element only has a ẑ-component since the other directional components are zero. Therefore, ISTs only experience absorption for light polarized along ẑ. For normal-incidence light on a typical quantum well system (layers grown in the ẑ-direction), ISTs are inaccessible without additional complexity introduced to the system.

6.4. Metasurface Architecture and Simulated Performance

We can achieve phase modulation by controlling the degree of interaction between ISTs in quantum wells and Mie-type resonances in dielectric particles. Since the coupling strength between two resonances relies on both spectral and spatial overlap, the quantum well structures must be in

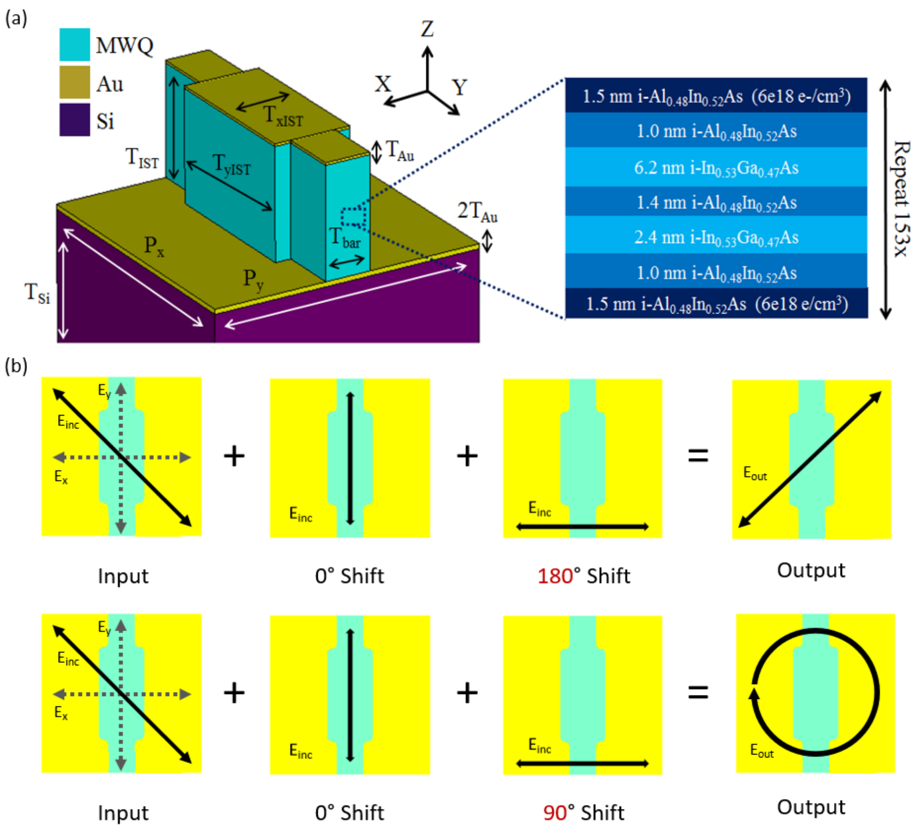

Figure 6.3: Metasurface design and functionality. (a) Unit cell architecture and quantum well design parameters. $P_x = P_y = 6.0\mu m$, $T_{Si} = 10\mu m$ (in simulations), $T_{Au} = 50nm$, $T_{bar} = 1\mu m$, $T_{xIST} = 1.7\mu m$, $T_{yIST} = 3.4\mu m$, and $T_{IST} = 2.3\mu m$. (b) Intended performance as a tunable waveplate. Since phase modulation is controlled for E_x polarization but not E_y, controlling the phase delay between the two can result in conversion from linearly polarized light to (Top) its cross-polarized state, or (Bottom) to circular polarization.

close physical proximity to the fields of the Mie-type resonator. Additionally, in order to observe a modulation in phase, we must access the strong coupling regime of the resonator-quantum well system. The most prominent feature of strong coupling between a cavity resonance (such as Mie-type dipole) and a two-level system (such as an IST in a quantum well) is the splitting of the absorption resonance peak into two in the frequency domain. This phenomenon is called Rabi splitting and is most commonly explained using the Jaynes-Cummings model (Jaynes & Cummings, 1963). The strength of the coupling dictates the splitting, or separation of the two peaks from the overlapped resonant energy, similar to how coupling two classical pendulums together by a spring splits the central oscillation frequency into two normal modes with different frequencies. By harnessing the QCSE, it is possible to reversibly overlap a Mie-type resonance with the IST frequency of quantum wells, therefore controlling the degree of coupling between the two and the overall phase response of the combined system.

The metasurface architecture coupling the ISTs to the dielectric Mie-type resonance is pictured in Figure 6.3. To maximize the coupling, the dielectric resonator is made entirely of quantum wells. The dimensions of the resonator are specifically designed to support a magnetic dipole resonance at nearly the same energy as the IST of the quantum well stack. The QW stack consists of repeating layers of InGaAs and InAlAs material organized into a double well structure of lengths 6.2nm and 2.4nm respectively. The additional complexity here is beneficial since a larger quantum confined Stark shift can be realized by introducing coupling between two QWs of different thicknesses in a multi-QW heterostructure (Mii, Karunasiri, Wang, Chen, & Yuh, 1990). Finally, the gold backplane and bar on top of the resonator serve as electrical contacts to provide the required field to tune the QW IST energy via the QCSE.

As mentioned in Section 6.3, a strong electric field perpendicular to the QW heterostructures ($\hat{z}$) is needed to successfully couple the IST to the Mie resonance since the matrix element of the IST is nonzero only along the z-axis. Incoming light at normal incidence does not provide this field, so we must rely on the magnetic dipole resonance of the particle. The resonator was specifically designed to support such a mode upon excitation with polarization along the x-axis (Figure 6.3(a)). A magnetic dipole mode generates a circulating electric field via Ampere's Law (Section 1.2), which provides the necessary $\hat{z}$-oriented field to access the QW IST. The reason for this anisotropy is illustrated in Figure 6.3(b). If the magnetic dipole mode is only spectrally overlapped with the QW IST for light polarized along the x-axis, then only incoming light with an

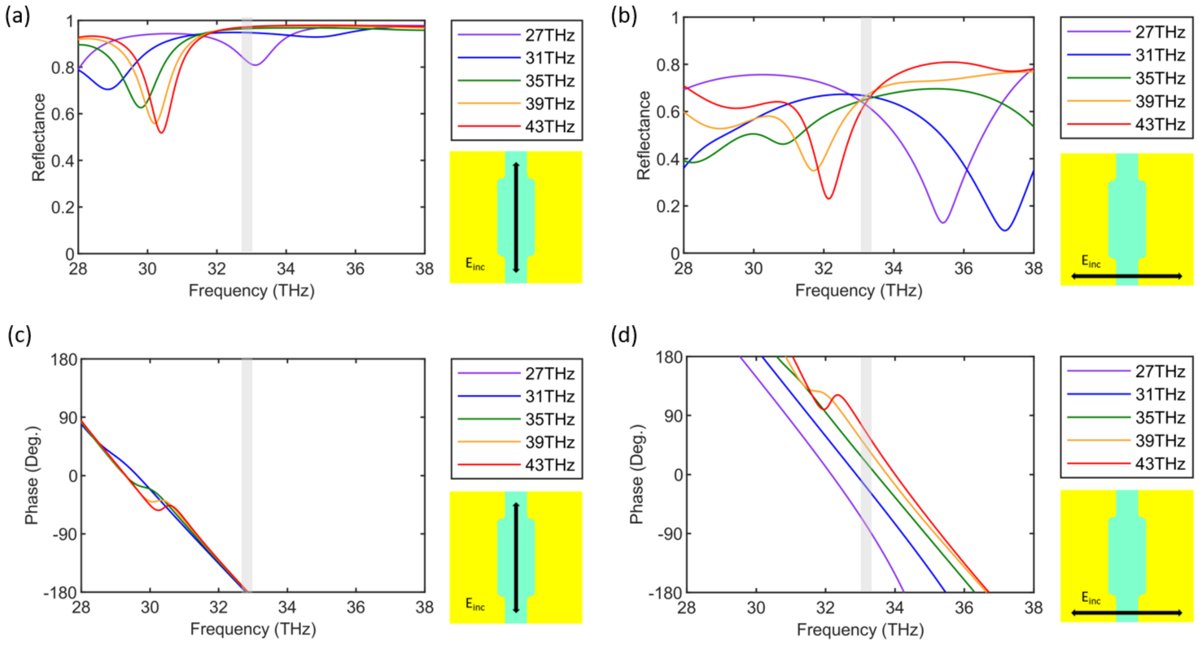

Figure 6.4: Simulated metasurface performance for phase tunability and polarization conversion. (a,b) Reflected amplitude as a function of frequency for several values of the QW IST energy. The desired operation wavelength is at 33.2THz, where the reflected amplitude remains constant for both polarizations. (c,d) Reflected phase as a function of frequency for the same QW IST energies shown in (a,b). Importantly, only the polarization in (d) experiences a change in phase, while the polarization in (c) remains at the same phase as the QW IST energy is changed.

electric field component in the x-direction will have its phase modified via coupling to the QW ISTs. For the orthogonal polarization state (along the y-axis), the resonator dimensions do not support a magnetic dipole mode at the same energy as the QW ISTs, and therefore there is no coupling the particle to the QW IST. This way, we have engineered an artificial phase delay between orthogonal polarization states at normal incidence. This delay is controllable by tuning the QW IST energy closer or farther away from the energy of the (static) magnetic Mie mode in the resonator. As seen in Figure 6.3(b), if the incident light is polarized at 45° off axis (such that there are equal incident components along the x- and y-axes) and the phase delay is set to 90°, linearly polarized light will be converted to circularly polarized light. Similarly, if the phase delay is set to 180°, linearly polarized light will be converted to its cross-polarized state.

To function as an effective polarization converter, the metasurface must possess two essential characteristics. First, to ensure high efficiency, illumination along either optical axis should result in a relatively high reflection coefficient. Second, even if the reflection is not unity, illumination along either optical axis should result in the same reflection coefficient. This is to ensure we obtain circularly polarized light instead of an elliptically polarized signal upon conversion. Finally, the required phase delay for conversion (π/2 for linear to circular, π for linear to cross-polarized linear) must occur between orthogonal incident polarizations.

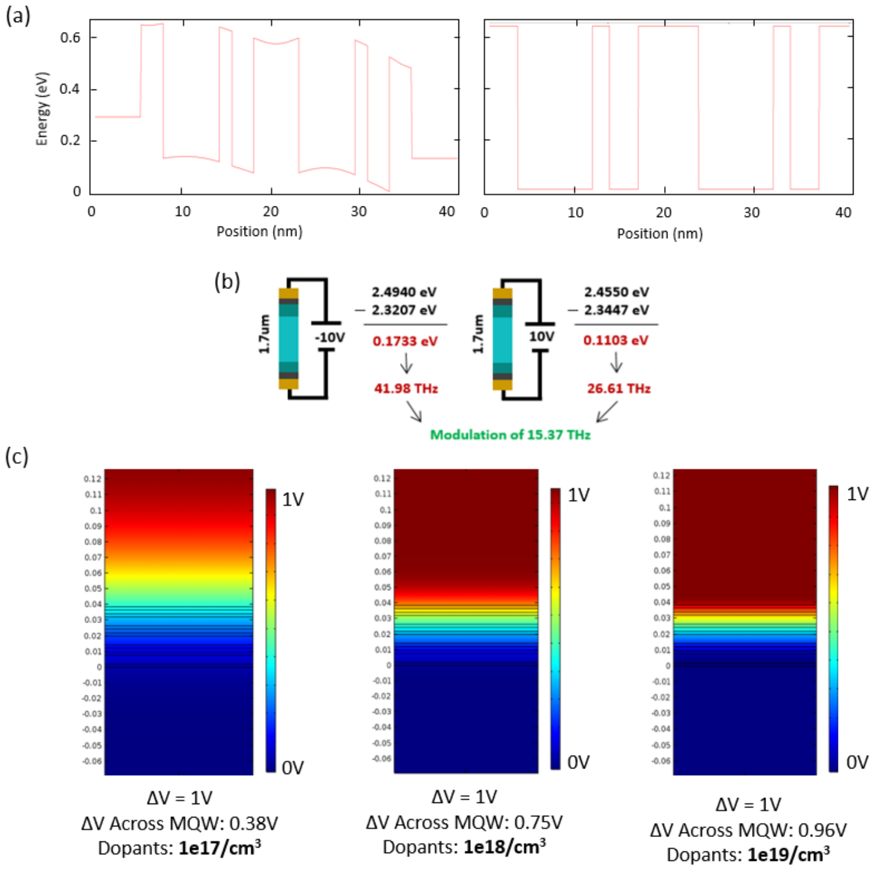

Figure 6.5: Investigation of realistic voltage parameters for the MQW stack. (a) Conduction band structure of the MQW stack under (left) 10V bias voltage and (right) no bias voltage. (b) Maximum QW IST frequency modulation with a bias range of ±10V. (c) Side profile of proposed resonator architecture where the top and bottom portions are replaced with doped semiconductor. Larger dopant concentrations result in the potential gradient becoming increasing concentrated in the MQW region.

As seen in Figure 6.4(a,b), the reflection coefficient for polarizations along both optical axes remains high regardless of the QW IST energy. This is expected for the polarization in (a) since the IST is not coupled to any dielectric Mie mode in the resonator. Despite the reflection being both large and constant across the simulated range of IST energies, the average value is different between polarizations: 0.6 in (b) and 0.9 in (a). The phase information is depicted in Figure 6.4(c,d). Again, the polarization in (c) experiences no phase shift for various IST frequencies, whereas the polarization in (d) experiences nearly 150° as the IST energy is varied form 43 THz to 27 THz. This means conversion from linear to circularly polarized light is possible with this metasurface, but in order to achieve the phase modulation required for linear to cross-linear polarization conversion, the IST energy must be tuned further.

One factor that must be considered is the actual physical tuning range of the QW IST frequency. It is essential to calculate the expected IST shift for an applied bias voltage to determine what input power is required to modulate the metasurface. This information can be obtained by using a 1D Schrodinger equation solver to estimate the energies of the conduction subbands in the quantum wells and analyzing how much those energies change for reasonable input voltages. Figure 6.5(a) depicts the quantum well energy diagram for both an unbiased system and one using 10V to bias the MQW stack. As expected, the voltage tilts the bands, and the IST frequency is extracted in Figure 6.5(b). This value is determined by taking the energy of the n=2 subband and subtracting the energy of the n=1 subband. For a bias voltage of ±10V, the IST frequency range is 42.0THz to 26.6THz. Based on these results and Figure 6.4(d), this voltage range is sufficient for 90° of phase tunability, but not 180°.

Additionally, since the quantum wells have various doping levels within each layer, there will be some degree of screening as a bias voltage is applied across the MQW stack. In order to maximize the QCSE and therefore the modulation capabilities of the device, it is desirable for the potential drop between the top gold electrode and backplane to occur as evenly across the MQW region as possible. Since the z-oriented electric fields provided by the magnetic Mie dipole resonance are strongest in the middle of the resonator, one solution is to replace the top and bottom portions of the MQW resonator with a doped semiconductor. If there is comparatively little voltage drop across these buffer regions, then most of the voltage drop will occur across the QWs in the middle of the resonator. If most of the applied field is lost in the semiconductor layers, then less field will interact with the QWs and stifle the QCSE. As seen in Figure 6.5(c), using GaAs as a top and bottom buffer layer with a dopant concentration of $1x10^{19}e\text{-}/cm^3$ results in a 96% potential drop across the QW region, whereas a smaller potential gradient is observed for architectures with fewer dopants in the buffer regions.

6.5. Fabrication Procedure

To realize this metasurface architecture, the MQW stack is first grown using molecular beam epitaxy (MBE). Then, gold is deposited on the quantum well stack and the target adhesion wafer. The two are compressed together in a configuration known as “flip chip” bonding. The combined wafer stack is heated, and the two pieces are fused via thermocompressive bonding. Afterwards, the handling wafer that the MQWs were grown on is grinded away using a lapping tool (several times, using progressively finer grit). Then, a wet chemical etch process is used to selectively dissolve the seed layer of InGaAs used to grow the MQWs (4:1 $C_6H_8O_7$:H_2O_2). The top gold contact layer is deposited, and a normal round of electron beam lithography, development, RIE, and liftoff is performed to define the resonator pattern. Finally, the top and bottom electrodes are connected to a voltage source for biasing.

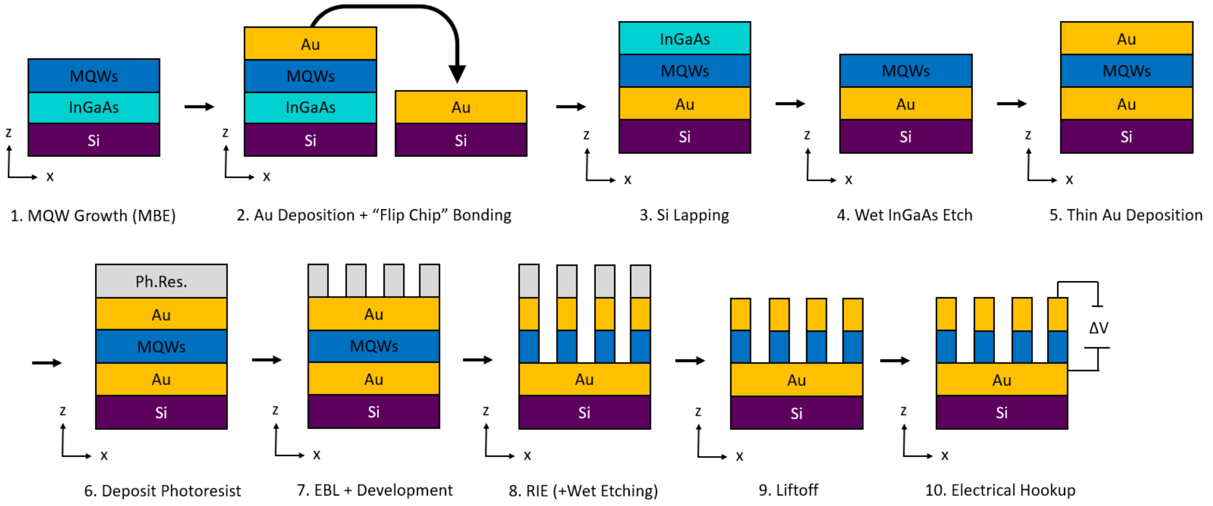

Figure 6.6: Fabrication procedure for the MQW-integrated metasurface phase modulators. Flip chip bonding is required to ensure a continuous Au backplane underneath the MQW layer. If Au sputtering upon dry etching in step 8 is an issue, the top layer of Au can be removed in step 5 and replaced in step 10 after the resonators are defined.

6.6. Future Plans

6.6.1. Fabrication Completion

One challenge surrounding the fabrication process has been the reactive ion etching step in defining the resonators. In the current configuration (Figure 6.6), the top gold contact layer is deposited before the dry etch step. The dry etching is responsible for selectively consuming the top gold layer and the MQW stack. However, the top gold tends to sputter and redeposit on the entire sample during the process, which results in a thin film of gold on the sides of the resonator structure. This would short the device and render it unusable for biasing experiments.

The second issue with the current fabrication procedure has been the development of a reactive ion etching (RIE) recipe that etches the MQW stack with high anisotropy. Our best efforts currently result in a frustum architecture with a sidewall angle of approximately 15 degrees. One solution to solving the gold sputtering issue would be to wait until the resonators are defined before depositing the top gold contact layer. However, if there is a sidewall angle to the MQW etch, the same issue would remain of gold being deposited on the resonator sidewalls, shorting the device. There is the possibility of defining a second mask via EBL purely for the top contact, but this approach requires precise alignment and an incredibly thick photoresist that would remain largely uniform despite the underlying MQW resonators. Further fine-tuning of the RIE recipe is needed before continuing with final devices for measurement.

6.6.2. Characterization and Measurement

Once the devices are completed, the final step is to verify that they work as intended. Doing so involves four main experiments. First, a mid-IR spectroscopy setup is needed to determine the reflection spectrum for both incident polarizations as a function of bias voltage. Second, the voltage-dependent reflected phase at the designed operational wavelength will need to be determined using a Michaelson interferometer setup equipped with a QCL. Third, the switching speed and maximum rate of phase modulation will need to be determined. Finally, it would be beneficial to examine the overall life cycle of the device by conducting cycling and degradation tests to determine the experimental limits on the system.

6.7. Conclusions

In summary, this chapter has outlined the design and realization of a mid-IR phase modulator based on changing the IST frequency of quantum wells using the QCSE. By physically and spectrally overlapping Mie resonances in dielectric particles with the IST energy, we have created a unique architecture that provides the necessary $\hat{z}$-oriented electric field (as required by the IST matrix element) to both couple incident light to the IST and change the reflected phase by moving the system in or out of the strong coupling regime. By ensuring that this response is achieved for one incident polarization, the built-in anisotropy enables the device to operate as an ultrathin tunable waveplate. The expected phase modulation is approximately 150° within an IST frequency range of 27 – 43THz. Additionally, this design benefits from the reflected amplitude remaining largely constant (0.6) over its tuning range and a theoretical modulation speed that is limited only by the RC time constant of the biasing circuit used to induce the QCSE. While additional work is needed to complete the fabrication and ensure proper electrical performance, this approach towards metasurface-based phase tuning is a promising candidate for the future of mid-IR ultrathin modulators.

CHAPTER 7

Conclusions and Outlook

The focus of my Ph.D. research has been to explore and surpass the limits of metasurface technology by combining electromagnetic modes of dielectric particles and tunable media in unique ways. As seen in several material systems, the work outlined previously has resulted in new architectures that have pushed the boundaries of narrow-band thermal emission, high-efficiency n-IR transmission control, ultrathin optical limiting, and dynamic phase tuning. In this chapter, I will summarize all of the results presented in this dissertation and provide some potential avenues towards future research. Additionally, I will discuss the main challenges that currently limit the use of such technologies outside of research settings and direct attention to some recent developments that I believe could alleviate those issues in coming years.

In Chapter 2, we explored the consequences of engineering Mie resonances in media with extreme material parameters such as large permittivity and dispersion. The beneficial properties elucidated here paved the way towards Chapter 3, in which we engineered a deeply subwavelength dielectric metasurface with narrow-band and near-unity emissivity. This is accomplished by utilizing spectrally overlapped electric and magnetic dipole resonances featuring equal oscillator strength (Decker et al., 2015; Monticone et al., 2013; Pfeiffer et al., 2014; Pfeiffer & Grbic, 2013b). While this condition would result in near-unity transmittance in the absence of loss (Huygens mode), we demonstrate that if absorption loss is present, and the losses in the dipole modes are balanced, then the result in near-unity absorption. Further, implementing this architecture in highly dispersive and high permittivity media results in narrowband absorption and thermal emission that is insensitive to the angle of incidence up to 50° off-normal. The metasurfaces are also highly transmissive off-resonance. This special type of device, which we call “balanced metasurfaces”, are realized experimentally using deeply subwavelength ($\lambda_{free\text{-}space}$/6.6) 3C-SiC nanopillar arrays, from which we observe 78% absorptance with a quality factor of 170. Due to its simple architecture, high quality, and insensitivity to angle of incidence, this design could be a strong candidate for future narrow-band IR sources.

In Chapter 4, we presented a dynamic metasurface that operates in transmission at telecom wavelengths. In order to overcome the large mode volume in dielectric resonators, we take advantage of an epsilon-near-zero (ENZ) mode in an electrically tunable indium tin oxide (ITO) layer. Operating at the ENZ point provides for large local field enhancement within the ITO, leading to dynamic transmission control. Here, we utilize a Huygens mode in the dielectric resonators to minimize impedance mismatch and maximize transmittance, allowing a maximum experimental transmittance of 70% and modulation depth of 31%. By doing so, this architecture offers a unique solution for compact spatial light modulators and/or tunable filters in the n-IR.

In Chapter 5, we designed an ultrathin optical limiter by integrating VO_2 with an all-dielectric metasurface. This structure also supports a Huygens mode with characteristically high transmittance in the on-state. An epsilon-near-zero (ENZ) mode of the VO_2 is introduced to damp the transmission. The limiting behavior of the device triggers when the incident intensity grows strong enough to trigger the metal-insulator transition of VO_2. These devices are experimentally realized, achieving 7.7dB transmission contrast with an off-state transmission of -4.1dB at an operating wavelength of 1.24μm. Due to the large cutoff efficiency and transmissive architecture, we believe this optical limiter design can contribute to highly secure real-time detection and sensing applications without the threat of overheating or damaging equipment.

Finally, in Chapter 6, we designed a reflective metasurface that modulates phase by integrating dielectric resonances with intersubband transitions (IST) in multi-quantum well (MQW) structures. Using the quantum confined Stark effect, the IST energy can be tuned towards or away from the magnetic dipole Mie mode energy, governing the strong coupling response. We provide a resonator architecture that ensures a constant reflection amplitude (0.6) with a phase tunability of nearly 180 degrees. Further, this geometry in sensitive to the incident polarization, allowing for tunable waveplate functionality by altering the phase delay between orthogonal incident polarization states. By further investigating this approach, we believe this metasurface design can serve as a strong candidate for fast and highly adjustable ultrathin phase modulators.

There any many interesting future research directions that can improve upon the results in this dissertation. For the work in Chapter 3, the design architecture can easily be expanded to include other polar materials in the mid-IR. Additionally, this approach is well-suited for flexible substrates such as PDMS since the resonators are highly insensitive the incident angle. Finally, since the design is highly transmissive off-resonance, one could engineer custom emission spectra by stacking individual resonator layers of different sizes to provide emission over a broader bandwidth. For the work in Chapter 4, one of the main drawbacks of the metasurface performance is the switching speed. Improving the mobility of the electrolyte or replacing the electrode material with another compact and conductive material such as graphene could significantly boost performance. To increase the transmittance tunability, it is possible to use a dual-gate design where ITO layers are both on the top and bottom of the silicon cylinder. For the VO_2-based optical limiter work in Chapter 5, we can potentially engineer designer-wavelength limiting by designing multilayer structures with resonator sizes corresponding to different wavelengths at each layer. Additionally, it would be highly beneficial to design a limiter structure that is reflection-based to eliminate the problem of a low damage threshold. Finally, there is much work to be done with the architecture in Chapter 6 to make the reflected phase more sensitive to the IST frequency, allowing for a larger phase modulation upon electrical bias.

Metasurfaces, and more generally nanoscale optoelectronic devices, provide an exciting degree of new functionality and customizability that paves the way towards new technologies or miniaturized versions of existing devices. The evolution of metamaterial designs in the past fifteen years has benefitted tremendously from developments in materials science; the variety of complex material systems harnessed in today’s tunable meta-devices reflect the maturity of the field of study. However, metasurfaces have largely failed to make the transition from research laboratories to commercial products. The primary reason for this lies in scalability and cost, particularly for meta-optics engineered for visible or n-IR light where resonators’ largest features are often a few hundred nanometers. For metasurfaces to make a real impact in this technology space, the challenge of cost-effective fabrication must be conquered in the coming years. Various methods such as chemical self-assembly, pattern transfer lithography, nano-imprint, and micro-sphere projection have been explored recently and are making developments in reducing the need for electron beam lithography for smaller feature sizes (Su, Chu, Sun, & Tsai, 2018). Whether such techniques will be able to advance enough to create large-area devices at low cost with sufficient reproducibility and precision will be critical to the future of optical metasurfaces as a viable technological platform.

APPENDIX A

Fabrication Details

A.1. Reactive Ion Etching Recipes

Reactive Ion Etching was commonly used throughout the projects in this dissertation to define nanostructures in the z-direction. This was performed in the standard manner: define a hard metal mask using electron beam lithography (or similar lithography techniques) and rely on the high selectivity between the mask and the etched material. Two main materials were etched in this way for the metasurfaces described in this dissertation: silicon and 3C-SiC. For completeness and reproducibility, the recipes for etching those materials are discussed in this section.

For silicon etching, the best performing recipe included a gas chemistry of CF_6/C_4F_8 with 28/47sccm respectively, a chamber pressure of 10mTorr, process temperature of 10°C, RF power of 30W, and ICP power of 1000W. The directionality of this etch was highly anisotropic and

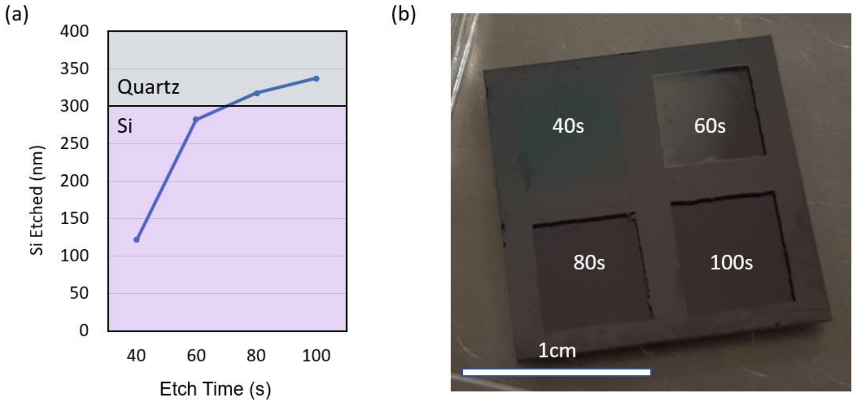

Figure A.1: Etch rate study of silicon using reactive ion etching. (a) Amount of silicon etched as a function of etch time using the recipe discussed in section A.1. (b) Optical image of a Si/Quartz wafer sample with four areas etched for different times. The Si thickness is 282nm, and as a result the areas etched for longer times are transparent. The labels correspond with the data points in (a).

resulted in straight sidewalls. The etch rate is described by Figure A.1. While day-to-day variations in chamber conditions and substrate thermal contact affect etch rates, we were able to follow these results as a guideline for silicon etch times.

For 3C-SiC etching, the best performing recipe included a gas chemistry of $O_2/SF_6/C_4F_8$ with 10/100/150sccm, respectively. The etch parameters were RF power = 100W, ICP power = 2000W, chamber pressure = 10mTorr, and process temperature 10°C. The directionality of this etch was less anisotropic, resulting in sidewall angles of approximately 15 degrees (See Figure 2.6); however, this angle was the best (lowest) of any combination of gases and pressures examined during process development. Notably, this etch was also significantly less selective compared to traditional metal masks compared to the silicon etch recipe. In order to survive a 2μm 3C-SiC etch, 100nm of Cr was necessary using the above recipe.

A.2. Thermal Oxidation of Silicon

The thermal oxidation of silicon is commonly approached using the Deal-Grove model (Deal & Grove, 1965). By heating silicon in an oxygen-rich environment, a thin film of SiO_2 will grow on the surface. The rate of this growth is determined by the following expression in the 1D case (a perfectly flat surface):

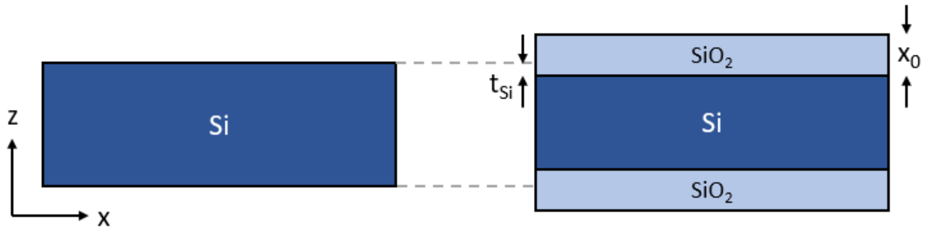

Figure A.2: Illustration of thermal oxidation of silicon. In an oxygen-rich environment at high temperatures, oxide layers will grow around existing silicon. The rate is characterized by the Deal-Grove model.

$$x_0 = \frac{A}{2}\left(\sqrt{1 + \frac{4B}{A^2}(t + T)} - 1\right) \tag{12}$$

Here, x_0 is the oxide thickness and both A and B are temperature-dependent variables that relate to the conversion rate of silicon. At a temperature of 1000°C, A = 0.165µm and B = 0.0117um^2/hr. T is the thickness of any pre-existing oxide on the surface (T = 0 for all cases in this dissertation), and t is the time in hours spent at the temperature corresponding to the parameters A and B. Notably, some of the underlying silicon is consumed to create the SiO_2 film, but the rate of growth of the SiO_2 film and consumption of silicon are not equal ($t_{Si} = 0.46x_0$). This is represented in Figure A.2.

In the context of this dissertation, thermal oxidation is used as a precise method of controlling the thickness of a thin silicon film. For example, in Chapter 4, we require the height of silicon resonators to be a specific value (230nm), but at the time of the experiment, we had wafers of 300nm silicon on quartz. We controllably converted the top layer of a silicon film to SiO_2 as a function of time, and then removed the top film of SiO_2 with HF (Hydrofluoric Acid). This way, we were able to strip away just enough silicon to create samples of the desired thickness. This level of precision and uniformity is not possible using reactive ion etching (RIE), so the oxidation process was critical to the results of Chapter 4.

Time (Hr)	x_0 (nm)	t_{Si} (nm)	Exp. t_{Si} (nm)
0.5	30.0	13.8	11
1.5	73.5	33.8	31
2.5	107.3	49.3	45
3.5	136.0	62.6	60
4.5	161.2	74.2	77

Table A.1: Confirmation of Deal-Grove model for thermal oxidation of silicon. The first three columns correspond to the model described in Section A.2, and the final column is the experimental values of t_{Si}.

This procedure was confirmed by testing the rate of oxidation / silicon conversion in a tube furnace in VINSE. The theoretical oxidation parameters and experimental results are provided in Table A.1 and based off a comparison between t_{Si} and experimentally measured t_{Si} via AFM and ellipsometry, provide excellent results with the Deal-Grove model.

A.3. Solid Electrolyte Preparation

In Chapter 4, we discussed the use of a solid electrolyte that was used as a transparent top gate to actively tune the properties of a transmission modulator. The process for creating this solution is described here, although the original work in which the electrolyte was developed and used is also provided (Prasai et al., 2015).

To create the solid electrolyte, 0.05g of bi-(trifluoromethylsylfonyl) amine lithium salt was dissolved alongside 0.3g of poly(ethylene oxide) in 20ml of acetonitrile. It is important to mix this solution well (>400rpm with a magnetic stir bar on a hot plate) at 90°C for 5 min. The mixture should appear cloudy. Afterwards, the solution should be transferred to two vials and centrifuged at 6000rpm for 15min. Once complete, the precipitate will be condensed at the bottom of the vials. The best electrolyte is at the top of the vial – pipetting this fraction of the centrifuged vial into separate airtight containers results in the best electrolyte.

To apply the electrolyte, we drop cast the solution onto our sample, spin coat the mixture at 800rpm for 1 min, and baked the sample on a hot plate at 90°C for 5 min to harden.

A.4. Thermal Emissivity Spectra Calibration

For a thermal emissivity measurement to have any quantitative meaning, it must be properly normalized and calibrated to the instrument being used. In the case of measuring the emissivity of 3C-SiC metasurfaces in Chapter 3, we used a Fourier transform infrared (FTIR) spectrometer. This normalization is necessary because many other components within the measurement apparatus itself also radiate, such as beam splitters, mirrors, lenses, filters, and amplifiers. Additionally, the transmittance of the atmosphere must be considered, especially in the mid-wave and long-wave infrared. These conditions can be considered by performing additional measurements with samples of known emissivity (black bodies) and folding their spectra into the measurement of the unknown sample (T. G. Folland, Nordin, Wasserman, & Caldwell, 2019).

A properly calibrated emission spectrum will take the form:

$$\mathrm{L}_{\mathrm{v}}(\nu) = \frac{S(\nu)}{R(\nu)} - G(\nu) \tag{13}$$

Here, $L_v(\nu)$ is the spectral radiance of the sample surface, $S(\nu)$ is the measured spectrum of the sample, $R(\nu)$ is the influence of the atmosphere on the emissivity, and $G(\nu)$ is the radiance from the spectrometer's internal parts. In order to calibrate the spectrum, we need forms for $R(\nu)$ and $G(\nu)$. They can be expressed as follows:

$$R(\nu) = \frac{S_1(\nu) - S_2(\nu)}{L_{\nu 1}(\nu) - L_{\nu 2}(\nu)} \qquad G(\nu) = \frac{S_1(\nu)}{R(\nu)} - L_{\nu 1}(\nu) \tag{14.15}$$

Here, $L_{\nu 1}(\nu)$ and $L_{\nu 2}(\nu)$ are the radiance of a black body at temperatures T_1 and T_2. The expressions for these two functions simply follow Planck's Law. $S_1(\nu)$ and $S_2(\nu)$ are measured spectra of a black body source using the same measurement tool as $L_v(\nu)$ at the two temperatures T_1 and T_2. In our measurement setup, we used a carbon nanotube array whose emissivity was independently verified to be >0.95 across the near-, mid-, and long-wave IR, and the two temperatures used were re, $T_1 = 250K$ and $T_2 = 300K$. With this information, it is possible to generate a calibrated emission spectrum $\mathrm{L}_{\mathrm{v}}(\nu)$ from Equation 9.

REFERENCES

A. Evlyukhin, S. Novikov, U. Zyweitz, R. Eriksen, C. Reinhardt, S. Bozhevolnyi, B. C. (2012). Demonstration of Magnetic Dipole Resonances of Dielectric Nanospheres i the Visible Region. *Nano Letters*, **12**, 3749–3755.

Abdollahramezani, S., Taghinejad, H., Nejad, Y. K., Eftekhar, A. A., & Adibi, A. (2018). Dynamic dielectric metasurfaces incorporating phase-change material. *2018 Conference on Lasers and Electro-Optics, CLEO 2018 - Proceedings*, **1**, 1–2.

Aieta, F., Genevet, P., Kats, M. A., Yu, N., Blanchard, R., Gaburro, Z., & Capasso, F. (2012). Aberration-free ultrathin flat lenses and axicons at telecom wavelengths based on plasmonic metasurfaces. *Nano Letters*, **12**, 4932–4936.

Alaee, R., Albooyeh, M., & Rockstuhl, C. (2017). Theory of metasurface based perfect absorbers. *Journal of Physics D: Applied Physics*, **50**, 1–14.

Ali, H. E. (2019). A novel optical limiter and UV–Visible filters made of Poly (vinyl alcohol)/KMnO4 polymeric films on glass-based substrate. *Journal of Materials Science: Materials in Electronics*, **30**, 7043–7053.

Alù, A., Silveirinha, M. G., Salandrino, A., & Engheta, N. (2007). Epsilon-near-zero metamaterials and electromagnetic sources: Tailoring the radiation phase pattern. *Physical Review B - Condensed Matter and Materials Physics*, **75**, 1–13.

Arbabi, A., Horie, Y., Ball, A. J., Bagheri, M., & Faraon, A. (2015). Subwavelength-thick lenses with high numerical apertures and large efficiency based on high-contrast transmitarrays. *Nature Communications*, **6**, 1–6.

Arbabi, E., Arbabi, A., Kamali, S. M., Horie, Y., & Faraon, A. (2016). Multiwavelength polarization-insensitive lenses based on dielectric metasurfaces with meta-molecules. *Optica*, **3**, 628.

Asadchy, V. S., Faniayeu, I. A., Ra'di, Y., Khakhomov, S. A., Semchenko, I. V., & Tretyakov, S. A. (2015). Broadband reflectionless metasheets: Frequency-selective transmission and perfect absorption. *Physical Review X*, **5**, 1–10.

Asano, T., Mochizuki, K., Yamaguchi, M., Chaminda, M., & Noda, S. (2009). Spectrally selective thermal radiation based on intersubband transitions and photonic crystals. *Optics Express*, **17**, 19190–19203.

Aydin, K., Ferry, V. E., Briggs, R. M., & Atwater, H. A. (2011). Broadband polarization-independent resonant light absorption using ultrathin plasmonic super absorbers. *Nature Communications*, **2**, 517.

Baranov, D. G., Edgar, J. H., Hoffman, T., Bassim, N., & Caldwell, J. D. (2015). Perfect interferenceless absorption at infrared frequencies by a van der Waals crystal. *Physical Review B - Condensed Matter and Materials Physics*, **92**, 1–6.

Bezares, F. J., Long, J. P., Glembocki, O. J., Guo, J., Rendell, R. W., Kasica, R., Shirey, L., Owrutsky, J. C., & Caldwell, J. D. (2013). Mie resonance-enhanced light absorption in periodic silicon nanopillar arrays. *Optics Express*, **21**, 27587.

Bhattarai, K., Silva, S., Song, K., Urbas, A., Lee, S. J., Ku, Z., & Zhou, J. (2017). Metamaterial Perfect Absorber Analyzed by a Meta-cavity Model Consisting of Multilayer Metasurfaces. *Scientific Reports*, 1–9.

Biener, G., Dahan, N., Niv, A., Kleiner, V., & Hasman, E. (2008). Highly coherent thermal emission obtained by plasmonic bandgap structures. *Applied Physics Letters*, **92**, 4–7.

Braun, J. M., Schneider, H., Helm, M., Mirek, R., Boatner, L. A., Marvel, R. E., Haglund, R. F., & Pashkin, A. (2018). Ultrafast response of photoexcited carriers in vo2 at high-pressure. *New Journal of Physics*, **20**. https://doi.org/10.1088/1367-2630/aad4ef

Caldwell, J. D., Lindsay, L., Giannini, V., Vurgaftman, I., Reinecke, T. L., Maier, S. A., & Glembocki, O. J. (2015a). Low-loss, infrared and terahertz nanophotonics using surface phonon polaritons. *Nanophotonics*, **4**, 44–68.

Caldwell, J. D., Lindsay, L., Giannini, V., Vurgaftman, I., Reinecke, T. L., Maier, S. A., & Glembocki, O. J. (2015b). Low-loss , infrared and terahertz nanophotonics using surface phonon polaritons. *Nanophotonics*, **4**, 44–68.

Campione, S., Benz, A., Klem, J., Sinclair, M. B., Brener, I., & Capolino, F. (2014). Electrodynamic modeling of strong coupling between a metasurface and intersubband transitions in quantum wells. *Physical Review B - Condensed Matter and Materials Physics*, **89**.

Campione, S., Brener, I., & Marquier, F. (2015). Theory of epsilon-near-zero modes in ultrathin films. *Physical Review B - Condensed Matter and Materials Physics*, **91**, 1–5.

Chan, W., Chen, H.-T., Taylor, A., Brener, I., Cich, M. J., & Mittleman, D. M. (2009). A spatial light modulator for terahertz beams. *Applied Physics Letters*, **94**.

Chen, B. H., Wu, P. C., Su, V. C., Lai, Y. C., Chu, C. H., Lee, I. C., Chen, J. W., Chen, Y. H., Lan, Y. C., Kuan, C. H., & Tsai, D. P. (2017). GaN Metalens for Pixel-Level Full-Color Routing at Visible Light. *Nano Letters*, **17**, 6345–6352.

Chen, H. T., Padilla, W. J., Cich, M. J., Azad, A. K., Averitt, R. D., & Taylor, A. J. (2009). A metamaterial solid-state terahertz phase modulator. *Nature Photonics*, **3**, 148–151.

Chen, X. R., Hu, J. Z., Han, W. Z., & Xu, B. S. (2008). Study on electrical properties and 1064nm pulse laser damage of vanadium oxide thin film. *Key Engineering Materials*, **373–374**, 730–733.

Chuang, S. L. (2009). *Physics of Photonic Devices* (Second Edi). Hoboken, NJ: John Wiley & Sons.

De Ceglia, D., Campione, S., Vincenti, M. A., Capolino, F., & Scalora, M. (2013). Low-damping epsilon-near-zero slabs: Nonlinear and nonlocal optical properties. *Physical Review B - Condensed Matter and Materials Physics*, **87**, 1–12.

De Zoysa, M., Asano, T., Mochizuki, K., Oskooi, A., Inoue, T., & Noda, S. (2012). Conversion of broadband to narrowband thermal emission through energy recycling. *Nature Photonics*, **6**, 535–539.

Deal, B. E., & Grove, A. S. (1965). General relationship for the thermal oxidation of silicon. *Journal of Applied Physics*, **36**, 3770–3778.

Decker, M., Staude, I., Falkner, M., Dominguez, J., Neshev, D. N., Brener, I., Pertsch, T., & Kivshar, Y. S. (2015). High-Efficiency Dielectric Huygens' Surfaces. *Advanced Optical Materials*, **3**, 813–820.

Devarapu, G. C. R., & Foteinopoulou, S. (2017). Broadband Near-Unidirectional Absorption Enabled by Phonon-Polariton Resonances in SiC Micropyramid Arrays. *Physical Review Applied*, **7**, 1–15.

Dhanuskodi, S., Girisun, T. C. S., Smijesh, N., & Philip, R. (2010). Two-photon absorption and optical limiting in tristhiourea cadmium sulphate. *Chemical Physics Letters*, Vol. 486, pp. 80–83.

Du, Z., Chen, L., Kao, T. S., Wu, M., & Hong, M. (2015). Improved optical limiting performance of laser-ablation-generated metal nanoparticles due to silica-microsphere-induced local field enhancement. *Beilstein Journal of Nanotechnology*, **6**, 1199–1204.

Dunkelberger, A. D., Ellis, C. T., Ratchford, D. C., Giles, A. J., Kim, M., Kim, C. S., Spann, B. T., Vurgaftman, I., Tischler, J. G., Long, J. P., Glembocki, O. J., Owrutsky, J. C., & Caldwell, J. D. (2018). Active tuning of surface phonon polariton resonances via carrier photoinjection. *Nature Photonics*, **12**, 50–56.

Ehrlich, J. E., Wu, X. L., Lee, I.-Y. S., Hu, Z.-Y., Röckel, H., Marder, S. R., & Perry, J. W. (1997). Two-photon absorption and broadband optical limiting with bis-donor stilbenes. *Optics Letters*, **22**, 1843.

Epstein, A., & Eleftheriades, G. V. (2016). Huygens' metasurfaces via the equivalence principle: design and applications. *Journal of the Optical Society of America B*, **33**, A31.

Faenzi, M., Minatti, G., González-Ovejero, D., Caminita, F., Martini, E., Della Giovampaola, C., & Maci, S. (2019). Metasurface Antennas: New Models, Applications and Realizations. *Scientific Reports*, **9**, 1–14.

Feigenbaum, E., Diest, K., & Atwater, H. A. (2010). Unity-order index change in transparent conducting oxides at visible frequencies. *Nano Letters*, **10**, 2111–2116.

Fleming, J. G., Lin, S. Y., El-Kady, I., Biswas, R., & Ho, K. M. (2002). All-metallic three-dimensional photonic crytal with a large infrared bandgap. *Nature*, **417**, 52–55.

Folland, T. G., Nordin, L., Wasserman, D., & Caldwell, J. D. (2019). Probing polaritons in the mid- to far-infrared. *Journal of Applied Physics*, **125**. https://doi.org/10.1063/1.5090777

Folland, T., Runnerstrom, E. L., Kelly, K. P., Engheta, N., Caldwell, J. D., & Maria, J.-P. (2019).

Polaritonic hybrid-epsilon-near-zero modes: engineering strong optoelectronic coupling and dispersion in doped cadmium oxide bilayers (Conference Presentation). 7.

Fox, M. (2012). *Optical Properties of Solids: 2nd Edition*. New York, NY: Oxford University Press.

Geffrin, J. M., García-Cámara, B., Gómez-Medina, R., Albella, P., Froufe-Pérez, L. S., Eyraud, C., Litman, A., Vaillon, R., González, F., Nieto-Vesperinas, M., Sáenz, J. J., & Moreno, F. (2012). Magnetic and electric coherence in forward-and back-scattered electromagnetic waves by a single dielectric subwavelength sphere. *Nature Communications*, **3**. https://doi.org/10.1038/ncomms2167

Genevet, P., Capasso, F., Aieta, F., Khorasaninejad, M., & Devlin, R. (2017). Recent advances in planar optics: from plasmonic to dielectric metasurfaces. *Optica*, **4**, 139–152.

Gutruf, P., Zou, C., Withayachumnankul, W., Bhaskaran, M., Sriram, S., & Fumeaux, C. (2016). Mechanically tunable dielectric resonator metasurfaces at visible frequencies. *ACS Nano*, **10**, 133–141.

Haverkort, M. W., Hu, Z., Tanaka, A., Reichelt, W., Streltsov, S. V., Korotin, M. A., Anisimov, V. I., Hsieh, H. H., Lin, H. J., Chen, C. T., Khomskii, D. I., & Tjeng, L. H. (2005). Orbital-assisted metal-insulator transition in VO2. *Physical Review Letters*, **95**, 4–7.

He, G. S., Reinhardt, B. A., Bhatt, J. C., Dillard, A. G., McKellar, R., Xu, C., & Prasad, P. N. (1995). Two-photon absorption and optical-limiting properties of novel organic compounds: erratum. *Optics Letters*, **20**, 1930.

He, Q., Sun, S., & Zhou, L. (2019). Tunable/Reconfigurable Metasurfaces: Physics and Applications. *Research*, **2019**, 1–16.

Hedayati, M. K., Javaherirahim, M., Mozooni, B., Abdelaziz, R., Tavassolizadeh, A., Chakravadhanula, V. S. K., Zaporojtchenko, V., Strunkus, T., Faupel, F., & Elbahri, M. (2011). Design of a perfect black absorber at visible frequencies using plasmonic metamaterials. *Advanced Materials*, **23**, 5410–5414.

Hodgkinson, J., & Tatam, R. P. (2013). Optical gas sensing: A review. *Measurement Science and Technology*, **24**. https://doi.org/10.1088/0957-0233/24/1/012004

Holloway, C. L., Kuester, E. F., Gordon, J. A., O'Hara, J., Booth, J., & Smith, D. R. (2012). An overview of the theory and applications of metasurfaces: The two-dimensional equivalents of metamaterials. *IEEE Antennas and Propagation Magazine*, **54**, 10–35.

Huang, L., Chen, X., Mühlenbernd, H., Zhang, H., Chen, S., Bai, B., Tan, Q., Jin, G., Cheah, K. W., Qiu, C. W., Li, J., Zentgraf, T., & Zhang, S. (2013). Three-dimensional optical holography using a plasmonic metasurface. *Nature Communications*, **4**, 1–8.

Huang, Y. W., Lee, H. W. H., Sokhoyan, R., Pala, R. A., Thyagarajan, K., Han, S., Tsai, D. P., & Atwater, H. A. (2016). Gate-Tunable Conducting Oxide Metasurfaces. *Nano Letters*, **16**, 5319–5325.

Huygens, C. (1690). *Traité de la Lumiére*. Leyden: Pieter van der Aa.

Inoue, T., De Zoysa, M., Asano, T., & Noda, S. (2013a). Single-peak narrow-bandwidth mid-infrared thermal emitters based on quantum wells and photonic crystals. *Applied Physics Letters*, **102**, 10–14.

Inoue, T., De Zoysa, M., Asano, T., & Noda, S. (2013b). Single-peak narrow-bandwidth mid-infrared thermal emitters based on quantum wells and photonic crystals. *Applied Physics Letters*, **102**, 10–14.

Inoue, T., De Zoysa, M., Asano, T., & Noda, S. (2015a). Electrical tuning of emissivity and linewidth of thermal emission spectra. *Physical Review B - Condensed Matter and Materials Physics*, **91**, 1–5.

Inoue, T., De Zoysa, M., Asano, T., & Noda, S. (2015b). Realization of narrowband thermal emission with optical nanostructures. *Optica*, **2**, 27.

Inoue, T., De Zoysa, M., Asano, T., & Noda, S. (2016). High-Q mid-infrared thermal emitters operating with high power-utilization efficiency. *Optics Express*, **24**, 15101.

Inoue, T., Zoysa, M. De, Asano, T., & Noda, S. (2014). Realization of dynamic thermal emission control. *Nature Materials*, **13**, 928–931.

J.-J. Greddet, R. Carminati, K. Joulain, J.-P. Mulet, S. Mainguy, and Y. C. (2002). Coherent emission of light by thermal sources. *Nature (London)*, **416**, 61–64.

Jahani, S., & Jacob, Z. (2016). All-dielectric metamaterials. *Nature Nanotechnology*, **11**.

Jaynes, E. T., & Cummings, F. W. (1963). Comparison of quantum and semiclassical radiation theories with application to the beam maser. *Proc. IEEE*, **51**, 89–109.

Jin, M. H., Durstock, M., Dai, L. (2006). *Carbon Nanotechnology: Developments in Chemistry, Physics, Materials Science and Device Applications*. Elsevier B.V.

Kafaie Shirmanesh, G., Sokhoyan, R., Pala, R. A., & Atwater, H. A. (2018). Dual-Gated Active Metasurface at 1550 nm with Wide (>300°) Phase Tunability [Rapid-communication]. *Nano Letters*, **18**, 2957–2963.

Kannan, R., He, G. S., Lin, T. C., Prasad, P. N., Vaia, R. A., & Tan, L. S. (2004). Toward Highly Active Two-Photon Absorbing Liquids. Synthesis and Characterization of 1,3,5-Triazine-Based Octupolar Molecules. *Chemistry of Materials*, **16**, 185–194.

Karimzadeh, R., Aleali, H., & Mansour, N. (2011). Thermal nonlinear refraction properties of Ag2S semiconductor nanocrystals with its application as a low power optical limiter. *Optics Communications*, **284**, 2370–2375.

Karvounis, A., Aspiotis, N., Zeimpekis, I., Ou, J. Y., Huang, C. C., Hewak, D., & Zheludev, N. I. (2019). Mechanochromic Reconfigurable Metasurfaces. *Advanced Science*, **6**. https://doi.org/10.1002/advs.201900974

Karvounis, A., Ou, J. Y., Wu, W., Macdonald, K. F., & Zheludev, N. I. (2015). Nano-optomechanical nonlinear dielectric metamaterials. *Applied Physics Letters*, **107**. https://doi.org/10.1063/1.4935795

Kerker, M., Wang, D.-S., & Giles, C. L. (1983). Electromagnetic scattering by magnetic spheres. *Journal of the Optical Society of America*, **73**, 765.

Kim, H. T., Chae, B. G., Youn, D. H., Maeng, S. L., Kim, G., Kang, K. Y., & Lim, Y. S. (2004). Mechanism and observation of Mott transition in VO2-based two- and three-terminal devices. *New Journal of Physics*, **6**. https://doi.org/10.1088/1367-2630/6/1/052

Komar, A., Fang, Z., Bohn, J., Sautter, J., Decker, M., Miroshnichenko, A., Pertsch, T., Brener, I., Kivshar, Y. S., Staude, I., & Neshev, D. N. (2017). Electrically tunable all-dielectric optical metasurfaces based on liquid crystals. *Applied Physics Letters*, **110**. https://doi.org/10.1063/1.4976504

Kramers, H. A. (1927). La diffusion de la lumière par les atomes. *Atti Cong. Intern. Fisici, (Transactions of Volta Centenary Congress)*, **2**, 545–557.

Kronig, R. de L. (1926). On the Theory of Dispersion of X-Rays. *Journal of the Optical Society of America*, **12**, 547–557.

Kwon, M. S. (2016). Discussion of Two Ways of Optically Modeling Indium-Tin-Oxide Layers in Slot Waveguides for Waveguide Analysis. *IEEE Photonics Journal*, **8**, 1–9.

Landy, N. I., Sajuyigbe, S., Mock, J. J., Smith, D. R., & Padilla, W. J. (2008). Perfect metamaterial absorber. *Physical Review Letters*, **100**, 1–4.

Lazarovits, B., Kim, K., Haule, K., & Kotliar, G. (2010). Effects of strain on the electronic structure of VO2. *Physical Review B - Condensed Matter and Materials Physics*, **81**, 1–9.

Lee, B. J., Fu, C. J., & Zhang, Z. M. (2005). Coherent thermal emission from one-dimensional photonic crystals. *Applied Physics Letters*, **87**, 1–4.

Lenert, A., Bierman, D. M., Nam, Y., Chan, W. R., Celanović, I., Soljačić, M., & Wang, E. N. (2014). A nanophotonic solar thermophotovoltaic device. *Nature Nanotechnology*, **9**, 126–130.

Lewin, L. (1947). The electrical constants of a material loaded with spherical particles. *Journal of the Institution of Electrical Engineers-Part III: Radio and Communication Engineering*, **94**, 65–68.

Li, H., Wang, L., & Zhai, X. (2016). Tunable graphene-based mid-infrared plasmonic wide-angle narrowband perfect absorber. *Scientific Reports*, **6**, 1–8.

Li, K., Fitzgerald, J. M., Xiao, X., Caldwell, J. D., Zhang, C., Maier, S. A., Li, X., & Giannini, V. (2017). Graphene Plasmon Cavities Made with Silicon Carbide. *ACS Omega*, **2**, 3640–3646.

Li, W., & Valentine, J. (2014). Metamaterial perfect absorber based hot electron photodetection. *Nano Letters*, **14**, 3510–3514.

Liang, J., Li, W., Liu, J., & Hu, M. (2016). Room temperature CH4 sensing properties of Au decorated VO2 nanosheets. *Materials Letters*, **184**, 92–95.

Liaros, N., Koudoumas, E., & Couris, S. (2014). Broadband near infrared optical power limiting of few layered graphene oxides. *Applied Physics Letters*, **104**. https://doi.org/10.1063/1.4878660

Lin, J., Genevet, P., Kats, M. A., Antoniou, N., & Capasso, F. (2013). Nanostructured holograms for broadband manipulation of vector beams. *Nano Letters*, **13**, 4269–4274.

Lin, S. Y., Moreno, J., & Fleming, J. G. (2003). Three-dimensional photonic-crystal emitter for thermal photovoltaic power generation. *Applied Physics Letters*, **83**, 380–382.

Liu, H.-K. (2003). Nonlinear optical limiting of the azo dye methyl-red doped nematic liquid crystalline films. *Optical Engineering*, **42**, 2936.

Liu, L., Kang, L., Mayer, T. S., & Werner, D. H. (2016). Hybrid metamaterials for electrically triggered multifunctional control. *Nature Communications*, **7**, 1–8.

Liu, Xianliang, Starr, T., Starr, A. F., & Padilla, W. J. (2010). Infrared spatial and frequency selective metamaterial with near-unity absorbance. *Physical Review Letters*, **104**, 1–4.

Liu, Xianliang, Tyler, T., Starr, T., Starr, A. F., Jokerst, N. M., & Padilla, W. J. (2011). Taming the blackbody with infrared metamaterials as selective thermal emitters. *Physical Review Letters*, **107**, 4–7.

Liu, Xiaoming, Zhao, Q., Lan, C., & Zhou, J. (2013). Isotropic Mie resonance-based metamaterial perfect absorber. *Applied Physics Letters*, **103**, 1–4.

Long, J. P., Tischler, J. G., Bezares, F. J., Bassim, N. D., Maier, S. A., Wheeler, V. D., Vurgaftman, I., Owrutsky, J. C., Glembocki, O. J., Shirey, L. M., Francescato, Y., Sharac, N., Kasica, R., Caldwell, J. D., & Giannini, V. (2013). Low-Loss, Extreme Subdiffraction Photon Confinement via Silicon Carbide Localized Surface Phonon Polariton Resonators. *Nano Letters*, **13**, 3690–

3697.

Love, A. E. H. (1901). The integration of the equations of propagation of electric waves. *Phil. Trans. R. Soc. Lond. A*, 1–45.

Lu, Y. J., Sokhoyan, R., Cheng, W. H., Kafaie Shirmanesh, G., Davoyan, A. R., Pala, R. A., Thyagarajan, K., & Atwater, H. A. (2017). Dynamically controlled Purcell enhancement of visible spontaneous emission in a gated plasmonic heterostructure. *Nature Communications*, **8**, 1–8.

Markel, V. A. (2016). Introduction to the Maxwell Garnett approximation: tutorial. *Journal of the Optical Society of America A*, **33**, 1244.

Markov, P., Marvel, R. E., Conley, H. J., Miller, K. J., Haglund, R. F., & Weiss, S. M. (2015). Optically Monitored Electrical Switching in VO2. *ACS Photonics*, **2**, 1175–1182.

Mason, J. A., Smith, S., & Wasserman, D. (2011). Strong absorption and selective thermal emission from a midinfrared metamaterial. *Applied Physics Letters*, **98**, 96–99.

Miao, Z., Wu, Q., Li, X., He, Q., Ding, K., An, Z., Zhang, Y., & Zhou, L. (2015). Widely tunable terahertz phase modulation with gate-controlled graphene metasurfaces. *Physical Review X*, **5**, 1–13.

Mie, G. (1908). Contributions to the optics of turbid media, particularly of colloidal metal solutions. *Ann. Phys. (Leipsig)*, **25**, 377–445.

Mii, Y., Karunasiri, R., Wang, K., Chen, M., & Yuh, P. (1990). Large Stark shifts of the local to global state intersubband transitions in step quantum wells. *Applied Physics Letters*, **56**.

Miller, K. J., Haglund, R. F., & Weiss, S. M. (2018). Optical phase change materials in integrated silicon photonic devices: review. *Optical Materials Express*, **8**, 2415.

Miller, K. J., Hallman, K. A., Haglund, R. F., & Weiss, S. M. (2017). Silicon waveguide optical switch with embedded phase change material. *Optics Express*, **25**, 26527.

Monticone, F., Estakhri, N. M., & Alù, A. (2013). Full control of nanoscale optical transmission with a composite metascreen. *Physical Review Letters*, **110**, 1–5.

Ni, X., Wong, Z. J., Mrejen, M., Wang, Y., & Zhang, X. (2015). An Ultrathin invisibility skin cloak for visible light. *Science*, **349**.

Oskooi, A., Noda, S., Inoue, T., De Zoysa, M., & Asano, T. (2012). Design of single-mode narrow-bandwidth thermal emitters for enhanced infrared light sources. *Journal of the Optical Society of America B*, **30**, 165.

Ou, J. Y., Plum, E., Zhang, J., & Zheludev, N. I. (2013). An electromechanically reconfigurable plasmonic metamaterial operating in the near-infrared. *Nature Nanotechnology*, **8**, 252–255.

Park, C.-S., Koirala, I., Gao, S., Shrestha, V. R., Lee, S.-S., & Choi, D.-Y. (2019). Structural color filters based on an all-dielectric metasurface exploiting silicon-rich silicon nitride nanodisks. *Optics Express*, **27**, 667.

Park, J., Kang, J. H., Liu, X., & Brongersma, M. L. (2015). Electrically Tunable Epsilon-Near-Zero (ENZ) Metafilm Absorbers. *Scientific Reports*, **5**, 1–9.

Pfeiffer, C., Emani, N. K., Shaltout, A. M., Boltasseva, A., Shalaev, V. M., & Grbic, A. (2014). Efficient light bending with isotropic metamaterial Huygens' surfaces. *Nano Letters*, **14**, 2491–2497.

Pfeiffer, C., & Grbic, A. (2013a). Cascaded metasurfaces for complete phase and polarization control. *Applied Physics Letters*, **102**. https://doi.org/10.1063/1.4810873

Pfeiffer, C., & Grbic, A. (2013b). Metamaterial Huygens' surfaces: Tailoring wave fronts with reflectionless sheets. *Physical Review Letters*, **110**, 1–5.

Powell, A., Christiansen, J., Gregory, R. B., Wetteroth, T., & Wilson, S. R. (1999). Carrier concentration and lattice absorption in bulk and epitaxial silicon carbide determined using infrared ellipsometry. *Physical Review B - Condensed Matter and Materials Physics*, **60**, 11464–11474.

Prasai, D., Klots, A. R., Newaz, A. K. M., Niezgoda, J. S., Orfield, N. J., Escobar, C. A., Wynn, A., Efimov, A., Jennings, G. K., Rosenthal, S. J., & Bolotin, K. I. (2015). Electrical Control of near-Field Energy Transfer between Quantum Dots and Two-Dimensional Semiconductors. *Nano Letters*, **15**, 4374–4380.

Rodríguez-Ulibarri, P., Beruete, M., & Serebryannikov, A. E. (2017). One-way quasiplanar terahertz absorbers using nonstructured polar dielectric layers. *Physical Review B*, **96**, 1–9.

Runnerstrom, E. L., Kelley, K. P., Sachet, E., Shelton, C. T., & Maria, J. P. (2017). Epsilon-near-Zero Modes and Surface Plasmon Resonance in Fluorine-Doped Cadmium Oxide Thin Films. *ACS Photonics*, **4**, 1885–1892.

Sai, H., & Yugami, H. (2004). Thermophotovoltaic generation with selective radiators based on tungsten surface gratings. *Applied Physics Letters*, **85**, 3399–3401.

Samson, Z. L., MacDonald, K. F., De Angelis, F., Gholipour, B., Knight, K., Huang, C., Di Fabrizio, E., Hewak, D., & Zheludev, N. I. (2010). Metamaterial electro-optic switch of nanoscale thickness. *Applied Physics Letters*, **96.**

Sato, T., Dai, J., & Wang, X. (1967). Spectral Emissivity of Silicon. *Japanese Journal of Applied Physics*, **6**, 339–347.

Sautter, J., Staude, I., Decker, M., Rusak, E., Neshev, D. N., Brener, I., & Kivshar, Y. S. (2015). Active tuning of all-dielectric metasurfaces. *ACS Nano*, **9**, 4308–4315.

Savo, S., Shrekenhamer, D., & Padilla, W. J. (2014). Liquid crystal metamaterial absorber spatial light modulator for THz applications. *Advanced Optical Materials*, **2**, 275–279.

Schuck, P. J., Fromm, D. P., Sundaramurthy, A., Kino, G. S., & Moerner, W. E. (2005). Improving the mismatch between light and nanoscale objects with gold bowtie nanoantennas. *Physical Review Letters*, **94**, 14–17.

Schuller, J. A., Taubner, T., & Brongersma, M. L. (2009). Optical antenna thermal emitters. *Nature Photonics*, **3**, 658–661.

Schuller, J. A., Zia, R., Taubner, T., & Brongersma, M. L. (2007). Dielectric metamaterials based on electric and magnetic resonances of silicon carbide particles. *Physical Review Letters*, **99**, 1–4.

Semmlinger, M., Tseng, M. L., Yang, J., Zhang, M., Zhang, C., Tsai, W. Y., Tsai, D. P., Nordlander, P., & Halas, N. J. (2018). Vacuum Ultraviolet Light-Generating Metasurface [Rapid-communication]. *Nano Letters*, **18**, 5738–5743.

Shcherbakov, M. R., Liu, S., Zubyuk, V. V., Vaskin, A., Vabishchevich, P. P., Keeler, G., Pertsch, T., Dolgova, T. V., Staude, I., Brener, I., & Fedyanin, A. A. (2017). Ultrafast all-optical tuning of direct-gap semiconductor metasurfaces. *Nature Communications*, **8**, 1–5.

Shcherbakov, M. R., Vabishchevich, P. P., Shorokhov, A. S., Chong, K. E., Choi, D. Y., Staude, I., Miroshnichenko, A. E., Neshev, D. N., Fedyanin, A. A., & Kivshar, Y. S. (2015). Ultrafast All-Optical Switching with Magnetic Resonances in Nonlinear Dielectric Nanostructures. *Nano Letters*, **15**, 6985–6990.

Sherrott, M. C., Hon, P. W. C., Fountaine, K. T., Garcia, J. C., Ponti, S. M., Brar, V. W., Sweatlock, L. A., & Atwater, H. A. (2017). Experimental Demonstration of >230° Phase Modulation in Gate-Tunable Graphene-Gold Reconfigurable Mid-Infrared Metasurfaces. *Nano Letters*, **17**, 3027–3034.

Silveirinha, M., & Engheta, N. (2006). Tunneling of electromagnetic energy through subwavelength channels and bends using ε-near-zero materials. *Physical Review Letters*, **97**, 1–4.

Sipe, J. E., & Kranendonk, J. Van. (1974). Macroscopic electromagnetic theory of resonant dielectrics. *Physical Review A*, **9**, 1806–1822.

Smith, D. R., Padilla, W. J., Vier, D. C., Nemat-Nasser, S. C., & Schultz, S. (2000). Composite Medium with Simultaneously Negative Permeability and Permittivity. *Physical Review Letters*, **84**, 4184–4187.

Spinelli, P., Verschuuren, M. A., & Polman, A. (2012). Broadband omnidirectional antireflection coating based on subwavelength surface Mie resonators. *Nature Communications*, **3**, 692–695.

Stefanovich, G., Pergament, A., & Stefanovich, D. (2000). Electrical switching and Mott transition in VO2. *Journal of Physics Condensed Matter*, **12**, 8837–8845.

Strelcov, E., Lilach, Y., & Kolmakov, A. (2009). Gas sensor based on metal-insulator transition in VO 2 nanowire thermistor. *Nano Letters*, **9**, 2322–2326.

Su, V.-C., Chu, C. H., Sun, G., & Tsai, D. P. (2018). Advances in optical metasurfaces: fabrication and applications. *Optics Express*, **26**, 13148.

Tseng, M. L., Yang, J., Semmlinger, M., Zhang, C., Nordlander, P., & Halas, N. J. (2017). Two-

Dimensional Active Tuning of an Aluminum Plasmonic Array for Full-Spectrum Response. *Nano Letters*, **17**, 6034–6039.

Vella, J. H., Goldsmith, J. H., Browning, A. T., Limberopoulos, N. I., Vitebskiy, I., Makri, E., & Kottos, T. (2016). Experimental Realization of a Reflective Optical Limiter. *Physical Review Applied*, **5**, 1–7.

Veselago, V. G. (1968). THE ELECTRODYNAMICS OF SUBSTANCES WITH SIMULTANEOUSLY NEGATIVE VALUES OF Epsilon and Mu. *Soviet Physics Uspekhi*, **10**, 509–514.

Videen, G., & Bickel, W. S. (1992). Light-scattering resonances in small spheres. *Physical Review A*, **45**, 6008–6012.

Wang, H., Yi, X., & Li, Y. (2005). Fabrication of VO2 films with low transition temperature for optical switching applications. *Optics Communications*, **256**, 305–309.

Wang, T., Li, P., Chigrin, D. N., Giles, A. J., Bezares, F. J., Glembocki, O. J., Caldwell, J. D., & Taubner, T. (2017). Phonon-Polaritonic Bowtie Nanoantennas: Controlling Infrared Thermal Radiation at the Nanoscale [Research-article]. *ACS Photonics*, **4**, 1753–1760.

Wegkamp, D., Herzog, M., Xian, L., Gatti, M., Cudazzo, P., McGahan, C. L., Marvel, R. E., Haglund, R. F., Rubio, A., Wolf, M., & Stähler, J. (2014). Instantaneous band gap collapse in photoexcited monoclinic VO2 due to photocarrier doping. *Physical Review Letters*, **113**, 2–6.

Westlund, R., Glimsdal, E., Lindgren, M., Vestberg, R., Hawker, C., Lopes, C., & Malmström, E. (2008). Click chemistry for photonic applications: Triazole-functionalized platinum(ii) acetylides for optical power limiting. *Journal of Materials Chemistry*, **18**, 166–175.

Wu, P. C., Pala, R. A., Kafaie Shirmanesh, G., Cheng, W. H., Sokhoyan, R., Grajower, M., Alam,

M. Z., Lee, D., & Atwater, H. A. (2019). Dynamic beam steering with all-dielectric electro-optic III–V multiple-quantum-well metasurfaces. *Nature Communications*, **10**, 1–9.

Xu, J., Cua, M., Zhou, E. H., Horie, Y., Faraon, A., & Yang, C. (2018). Wide-angular-range and high-resolution beam steering by a metasurface-coupled phased array. *Optics Letters*, **43**, 5255.

Yang, B., Liu, W., Li, Z., Cheng, H., Chen, S., & Tian, J. (2018). Polarization-Sensitive Structural Colors with Hue-and-Saturation Tuning Based on All-Dielectric Nanopixels. *Advanced Optical Materials*, **6**, 1–8.

Yang, Y., Wang, W., Boulesbaa, A., Kravchenko, I. I., Briggs, D. P., Puretzky, A., Geohegan, D., & Valentine, J. (2015). Nonlinear Fano-Resonant Dielectric Metasurfaces. *Nano Letters*, **15**, 7388–7393.

Yang, Y., Wang, W., Moitra, P., Kravchenko, I. I., Briggs, D. P., & Valentine, J. (2014). Dielectric meta-reflectarray for broadband linear polarization conversion and optical vortex generation. *Nano Letters*, **14**, 1394–1399.

Yao, Y., Shankar, R., Kats, M. A., Song, Y., Kong, J., Loncar, M., & Capasso, F. (2014). Electrically tunable metasurface perfect absorbers for ultrathin mid-infrared optical modulators. *Nano Letters*, **14**, 6526–6532.

Yu, N., Aieta, F., Genevet, P., Kats, M. A., Gaburro, Z., & Capasso, F. (2012). A broadband, background-free quarter-wave plate based on plasmonic metasurfaces. *Nano Letters*, **12**, 6328–6333.

Yu, N., & Capasso, F. (2014). Flat optics with designer metasurfaces. *Nature Materials*, **13**, 139–150.

Yu, N., Genevet, P., Kats, M. a, Aieta, F., Tetienne, J.-P., Capasso, F., & Gaburro, Z. (2011). Light Propagation with Phase Reflection and Refraction. *Science*, **334**, 333–337.

Zhang, H. T., Zhang, L., Mukherjee, D., Zheng, Y. X., Haislmaier, R. C., Alem, N., & Engel-Herbert, R. (2015). Wafer-scale growth of VO 2 thin films using a combinatorial approach. *Nature Communications*, **6**. https://doi.org/10.1038/ncomms9475

Zhu, H., Luo, H., Li, Q., Zhao, D., Cai, L., Du, K., Xu, Z., Ghosh, P., & Qiu, M. (2018). Tunable narrowband mid-infrared thermal emitter with a bilayer cavity enhanced Tamm plasmon. *Optics Letters*, **43**, 5230.

Zhu, S., Lo, G. Q., & Kwong, D. L. (2014). Design of an ultra-compact electro-absorption modulator comprised of a deposited TiN/HfO_2/ITO/Cu stack for CMOS backend integration. *Optics Express*, **22**, 17930.

Zhu, W. M., Liu, A. Q., Zhang, X. M., Tsai, D. P., Bourouina, T., Teng, J. H., Zhang, X. H., Guo, H. C., Tanoto, H., Mei, T., Lo, G. Q., & Kwong, D. L. (2011). Switchable magnetic metamaterials using micromachining processes. *Advanced Materials*, **23**, 1792–1796.

Zhu, Z., Evans, P. G., Haglund, R. F., & Valentine, J. G. (2017). Dynamically Reconfigurable Metadevice Employing Nanostructured Phase-Change Materials. *Nano Letters*, **17**, 4881–4885.